# Subaqueous Sand Dunes and Sediment Starvation

By

GAETANO PORCILE

Department of Civil, Chemical and Environmental Engineering

UNIVERSITY OF GENOA

A dissertation submitted to the University of Genoa in accordance with the requirements of the degree of DOCTOR OF PHILOSOPHY.

Advisor: PROF. PAOLO BLONDEAUX

DECEMBER 2018

# Acknowledgements

First and foremost I wish to give my sincere thanks to my supervisor Prof. Paolo Blondeaux for his constant support and guidance. I have only found your stimulating suggestions and encouragements to have brought about fundamental discussions regarding all aspects of this project: research, conferences, courses, education, and the writing of this dissertation.

I am also very grateful to Prof. Marco Colombini and Prof. Giovanna Vittori with whom I have had the honour and pleasure of working along side during most of the different stages of the project. Thanks Marco for the bright discussions on fluvial bedforms and for your essential advice in the numerical modelling part of this research. Many thanks Giovanna also for introducing me to the amazing world of teaching.

I gratefully acknowledge Prof. Pieter C. Roos, Prof. Brad Murray and Prof. Albert Falqués for they agreed to review this work and consequently provided useful suggestions and comments which have inspired the enrichment of this dissertation.

Of course, grateful acknowledgements are also owed to all the staff and fellow scientists of the Department of Civil, Chemical and Environmental Engineering at the University of Genoa. Many thanks to all my PhD mates with whom I shared this although challenging very rewarding experience.

Last but by no means least, special words of thanks go to my parents for giving me unconditional support during all the studies, and to Flora – the only person capable of taking me away from sand dunes during these last years.

This thesis is dedicated to Luciana.

# Table of Contents

# Chapter 1

# Introduction

## 1.1 Sediment starved patterns

*Sediment patterns* produced by natural water flows over erodible granular surfaces are highly intriguing and equally of great practical importance. In order to rationally introduce the reader to the variety of sediment patterns encountered in nature, a criterion for their classification is briefly outlined below. It is possible to distinguish among erosional, depositional and equilibrium patterns depending on the balance between sediment availability and the sediment transport capacity of the forcing flow. Erosional patterns are mainly present in the upper part of river basins (mountain fronts, glaciers) where sediment supply is typically smaller than flow transport capacity. Depositional patterns develop at the base of mountain fronts (alluvial fans) and in those transitional regions where rivers meet the ocean (deltas, lagoons) owing to the inevitable reduction in the velocity of the carrier flows and also in their resulting transport capacity. Erosional and depositional patterns are the expression of a forced response of the flow-sediment system to hydrologic and geometric constraints. In contrast, equilibrium patterns arise as rhythmic oscillations of erosion and deposition in space and time so that a spatial-temporal equilibrium is maintained. These patterns (bedforms, planforms) represent a free response of the flow-sediment system to instabilities of the liquid-solid interface in the form of internal waves showing a spectacular surprisingly self-organisation. Depending on the various physical processes driving their formation, these regular patterns display different spatial and temporal scales. The sediment patterns listed below form as a free instability of the bed elevation, known as bedforms, and shape shallow water seafloors and fluvial channels. Of note, although the erosion and deposition itsef is a forced response, there can still be free responses (bedforms) within the upper part of river basins (cyclic steps, climbing ripples).

River beds are seldom flat and those that contain sand generally exhibit fairly regular undulations that arise spontaneously from an instability of the bed surface. These rippled sandy beds develop when viscosity affects the vertical velocity profile of the river stream in the near-bed region (hydraulically smooth and transitional flows) and, in turn, the bed shear stress and the related sediment transport, inducing a particular bed wave instability that ultimately leads to the appearance of the aforementioned bedforms, known as *ripples*. These small-scale sandy patterns exhibit asymmetric profiles with fairly regular crests that migrate invariably downstream and their formation does not depend on the flow depth being

Figure 1.1: Fascinating bedforms of Curtis Island, Cape Capricorn, Queensland, Australia. From the series 'Abstract Earth' © Richard Woldendorp.

characteristic of subcritical flows in the Reynolds sense: they are likely to emerge when the grain Reynolds number is lower than a certain critical value. *Dunes* are very similar to ripples as they exhibit many comparable characteristics, although these bedforms are much larger in size and they form where coarser sediment disrupts the viscous sub-layer (hydraulically rough flows). Fluvial dunes are sand waves that, invariably, migrate downstream and are marked by a sequence of gentle lee-slopes and sharp stoss-fronts. Their typical crest-to-crest distance scales with the flow depth and they are characteristic of subcritical flows in the Froude sense. *Antidunes* are a distinct class of bedforms, which scale with the flow depth and emerge from sediment mixtures forced by supercritical streams and, unlike dunes, these bedforms may migrate either upstream or downstream exhibiting rather symmetric profiles. All the above listed bedforms have crests perpendicular to the main direction of the flow and, as such, are a primary source of flow roughness. Their presence is therefore a major factor in determining water levels. On the one hand, flow and sediment transport produce bedforms, on the other hand, bedform appearance profoundly influences flow and sediment transport. Because of their significance in formulating depth-discharge relations for river flows and predictor formulae for sediment transport, bedforms in general, and dunes in particular, received extensive attention from engineers and geomorphologists.

Even more fascinating is the variety of beforms encountered in shallow sandy seas. Most readers would be familiar with those small regular patterns that are clearly visible on sandy beaches during low tide. These bedforms are known as *sea wave ripples* as they form as a consequence of the oscillatory flow at the bottom of sea waves in the surf zone. In deeper waters, sea wave ripples are found on the flanks of larger morphological patterns resulting in

an overlap of different types of bedforms generating fascinating and complex morphologies. The most common large-scale bedforms encountered in shallow water offshore regions are sand dunes and sand banks that are respectively associated with relatively weak and strong tidal currents. *Tidal dunes* are rhythmic, elongated, sandy bodies which are typically several meters high and display a regular spacing of the order of hundreds of meters. Their formation comes as a consequence of oscillatory tidal flows that interact harmonically with the perturbations of the seabed giving rise to steady recirculating cells that cause a net sediment transport which drags sediments towards the crests of these patterns. Since these bedforms evolve in unsteady oscillating currents, their sawtooth profiles are less asymmetric than those of fluvial dunes, and flow separation does not occur at their crests. *Tidal banks* are huge sandy bodies tens of meters high and tens of kilometres long spaced a few kilometres apart and, in the northern hemisphere, display crests rotated counterclockwise with respect to the main direction of the tidal current. A different interaction of oscillatory flows with seabed undulations leads to the appearance of tidal banks. When a tidal current crosses a sand bank whose crest is inclined with respect to the propagation of the tidal wave, the velocity of the current experiences an increase of its cross-bank component as the water depth decreases, whereas its along-bank component decreases as the bottom friction increases. Such a deflection of tidal currents that cross a sand bank results in a net sediment transport which is directed towards the bank crest during both the flood and ebb phase of the tide, thus resulting in bank accretion. In contrast to tidal sand banks that hardly ever move, tidal dunes behave very dynamically and their remarkable migration strongly depends on the intensity of the local residual current. Tidal dune migration and seasonal-variations in their amplitude and shape significantly affect the bathymetry of shallow water regions. In some cases, this leads to a reduction of water depths in navigation channels. Understanding their dynamics has a crucial application in the proper design of procedures related to dredging and mining activities. Furthermore, their migration may also cause the exposure of submarine pipelines and cables. And indeed strong tidal currents and severe sea storms may, in turn, lead to faults and/or damage of these infrastructures. The practical interest in tidal dunes arises in connection with the construction, safeguarding and maintenance of offshore and coastal structures, whose safety can be endangered by dune migration.

Both field observations and laboratory experiments have revealed that sediment transport produced by water flows can strongly vary as a result of the appearance of sediment patterns and/or the variability in sediment supply. As sediment supply to a stream is progressively reduced, the active zone of sediment transport narrows and some of the coarser particles get left behind on the bed. This results in an overall fining of the sediment in motion and a coarsening of the sediment resting at the bottom (Dietrich et al., 1989). As a consequence, limitation of the sediment supply can cause an expansion of coarse patches that eventually leads to the formation of a motionless substratum which inhibits the entrainment of sediment, This condition will herein be referred to as *sediment starvation*. The size of the material available for transport, as well as that of the transported particles, determines the mobility of the sediment mixtures. Gravel-sand mixtures can experience full or partial mobility. Full mobility occurs when the particle size in transport and that resting at the bed is approximately the same, whereas the latter, partial mobility, occurs when transported sediment is finer than bed material.

As channel slopes decrease, rivers typically exhibit abrupt transitions from gravel to sandy bottoms. In gravel-bed rivers, full mobility transport is rare as they usually experience partial mobility and, in many cases, seasonal and perennial streams exhaust the supply of sediment

that their transport capacity is able to entrain. As such, the finer sediment is mobilised while the mean grain size of the sediment resting at the bed surface becomes coarser. As a result, poorly sorted mixtures of sediment subject to periods of low flows or discharge waves undergo a transient degradation until they are fully armoured (Parker et al., 1982). Then the armour layer inhibits the entrainment of finer sediment from the bed which eventually leads to sediment starvation. Such sediment starvation may be natural, as described above, or may be man-made (such as erosion prevention measures) or induced (such as construction of dams). Among the most significant factors affecting global sediment delivery is the construction of dams in fluvial networks that cause rivers to fragment into a series of pools hence altering natural sediment transport. Dams trap sediment in their storage reservoirs and thus drastically reduce the sediment supply for downstream transport leading to dramatic effects on fluvial and coastal morphologies and, on a more local scale, sediment starvation.

Where sediment starvation does not affect the formation of sediment patterns, a well-known sequence of alluvial bedforms, that includes ripples, dunes and antidunes, can be identified as the strength of the forcing flow increases. A comparable sequence of bedforms has not yet been precisely identified whereby their appearance is also dictated by sediment starvation. *Starved bedforms* of fine sediment that develop over a static coarser substratum have been nevertheless well documented and include sand ribbons, barchans and dunes. Most readers should have at least some familiarity with aeolian barchan dunes widespread over sand-deserts. In subaqueous environments, starved bedforms have been especially observed in gravel bed rivers where the armour layer develops, but fine material continues to be persistently supplied from floodplains and hillslopes. *Barchan dunes* have a crescent shape with horns pointing downstream and seem to form whenever transported sediment is insufficient for the formation of fully developed ripples or dunes. As the sediment supply increases, barchans may gradually coalesce to dunes in a transition process, starting from barchans to barchanoids with increasing slip-face lengths, onto dunes with a barchanoid shape, and eventually to more or less two-dimensional transverse dunes which exhibit flat troughs where a motionless substrate is exposed (Kleinhans et al., 2002), hereinafter referred to as *starved dunes*.

A similar sequence of bedforms has also been well-described in aeolian environments (Bagnold, 1953), tidal environments (Allen, 1968) and on the sea floor (Lonsdale and Malfait, 1974). This suggests that a definable suite of starved bedforms develops regardless of the nature and the motion of the carrier fluid. *Amorphous sandy mounds* have been observed in submarine shallow water environments, where sediment starvation prevents the appearance of typical tidal dunes (Le Bot, 2001). In offshore regions, where tidal currents accelerate because of geometric constraints, intense flow velocities prevent the uniform deposition of sediment eventually leading to the exposition of relict pebble lags deposited before the post-glacial sea level rise (Houbolt, 1968). Over these motionless substrata, mobile sediment is transported in the form of morphological patterns that resemble tidal dunes but display more irregular geometries and a much larger spacing, these bedforms will herein be referred to as *tidal sandy mounds*.

## 1.2 Morphodynamics of fluvial and coastal dunes

How natural water flows interact with erodible granular surfaces by sediment transport is an interesting subject that becomes even more compelling when the feedback between sedi-

ment transport and morphology is taken into account. *Geomorphology*, the study of the form of the ground surface and the processes that mould it, has recently tended to become more deeply involved with the quantitative understanding of the processes of erosion, transport and deposition of sediment that are ultimately responsible for landform formation. Resultantly, it has developed many branches that comprise the study of a wide range of phenomena. *Morphodynamics* has been conceived in such a strongly interdisciplinary context and, originally developed at the boundary between geomorphology (Allen, 1982) and hydraulic engineering (Vanoni, 1975), it has rapidly evolved from an initial descriptive empirical status to establishing itself as a stand-alone branch of fluid mechanics. *Coastal and river morphodynamics* refer to the study of the fascinating interaction of seafloor and river channels with free surface water flows by sediment transport. Water flowing over an erodible surface induces sediment transport that changes the morphology of the surface whose evolution, in turn, changes the flow and sediment transport fields in a continuous feedback loop.

Felix Maria Exner, an Austrian researcher active in the early part of the twentieth century, was the first to derive an equation describing the *conservation of sediment mass* which was instrumental in aiding the formulation of the morphodynamic problem in quantitative terms. Morphodynamics generally deals with the motion of the interface between an erodible medium consisting of motionless, densely-packed sediment particles and a dynamic mixture composed of flowing water and transported sediment particles. Water flow may entrain sediment belonging to the erodible medium and, conversely, sediment transported by the flow may deposit at the interface between the two media. The inherent non-uniformity of both forcing flows and sediment supplies leads to an imbalance between entrainment and deposition of sediment ultimately resulting in the displacement of the liquid-solid interface. The

Figure 1.2: Barchan dunes of the Namib Desert, Namibia. © Ladislav Kamaràd.

equation describing the evolution of the erodible interface can be derived directly from the conservation of the sediment mass, commonly quoted as the *Exner equation* (Exner, 1925).

In many cases, the problem of morphodynamics reveals itself as a free boundary problem. Since an exchange of sediment particles exists between the water flow and the erodible medium, the time development of the interface between the two media turns out to be very much like that of a *free boundary*, the shape of which is apriori unknown depending on the highly variable parameters that characterise water flow and sediment supply. As would be expected, instabilities of the free boundary arise spontaneously as internal waves which shape the boundary itself and, as a result, the processes of erosion, transport and deposition of sediment are responsible for the formation of specific and somewhat predictable sediment patterns that ultimately determine the morphology of river channels, coasts and offshore regions.

As already pointed out in 1.1, among the variety of sediment patterns typically observed in fluvial and coastal environments *sand dunes* are far more important than any other bedforms. The appearance of sand dunes and their characteristics have been studied in great detail by various researchers over the years and a great deal of theoretical and physical modelling has been carried out in relation to their morphology and dynamics. Progress in the understanding of dune dynamics is still being made with ever improving techniques through laboratory and field observations. Field surveys clearly show that these bedforms are repetitive both in time and space and, as such, typical wavelengths, amplitudes and migration speeds can be assigned to them. Although no theoretical models has yet been able to reproduce all the characteristics of sand dunes correctly, idealised models do exist which are capable of predicting their spacing. By describing their appearance as a free instability of a sandy bottom forced by a water flow, these models, based on a linear stability analysis, are able to predict dune wavelengths in fair agreement with both laboratory and field observations.

The morphodynamic evolution of subaqueous sand dunes is a non-trivial problem which has been addressed by several authors. A first theoretical approach to the study of sand dune formation was proposed by Kennedy (1969), who's contribution proved that fluvial

Figure 1.3: Sand dunes of the Delta do Parnaìba, Brazil. © Maranhão de Todos Nòs.

dunes can be interpreted as a free instability of perturbed alluvial beds forced by uniform steady flows. Later, Engelund (1970), described dune instability as a result of the balance between the stabilising effects of gravity and the destabilising effects of friction leading to a phase shift between the bottom perturbation and the perturbation of the shear stress which drives the instability process. By using suitable flow models and the sediment continuity equation, progresses were made in the modelling of the formation of fluvial dunes within the framework of linear stability encompassing various lines of research (Richards, 1980). An extensive review of the linear theory of fluvial dune formation can be found in Colombini (2004), who revisited it by overcoming some deficiencies in the state-of-the-art modelling through the use of a more refined description of both hydrodynamics and sediment transport.

A similar instability process is responsible for the emergence of tidal dunes. A first attempt, proposed by Deigaard and Fredsøe (1987), was made to extend the aforementioned theoretical modelling developed in the framework of alluvial streams to the problem of tidal dune formation. Based on the physical analogy between fluvial dunes, which form where alluvial beds are forced by steady currents, and tidal dunes, which form where sandy seafloors are forced by slow varying tidal currents, the model is an adaptation of the dune model by Fredsøe (1974). However, since tidal flows have an intrinsic oscillatory character, the mechanism leading to the appearance of tidal dunes turns out to be different from that which induces the formation of dunes in fluvial environments. The presence of tidal dunes is related to steady streams in the form of recirculating cells over the depth owing to the interaction between seafloor perturbations and oscillatory tidal flows. The first detailed investigation of this interaction was made by Hulscher (1996), who proved that these large-scale sand waves can be interpreted as a free instability of a seabed undulation forced by tidal currents. Later Besio et al. (2006) improved the linear stability analysis proposed by Hulscher (1996) accounting for a more refined description of turbulence dynamics which allows the complete evaluation of the flow field from the bottom up to the free surface. Moreover, Besio et al. (2006) accounted for the presence of residual currents, which have a large influence on the migration of tidal dunes, and of wind waves, whose stirring lift into suspension large amounts of sediment affecting the formation of tidal dunes. In addition, they were able to highlight the crucial role played by the phase shift between different tidal constituents in determining dune migration, which is their most important property to be evaluated.

## 1.3 Hydraulic sediment transport

The above-mentioned morphodynamic predictions of the dynamics of sediment patterns observed in fluvial and coastal environments strongly rely on the modelling of *sediment transport* for given hydraulic conditions and sediment parameters.

The term *sediment* encompasses a wide range of particles with different grain sizes, ranging from fine clay to large boulders, that are produced in the upper part of river basins by weathering of mountain rocks and, as a result, it is composed of a variety of rock minerals. Silicates are the main constituents of rocks, the most diffused of which are feldspar and quartz, which are very resistant minerals that can travel long distances without loosing integrity. Other diffused minerals are carbonates, that are the basic constituents of sedimentary rocks, like limestone and dolomite. Limestone is a far less resistant rock that easily degrades to silt eventually leading to its total dissolution into water and, as such, clastic limestone sediment is hardly ever found at locations far from its source. Lesser abundant rocks in the

crust of the Earth include basalt, granite and more esoteric variants such as those composed of magnetite. The *specific gravity* of the sediment, that being the ratio between the sediment density and the density of the surrounding fluid, depends on the type of parent rock the sediment derives from. This is a crucial factor in determining sediment entrainment and transport.

During its gradual descent from the mountain slopes to the abyssal plains, sediment is transported by gravitational forces acting on the solid particles or on the fluid flows thereby transmitting momentum to the particles via drag. Sediment motion begins high up on mountain slopes where the raindrops cause sheet erosion and rapid snow-melts trigger rock slides. Rocky debris that has made its way down the slopes finally deposits as alluvial fans at the base of the mountain fronts. Here, mixtures of coarse material, possibly embedded in a muddy matrix, can be destabilised by heavy rainfalls and can ultimately lead to landslides, debris flows and mud flows. In all these transport phenomena the dominant mechanism of sediment motion is an interplay between gravity and inter-particle friction.

The material eroded in the upper part of river basins reaches river networks and the sediment that does make it this far is further mobilised by river streams through river channels, which act as conduits for sediment movement. Streams entrain sediment; the stronger the flow, the larger the amount of sediment in motion. Throughout its fluvial journey, sediment is continually altered as a consequence of selective sorting and particle abrasion and so, proceeding further downstream, the *sediment mixture* at the river bed undergoes progressive fining. In the upper part of the watersheds, gravel-bed streams are characterised by poorly sorted sediment mixtures whereas, further towards the ocean, sand bed streams dissecting the floodplains are characterised by well sorted mixtures. A noteworthy property of sediment mixtures is its *grain size distribution* and, as grains display different shapes depending on the amount of abrasion they incur, it is necessary to define a conventional grain size so as to give an overall average. Such a categorisation is carried out in different ways, the most common of which is by sieving, which is employed for mixtures consisting of grains ranging from silt to fine gravel. It is thus possible to determine the grain size distribution by defining the cumulative distribution function for a given grain size, which is the fraction of the sample weight which contains only grains smaller than the given size. Furthermore, sediment mixtures are also characterised by their *porosity*, that being the ratio between the volume of the voids in a given sample and its total volume. Sediment mixtures in natural environments have different porosity depending on their grain size distribution.

Where rivers meet the ocean, hydraulic sediment transport is significantly affected by tides, winds and waves. Here, sediment does not only originate from fluvial networks, but may also originate from the erosion of coastal cliffs, the decomposition of sea shells and other marine organisms. Finally, in the very last part of its journey, sediment sinks from the coastal regions to the abyss. Turbidity currents carry suspended sediment across the continental shelf down to the deep sea. Severe sea storms, submarine landslides, or sediment-laden river outflows can mobilise significant amounts of sediment in suspension which, in turn, may reach the inlet of submarine canyons. Mixtures of water and sediment approaching canyon inlets have a density higher than the surrounding water and thus they move down the canyon slopes in the form of turbidity currents until the flat abyssal plains. Here, the currents decelerate leading to the settling of the sediment and, as a result of geological diagenesis, offshore sediment deposits eventually evolve into deep water rocks, called turbidities.

Throughout the sediment cycle briefly illustrated, natural fluid flows interact with the erodible surface of the Earth by sediment transport. *Mechanics of sediment transport* refers

to theories and experiments concerning the physical mechanisms that drive the transport of granular particles by fluid flows and, as such, it pertains to the motion of two phase flows, one phase being fluid and the other solid. In the following, attention is drawn to the sediment transport exclusively due to the action of water flows typically encountered in fluvial and coastal environments. Here, the concentration of sediment tends to be rather dilute throughout the water column, although this does increase towards the bottom where it attains significant values only in a thin layer confined to the liquid-solid interface. As a consequence, it is generally assumed that large scale water flows are not affected by the presence of the solid phase. The inherent turbulent nature of these flows further complicates the picture. Intermittent turbulent sweeps close to the ground and intense random ejections

Figure 1.4: Sediment laden outflow of the Yukon River, Canada. © Georgia Scardamaglia.

entrain sediment particles tending to lift them upwards. Inelastic collisions of the transported particles with those particles resting at the ground complicate the matter as these collisions cause an increase of the shear stress at the liquid-solid interface where particles at rest can be resultantly mobilised. All that being said, the mechanics of sediment transport constitutes an interesting field in its own right.

Water flowing over an erodible bottom is able to entrain sediments in various modes of transport which depend on the strength of the carrier flow, that determines the amount of sediments the flowing water is able to transport, the *flow transport capacity*. At the lower stages of transport, moving particles slide and roll over the bottom, but with only a small increase of the flow, these particles lift up from the bottom tracing out ballistic trajectories. This mode of sediment transport is known as saltation (Lat. *saltare*). Saltation is mainly governed by the action of hydrodynamic forces exerted on the granular particles by the carrier flow, as well as by the downward action of gravity and, in addition, by the collision of the transported particles with those resting at the bottom. Saltating sediments leap in the vicinity of the bottom within a layer that is only a few grain diameters thick, known as the *saltation layer*. Here, transported particles exhibit a complex dynamics which is driven by, but different from, the dynamics of the fluid particles. At higher stages of transport, the water flow entrains finer sediment throughout the water column into *suspension*. The suspended sediments, captured by coherent vortices, escape the saltation layer in the form of intense ejections that come as a result of the increased turbulence of the flow. These lightweight particles are then advected by the flow in a dynamic process which differs from that of fluid particle motion only for their tendency to re-settle. As saltation and suspension clearly turn out to be the major modes of hydraulic sediment transport, it is possible to ideally split the total hydraulic sediment load into *bed-load* and *suspended-load*. The former consists of sediments mainly saltating over each other, never rising too far from the bed, whereas the latter consists of sediments drawn into suspension. In gravel-bed rivers, sediments are transported mainly as bed-load, and conversely, in sand-bed rivers as well as in coastal regions, bed-load and suspended-load coexist.

Whether the mode of transport is saltation or suspension, flow turbulence typically prevents a clear definition of the hydraulic conditions required for *incipient sediment transport*, a major issue regarding the mechanics of sediment transport. It is nevertheless possible to define threshold conditions below which sediment transport can be neglected for many practical purposes. Experimental findings suggest that a uniform water flow over a cohesionless erodible surface is unable to entrain sediments below a critical value of the ratio between the drag force and the resistive frictional force acting on these sediments. This is the parameter set out by Shields (1936), who deduced, from dimensional analysis of his set of pioneering laboratory experiments, a formulation of the threshold conditions for incipient sediment transport in terms of a dimensionless measure of the *bottom shear stress*. It is possible to obtain an explicit formulation of the relation explored by Shields by means of a mechanistic model for the incipient motion of an idealised spherical particle protruding upwards from an erodible flat surface, assuming that drag and lift forces due to a uniform laminar flow are applied to the centre of the particle. This simplified model highlights the main sources of uncertainty, such as drag and lift coefficients, particle shape and location, and it explains why it is so difficult to define the threshold conditions for incipient sediment transport in a deterministic way.

Sediment transport models attempt to predict sediment erosion, transport and deposition rates for given hydraulic conditions. In principle, a rigorous modelling would reproduce a

rough turbulent shear two-phase flow accounting for mutual interactions between the two phases. Such modelling is currently beyond today's theoretical and computational capabilities and consequently approximate models are commonly used. Although advanced numerical models do exist that are able to capture not only the feature of the mean water flow but also its intermittent turbulent structures, flow models usually solve simplified forms of the *Navier-Stokes Equations*, such as Saint Venant Equations, Shallow Water Equations and Reynolds Averaged Equations, being respectively one-, two- and three-dimensional. One-dimensional flow models are applied to sedimentation processes in fluvial channels, whereas two- and three-dimensional models can be applied to sedimentation processes in floodplains, estuaries and coastal regions. Adding to these limitations, common practises for predicting hydraulic sediment transport directly from the knowledge of the forcing flow are based on heuristic approaches whose intrinsic uncertainty affects the reliability of sediment transport predictions.

Most of these approaches have a somewhat theoretical basis but depend mostly on experimental data for their quantitative aspects. A large assortment of sediment transport *predictor relations* exist that have being customarily integrated into computer programs for sediment transport modelling. Selection among different predictors, algorithms, or procedures must be based on comparisons between different methods. Whenever possible, model calibration against real data is highly recommended in order to set the correct values of the various hydrodynamic and sediment parameters which features the most commonly-quoted relations.

## 1.4 Research questions, methodology and outline of the thesis

The present study is intended to be a contribution to the theory of sand dune stability which comprises the effects of sediment starvation. In this section, the list of the main research questions is introduced, followed by the adopted methodology and finally the subsequent chapters of the thesis are outlined.

**Q1.** What is known about the effect of sediment starvation on the formation of sand dunes?

**Q2.** Can the effect of sediment starvation on sand dune formation (Q1) be reproduced by laboratory experiments that simulate the appearance of fluvial dunes in steady currents, and how do the experimental findings then compare to the outcome of previous laboratory and field observations?

**Q3.** Can the effect of sediment starvation on sand dune formation (Q1) be reproduced by an idealised process-based model, and how do the model results compare to the results of the laboratory experiments (Q2)?

**Q4.** Can the idealised modelling of the starved dune formation in steady currents (Q3) be extended to reproduce the effect of sediment starvation on the formation of tidal dunes, and, if so, how do the results of the model compare to field observations?

By following a rigorous scientific method, the present investigation entails few fundamental steps. The first of which concerns the *description of the phenomenon* and considers both laboratory and field observations. Since data on this topic is limited and an apparent contradiction exists in the literature between laboratory measurements and field surveys, a *physical modelling* is described here that investigates the effects of sediment starvation on the morphology of sand dunes. The main outcome of this experimental study is that the volume

of sediment available for transport affects the formation of sand dunes as a reduction in the sediment availability implies longer dunes with a more three-dimensional morphology. According to this experimental outcome, the following hypothesis is deduced that represents the novelty of the present contribution. *When a motionless substratum is exposed by the growth of sand dunes, the lack of sand affects the sediment transport, and, in turn, the dune morphology*. This leads to the *tendency of starved dunes to increase their wavelength because of sand deficit* which is consistent with the above introduced experimental measurements. Also, *starved bedforms become more irregular* which is consistent with previous field observations. The aforementioned hypothesis is then formulated through *numerical means*, by modelling the sediment transport under supply-limited conditions, and is developed in the framework of the stability theory of fluvial dunes. The main outcome of such *theoretical modelling* is qualitatively and quantitatively in agreement with the experimental measurements presented in the following subsection. The final step of the investigation consists of testing the aforesaid hypothesis in the more complex framework of the stability theory of tidal dunes. A more sophisticated hydrodynamic model is introduced to properly simulate the oscillatory tidal flow and an extension of the tidal dune stability is ultimately proposed that includes the effects of sediment starvation. Finally, a comparison of the model predictions to previous field observations is made that supports the reliability of the *idealised modelling*.

### 1.4.1 Chapter 2

A physical model which investigates the formation of starved dunes in steady currents is presented herein. This is to be used to provide data on a topic in which measurements are limited and shed light on the apparent contradiction found in the literature. To do so, a set of laboratory experiments is presented that investigate the relationship between dune morphology and sediment starvation. An open channel flow in a laboratory flume is realised that forces an erodible and hydraulically rough sandy bottom in a flow regime for which continuous intermittent sediment transport occurs. Cohesion-less sand is used as artificial roughness and, at the beginning of each experiment, the same sand is uniformly spread on the flume bottom to generate an initial layer of sediment with a constant thickness. The series of experiments are then thoroughly described which are conducted by fixing all the hydrodynamic and morphodynamic parameters except the thickness of the initial layer of mobile sediment. Another fixed parameter is the duration of each experiment which is sufficient for the formation of sand dunes over the entire length of the flume that is observed in both alluvial and supply limited conditions. Laboratory measurements indicate that the exposition of the rigid bottom of the flume strongly affects the morphology of starved dunes, the average spacing of which increases with a decreasing sediment availability.

### 1.4.2 Chapter 3

A numerical model of the formation of starved dunes in steady currents is presented which represents an extension of the linear stability analysis by Colombini (2004) that takes into account the effect of sediment starvation on the formation of fluvial dunes. A steady turbulent free-surface water flow through a wide straight channel is studied in a two-dimensional Cartesian coordinate system with the horizontal axis along the channel axis, and the vertical axis over the depth pointing upwards with the origin at the bottom. The presence of

two-dimensional dunes with crests orthogonal to the direction of the flow is considered. Assuming that the dune amplitude is much smaller than the local water depth, the flow field can be evaluated by means of a perturbation approach. Such an assumption is reasonable for initial-instability stages of the pattern formation and is a necessary condition for the below described stability analysis. By regarding the bottom geometry as periodic, the sandy bed can be expressed as superposition of different spatial components, the number of which should be large enough to describe the discontinuity of the starved bottom profile. Analogously to the above described physical modelling, the profile of the dunes is thought to arise as a result of the instability of a thin layer of sand which initially is homogeneously lying over a motionless substratum. The hydrodynamic problem can be split into the evaluation of a basic flow field, which describes the steady flow over a flat bottom, and a set of linearly independent differential problems, which describe the perturbation of the flow field owing to the presence of sand dunes. As fluvial streams are known to be characterised by high Reynolds number values, the determination of the flow field requires the introduction of a turbulence model. The two-dimensional Reynolds-Averaged-Navier-Stokes equations are numerically integrated to evaluate the basic flow field, under the shallow water approximation, as well as the perturbed flow field, which is solved in a full two-dimensional form. At the free surface, the dynamic boundary condition forces the vanishing of the shear stresses and the kinematic boundary condition is also imposed. Close to the bottom, the flow velocity vanishes at a distance from the seabed which is related to the bed roughness. The hydrodynamic problem is closed by simply introducing a self-similar solution for the kinematic eddy viscosity, and then Reynolds stresses are quantified by the Boussinesq relationship. Information about the net sediment transport can be obtained directly from the knowledge of the perturbed flow field through evaluating the bed shear stress, along with the relative Shields parameter, and by also introducing a suitable sediment transport predictor formula. Suspended sediment transport is neglected at this first stage of the modelling and only bed-load sediment transport is considered. The time development of the sandy bottom can be estimated by introducing the sediment continuity equation (Exner equation), which lies at the heart of the morphodynamic model. By linearising all the morphodynamic formulae and coupling them with the linear hydrodynamics previously described, it is possible to perform a linear stability analysis. To do so, small amplitude bottom perturbations and related sediment transport rates are expressed as exponential functions in time and space and then investigated separately. Directly from the linearised sediment continuity equation a dispersion relationship is straightforwardly obtained. The morphodynamic time development of the generic bottom perturbation turns out to be exponential, and thus its complex argument describes the growth (decay) of the amplitude, with its imaginary part, and the migration of the crest, with its real part. Finally, assuming that the most unstable mode prevails over all the others, the main features of the sand dune which is more likely to occur can be predicted depending on the values of the flow and sediment parameters.

The numerical approach described by Blondeaux et al. (2016) is adopted to take into account the effect of sediment starvation on sediment transport. When local entrainment of sediment is prevented by the presence of a motionless substratum, the amount of sediment in motion is smaller than the local transport capacity and the evaluation of the sediment flux calls for a numerical procedure. Where locally no sand is available, sediment transport depends on the bed shear stress and its spatial derivative. If the shear decreases in the direction of the main flow, the sediment transport rate is provided by the sediment transport predictor formulas and some deposition thus occurs in line with sediment continuity. Conversely, if the

shear increases in the flow direction, the sediment transport rate cannot increases as, locally, no further sediment is available for transport, and, therefore, its local value should be equal to the upstream value. Numerical simulations of the time development of a bottom configuration starting from an initial small amplitude perturbation are presented. by integrating the sediment continuity equation along the longitudinal coordinate and over the morphodynamic time. A comparison with the laboratory measurements described in the previous subsection is made by choosing a simulation-time-window and flow and sediment parameters so that they fall in the range of values typical of the laboratory experiments. Numerical results confirm the lengthening of the starved dunes as the initial sand layer thickness decreases in fair agreement with the aforementioned experimental measurements.

### 1.4.3 Chapter 4

In those submarine regions where sediment starvation does not allow the formation of typical tidal dunes, field observations reveal regularly spaced amorphous mounds of sand. For similar hydrodynamic and morphodynamic conditions, these sandy mounds are characterised by crest-to-crest distances which are larger than those of typical tidal dunes. In particular, sandy mounds were observed by Le Bot (2001) in the middle of English Channel between Calais and Dover.

A numerical model of the formation of starved dunes in oscillatory tidal currents is presented which represents an extension of the linear stability analysis by Besio et al. (2006) that takes into account the effect of sediment starvation on the formation of tidal dunes by including the numerical procedure outlined by Blondeaux et al. (2016). In order to compare the numerical findings with the results of a classical linear stability analysis, a *numerical growth rate* for the generic harmonic component is defined by simply integrating the dispersion relationship over the morphodynamic simulation time. Such *numerical growth rate* can be then compared to the *analytic growth rate* provided by standard linear stability analyses. If tidal dunes develop in a sand rich environment, the initial growth of the unstable bottom perturbations is exponential and the value of the *numerical growth rate* matches the value of the *analytic growth rate* predicted by the linear stability analysis. On the other hand, if tidal dunes develop over a motionless substratum, the supply limitation affects the growth of the perturbations, especially those with small wavelengths. The lengthening of the fastest growing mode predicted by the model is analogous to that observed by Blondeaux et al. (2016) for sea-wave-ripples. Numerical results suggest that the mound-to-mound distance which is more likely to occur is larger than the crest-to-crest distance of typical tidal dunes in analogy with the field observations by Le Bot (2001).

# Chapter 2

# An Experimental Investigation on the Formation of Starved Dunes in Steady Currents


## Abstract

Field observations indicate that alluvial bedforms, that are sedimentary patterns observed where mobile sediments entirely cover a underlying motionless substratum, differ from starved bedforms, that are sedimentary patterns observed where a motionless substratum is exposed by their appearance. Laboratory experiments were designed to investigate the effect of sediment starvation on the formation of fluvial dunes. Three series of experiments were conducted in a laboratory flume by fixing all the hydrodynamic and morphodynamic parameters except the volume of mobile sediments that was uniformly spread over the rigid bottom of the flume prior to each experiment. At the end of all the experiments, which lasted for the same amount of time, the formation of alluvial dunes and starved dunes was observed. The main outcome of this experimental investigation is that the volume of sediment available for transport affects the formation of fluvial dunes. As the initial volume of mobile sediments decreases, the rigid bottom of the flume was exposed progressively earlier during the experiments and laboratory measurements clearly indicate the tendency of starved dunes to lengthen, the stronger the sediment starvation, the longer their final crest-to-crest distance. Furthermore, as the sediment starvation attains its maximum value, the dune morphology becomes more irregular: two-dimensional starved dunes turn into amorphous sandy mounds that eventually separate onto three-dimensional barchan dunes.

## 2.1 Introduction

In many natural environments, the morphological patterns which are commonly observed where large amounts of mobile sediment are available (i.e. alluvial bedforms) differ from those which form where the mobile sediment is insufficient to cover an underlying body of sediment which cannot be moved by the flowing fluid (i.e. starved bedforms). Isolated bedforms which migrate over flat immobile terrains are observed in aeolian environments and their geometric and kinematic characteristics are consistently different from those of the bedforms observed along the deserts where sand is profuse, e.g., Allen (1968), Howard et al. (1978), Wippermann and Gross (1986). Field surveys seem to indicate that for similar conditions, the crest-to-crest distance of the starved bedforms is consistently larger than that of the bedforms which form where the sand is abundant. In the left panel of Figure 2.1, the crest-to-crest distance of the desert dunes in the lower part of the photo, where less sand is present, appears to be longer than the crest-to-crest distance of the dunes that can be identified in the upper part of the photo, where more sand is present. The tendency of bedforms to elongate when they enter regions characterised by a scarcity of mobile sediment is also curiously shown by some images of the large dunes photographed on the surface of Mars (see the right panel of Figure 2.1, where the crest-to-crest distance of the bedforms in the lower part of the photo is smaller than that of the bedforms in the upper part of the photo where mobile sediment is present only in the form of three-dimensional barchan dunes).

A similar trend is observed in subaqueous marine environments where the sediment is mobilised by the oscillatory flow generated by the propagation of tidal waves. For example the field observations of Le Bot (2001), which were carried out in the English Channel through the central part of the Calais-Dover Strait where strong tidal currents prevent the uniform deposition of sediments ultimately leading to sediment starvation, show the presence of bedforms with geometric and kinematic characteristics that are similar to, but different from, those of typical tidal dunes. In particular, these amorphous sandy mounds exhibit an averaged spacing which is larger than the wavelength of tidal dunes that are observed in the same surveyed area where sand is abundant (Figure 2.2).

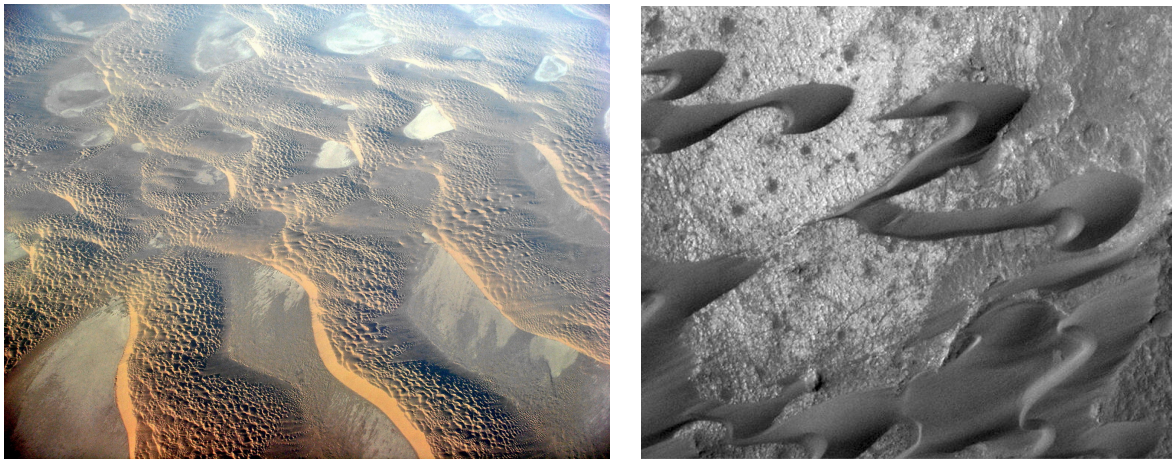

Figure 2.1: Left panel: Dunes of the Taklamakan Desert (courtesy of Beno Saradzic). Right panel: Barchan dunes on the surface of Mars (credit: photo by NASA). Flow is from left to right.

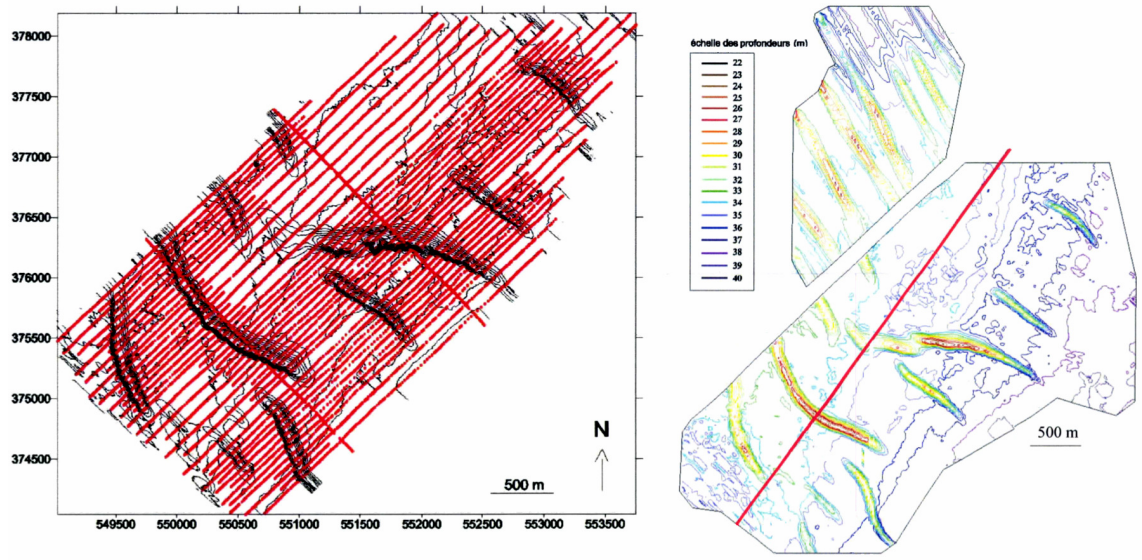


Figure 2.2: Example of a complete survey realised through the Calais-Dover Strait (SHOM/MHA, 1992). Two morphologically contrasted sectors are clearly identifiable: a North-West sector where sand is abundant and regular tidal dunes shape the seafloor and a South-East sector where sand is present only in the form of amorphous sandy mounds interspersed with exposed pebble lags (courtesy of Sophie Le Bot).

Furthermore, in both aeolian and marine environments, a definable suite of starved bedforms develops (Venditti et al., 2017). In the Celtic Sea, where sandy patches overlay gravel lags, Kenyon (1970) distinguished marine sand ribbons, barchanoid sand waves and isolated dunes depending on the thickness of the sand cover and the strength of the forcing tidal currents. A similar sequence of bedforms is observed in fluvial environments (Kleinhans et al., 2002). Rivers typically show an abrupt transition from gravel to sandy bottoms as channel slopes decrease and, in many cases, seasonal and perennial gravel-bed rivers exhaust the supply of sediment their streams can entrain. In such cases, the finer sediment is mobilised as bedload transport while the mean grain size becomes coarser at the bed surface and, as such, poorly sorted river beds subject to periods of low flows or discharge waves undergo a transient degradation until they are fully armoured (Parker et al., 1982). Whereby an armour layer develops, but finer sediment continues to be available, a definable suite of starved bedforms develops. As the sediment supply from upstream increases, a gradual transition occurs starting from longitudinal sand ribbons to three-dimensional barchans that eventually coalesce onto amorphous sandy mounds ultimately leading to the appearance of two-dimensional transverse dunes (Kleinhans et al., 2002). By means of a very simple phenomenological experiment, Venditti et al. (2017) revealed that this sequence of bedforms emerges in steady currents as the sediment supply increases. They fed fine sand to a Plexiglas channel showing that the aforementioned gradual transition can be observed even under the simplest experimental conditions. In particular, it is the volume of sediment supply that sets the types of the emerging bedforms (Figure 2.3).

However, in the case of fluvial dunes, how sediment starvation affects the morphology of the bedforms is still unclear. Only a few observations of starved bedforms generated by steady currents in subaqueous environments are available and measurements do not indicate a clear

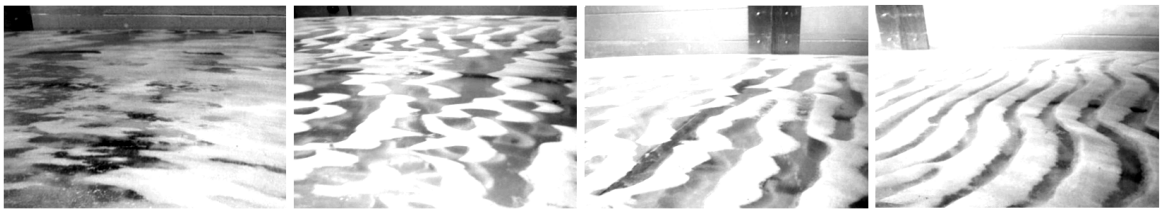

Figure 2.3: Sequence of supply limited patterns generated by a steady flow over a Plexiglas rigid bottom with increasing sediment supply (Venditti et al., 2017). Panel 1: sand patches akin to longitudinal sand ribbons; Panel 2: fully three-dimensional barchans; Panel 3: interconnected barchanoid dunes; Panel 4: two-dimensional transverse dunes.

trend. Carling et al. (2000) described the geometry of the starved dunes observed in a supply-limited reach of the Rhine river (Germany), showing the presence of different morphological patterns: ripples, small dunes and large dunes. Their data suggest that sediment starvation manifested itself by giving rise to isolated, amorphous dunes interspersed with plane gravel lags. Moreover small transverse dunes are observed, the crest-to-crest distance of which changed as they migrate from the gravel lags to the stoss side of the isolated mounds. In particular, similarly to the observations of Le Bot (2001), the spacing of the small dunes is longer when they move above the gravel lags. In contrast, the laboratory measurements carried out by Tuijnder et al. (2009) seem to indicate the opposite: bedform size (both length and height) decreases as the volume of mobile fine sediment decreases and the immobile coarse bottom is exposed.

The laboratory experiments described in the following were designed to provide further data on the effects of sediment starvation on the formation of sand dunes generated by steady currents in subaqueous environments. Three sets of experiments were performed by fixing all the hydrodynamic and morphodynamic parameters except the thickness of the layer of sediment initially available for transport, thus allowing for a consistent comparison between the geometric characteristics of the starved bedforms and that of the alluvial bedforms. The duration of the experiments was kept fixed in order to investigate only the effects of sediment starvation on the dune morphology.

In the next sections the experimental apparatus, the different methods apply to collect measurements and the adopted experimental procedure are respectively described. The experimental results are summarised in Section 4.3 and a thorough discussion of the comparisons with previous field and laboratory observations is made in Section 2.6. The conclusions are drawn in the final section.

## 2.2 Experimental Apparatus

The experiments were made in a laboratory flume $12$ m long, $0.4$ m wide and $0.3$ m deep which was mounted on a beam, the slope $(S)$ of which could be easily adjusted even during a single experiment. The water flowed along the flume from a head tank filled by a $100$ mm pipe. The pipe line was equipped with a $70$ mm flow nozzle connected to a differential manometer which allowed the measurement of the flow discharge $(Q)$ that was generated by a pump and regulated by a special valve. A sluice gate was placed at the end of the flume to control the water level $(H)$ in order to generate a uniform flow along the channel

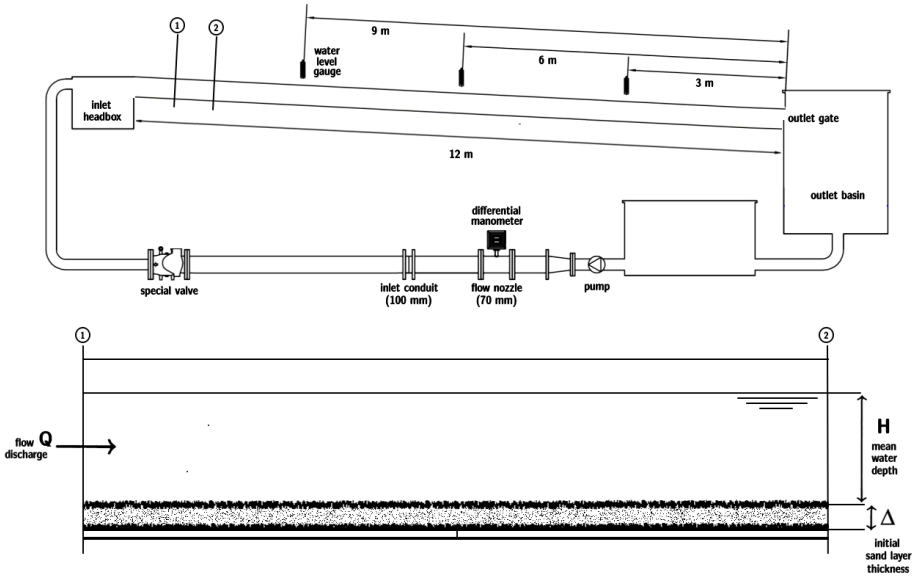


Figure 2.4: Sketch of the experimental apparatus.

according to a rating curve established through some preliminary fixed-bed runs. In all these preliminary tests that are thoroughly described in the following, the free surface and the fixed bed were indeed remarkably parallel, up to the accuracy of the water level measurements ($<$ $1$ mm). Hence, the water flowed over the gate to fall in a second tank from which the supply pipe departed.

Well sorted sand grains characterised by a mean diameter $d_s$ equal to $1.12$ mm were glued on $6$ PVC slabs $200$ cm long, $40$ cm wide and $2$ mm thick which, in turn, were fixed to the flume bottom thus creating a rough bed. Before the pump was switched on and the water started to flow throughout the channel, the same sand was spread on the rough fixed bottom to generate a layer of sediment with a constant initial thickness $\Delta$ throughout the entire length of the flume.

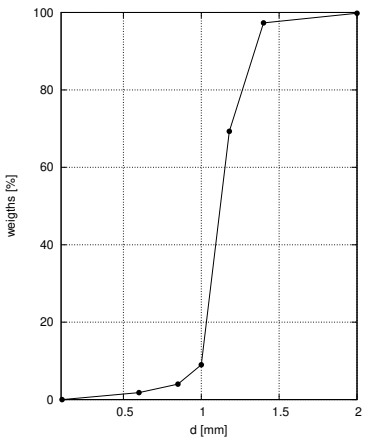


Figure 2.5: Grain size distribution evaluated by the sieve analysis of the well sorted sand.

## 2.3 Experimental Measurements

### 2.3.1 Side Wall Correction

When open channel flows and sediment transport are investigated in narrow flumes, the evaluation of the shear stress at the bottom is decisive. Because of the flume width is usually narrow compared with the flow depth, the side walls affect the bottom shear stress. If the bottom is rougher than the side walls, as in the present experimental investigation, the distribution of the shear along the wetted perimeter of the channel is nonuniform. All this being said, experimental outcome cannot be expected to correspond to field observations unless a correction for the shear stress at the side walls is made. An equivalent roughness length characterising the sediment glued on the bottom of the flume and its relative flow scale, which is the description of the uniform flow depth as function of the flow discharge and the channel slope (c.f. Figure 2.7), were evaluated by dividing the shear stress in a wall and a bottom part by accounting for the side wall correction.

Einstein (1934) determined an equation for the side wall correction based on the flow resistance making some special assumptions. Essentially, the procedure outlined by Johnson (1942), later simplified by Vanoni and Brooks (1957), was employed. The entire cross-section is partitioned into two sub-regions $\Omega_B$ and $\Omega_W$ corresponding to the bottom and the side walls, respectively. Hereinafter subscript B and W refer to bottom and side walls, respectively, while the variables without subscript are referred to the entire cross-section. These different sub-regions are thought as two independent parallel channels with the same mean velocity $U$ and longitudinal slope $S$ (c.f. Figure 2.6).

Flow measurements were performed for different channel slopes by adjusting the level of the downstream sluice gate depending on the imposed flow discharge $Q$ once uniform flow conditions were established. The critical flow conditions were determined directly from the geometry of the flume cross-section for any realised couple of flow discharge and channel slope. Initially, assuming an uniform distribution of the roughness along the wetted perimeter, a preliminary estimate of the uniform flow was performed. A comparison in terms of uniform flow depth $H$ between the roughly predicted values and the measurements supported the reliability of the experimental apparatus. At this early stage of the physical modelling, the cross-sectional roughness length $k_s$ was assumed to be a given multiple of the mean grain size $d_s$ of the sediment, accordingly to the Nikuradse sand roughness ($k_s \sim 2.5 d_s$). The mean flow velocity $U$ was evaluated simply dividing the imposed discharge by the measured flow depth and the channel width $B$.

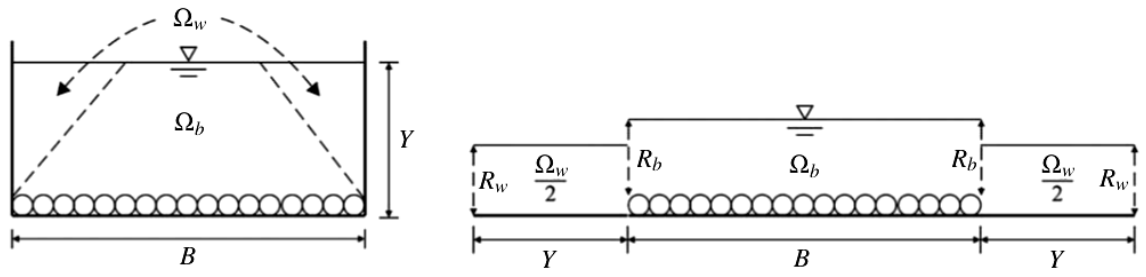


Figure 2.6: Sketch describing the side wall correction *modus operandi*.

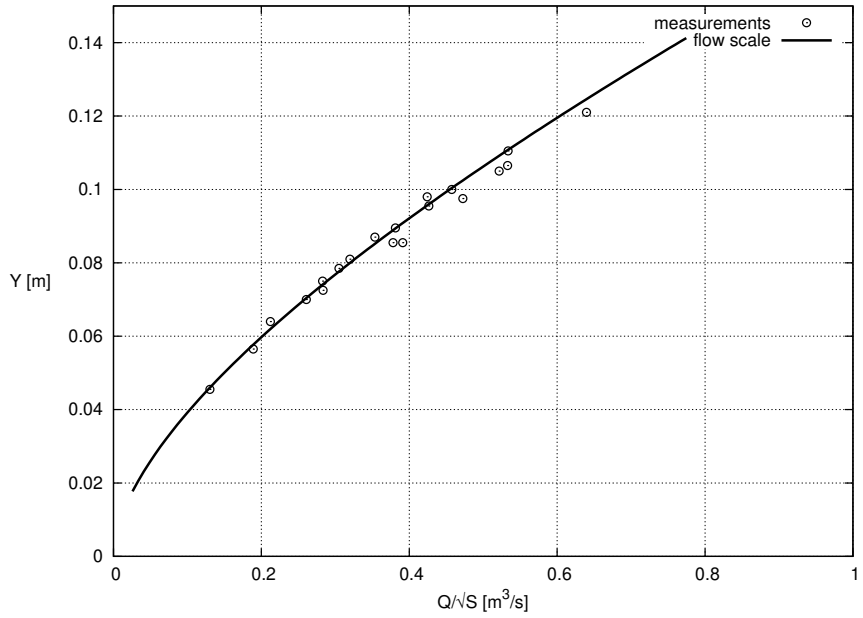


Figure 2.7: Flow scale curve of the slope varying flume with sediment ($d_s = 1.12$ mm) cemented at the bottom giving an equivalent roughness length $k_{s,eq} = 4.85$ mm computed by means of the side wall correction. Points are experimental measurements.

The Rouse equation relates the hydraulic radius $R = BH/(B+2H)$ with the conductance coefficient $C$, or alternatively with the friction factor $F$, which is an indirect measurement of the total shear stress. Analogously to the mean flow velocity and the channel slope, the Rouse equation was applied to both sub-regions.

$$U = C\sqrt{gRS} = \sqrt{\frac{8}{F}gRS} = \frac{Q}{BH} \Rightarrow \frac{U^2}{8gS} = \frac{R}{F} = \frac{R_W}{F_W} = \frac{R_B}{F_B} \tag{2.1}$$

The PVC side walls were considered hydrodynamically smooth, their conductance coefficient (friction factor) was related to the corresponding hydraulic radius by the Keulegan equation for smooth flow regime

$$C_W = \sqrt{\frac{8}{F_W}} = \frac{1}{\kappa}\log\frac{Re_W\sqrt{F_W}}{3.41}, \tag{2.2}$$

where $\kappa$ is the von Karman constant and $Re_W = ReR_W/R$, $Re = UH/\nu$ is the Reynolds number of the flow. In analogy with the flow cross-section, the wetted perimeter can be partitioned into a bottom-related part, which equals the channel width, and a wall-related part, which is equal to twice the mean flow depth. Consequently the water continuity requires that

$$F = \frac{BF_B + 2HF_W}{B+2H} \Rightarrow F_B = \frac{F(B+2H) - 2HF_W}{B}. \tag{2.3}$$

Once the Keulegan equation for the rough flow regime was applied to the sandy bed, the evaluation of the bottom friction factor by means of the above relationship translated into the estimate of the effective roughness length $k_{s,eff}$.

$$C_B = \sqrt{\frac{8}{F_B}} = \frac{1}{\kappa} \log \frac{11.09 R_B}{k_{s,eff}} \tag{2.4}$$

The effective roughness length was then calculated for each measured triple $Q$, $S$, $H$. Thus, an equivalent roughness length $k_{s,eq} \sim 4.3 d_s$ was obtained by simply averaging the outcome of the above procedure. The equation system composed by (2.1)-(2.4), where the effective value of the roughness length is substituted with its equivalent counterpart, constitutes an implicit set in the unknowns $F_W$, $R_W$, $F_B$, $R_B$. Solving the system of implicit equations iteratively, the flow scale of the channel was deduced (c.f. Figure 2.7), and the principal unknowns of interest were found. Thereby, a uniform rough wide open channel flow was determined, which is related to the uniform flow realised in the narrow flume, by interpreting the bottom hydraulic radius as its mean water depth $D = R_B$ that is related to its Froude number $F_R = U/\sqrt{gD}$ and allows to evaluate the dimensionless equivalent sediment grain size $d = d_s/D$, which, in turn, is related to the representative bottom conductance coefficient

$$C = \frac{1}{\kappa} \log \frac{11.09 D}{k_{s,eq}} = \frac{1}{\kappa} \log \frac{2.58}{d} \tag{2.5}$$

Of note, the Froude number characterising the uniform rough wide open channel flow related to the individual experiment turns out to be larger than its measured value. It is then possible to evaluate the bottom shear stress $\tau$ and its related Shields parameter $\Theta$ to be associated with the uniform rough wide open channel flow as follows

$$\tau = \rho u_\tau^2 = \rho g D S = \rho \frac{U^2}{C^2} \ , \quad \Theta = \frac{\tau}{\rho g (s-1) d_s} \ , \tag{2.6}$$

where the relative density of the sediment $s = \rho_s/\rho$ is introduced. This experimental post-process is crucial in order to generalize the results of the present physical model by defining global dimensionless quantities of interest (e.g. $F_R$, $d$, $C$, $\Theta$) which are independent on the flume width. All that being said, the side-wall correction allows to extend the results of the flume experiments described in the following to real rough wide open channel flows and related theoretical models (see Chapter 3).

### 2.3.2 Laser Scanning

Accurate measurements of the geometrical characteristics of the morphological patterns generated by the open channel flow were made by means of laser scanning surveys. The effective length suitable for the measurements was approximately the downstream half of the $12$ m long channel, where the irregularity of the incoming flow and the related upstream scour did not affect the formation of the dunes. The accuracy of the measurements strongly depends on the distance between the location of the laser scanner and the farthest position at which the three-dimensional coordinates of the bed elevation were evaluated. In order to achieve a high resolution, three different scans of each final bottom configuration were made placing the laser instrument roughly over the centerline of the channel at the beginning, in the middle and at the end of a $5$ m downstream test section. The resolution range of the laser system was equal to $0.1$ mm. Therefore, detailed measurements of the bed elevation were obtained.

### 2.3.3 Fourier Analysis

In most of the experiments, the mean geometrical features of the emerging patterns did not vary significantly throughout the downstream half of the flume. The downstream stretch of the channel suitable for the measurement of the geometric characteristics of the bedforms was approximately the downstream half of the channel (test section), where the irregularities of the incoming flow and the related upstream scour did not affect the formation of the morphological patterns. Consequently a preliminary rough estimation of the average wavelength (crest-to-crest distance) of the bedforms was performed by simply dividing the distance between the most upstream and the most downstream crests by the number of crests observed therein minus one.

However, in some experiments, the increased flow discharge forcing the progressively decreasing initial sand layer thickness leads to strong sediment starvation that ultimately results in the appearance of very three-dimensional bottom configurations. Thus the aforementioned simple procedure can become questionable for describing three-dimensional bedforms, when the definition of their crests and troughs is less clear. Hence, a detailed topographic survey of the bed was acquired by laser scanning. In particular, the Imager 5006i phase-based laser scanner, manufactured by Zoller + Frohlich, was used to measure the bottom profile from three different measuring stations, thus obtaining three sets of values of the bottom elevation which were interpolated on a regular grid by means of a MATLAB subroutine. The accuracy of the measurement procedure was quite high and the measurements of the bed elevation were affected by an error smaller than $1$ mm, mainly due to the random position of the sand grains. In order to gain reliable information on size and shape of the bottom forms in both the streamwise and the spanwise directions, a two-dimensional Fourier analysis was applied to a selected stretch of the downstream test section. Data were mirrored with respect to one bank to handle diagonal fronts, so that the first transverse mode turns out to have a wavelength which is twice the channel width, thus corresponding to an alternate pattern. The stretch of the downstream test section was selected in the streamwise direction so as to in-

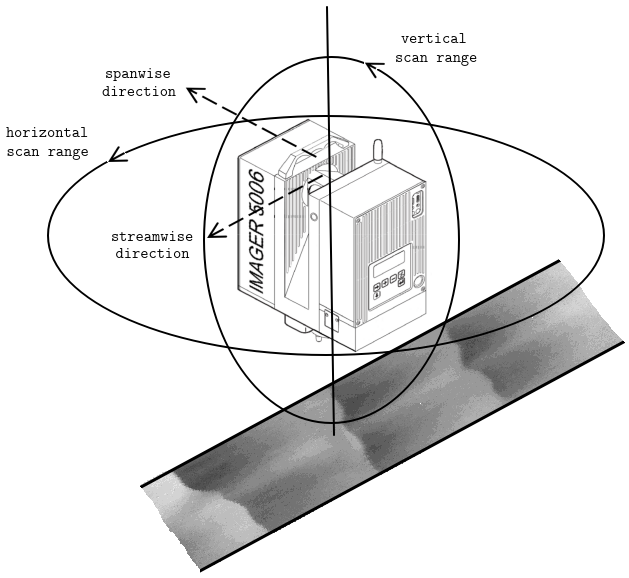


Figure 2.8: Sketch of the laser scanning.

clude only complete bedforms, i.e., the bottom elevation (with respect to the mean value) at the beginning of the stretch is approximately equal to that at the end. This condition makes the length of the selected stretch slightly different from one experiment to another. The two-dimensional Fourier analysis is based on the expansion of the measured bed elevation as follows

$$\eta = \eta_{0,0} + \sum_{n=0}^{N} \sum_{m=-M}^{M} \eta_{n,m} e^{i\frac{2\pi nx}{L}} e^{i\frac{2\pi my}{2B}} + \text{c.c.},$$

where $\eta_{0,0}$ is the averaged thickness of the initial sand layer, $x$ is the streamwise coordinate while $y$ is the spanwise coordinate, $L$ is the length of the selected stretch, $B$ is the measured part of the width of the flume and $c.c.$ indicates the complex conjugate of the quantity that precedes it. The amplitudes $\eta_{n,m}$ have been evaluated by means of a MATLAB routine. Typical values of the truncation numbers N and M are respectively $500$ and $75$. Such a description of the bed morphology allows an accurate quantitative measure of the harmonic content characterising both the streamwise and spanwise evolution of the bottom elevation and then a more accurate estimate of the average wavelength of the emerging patterns that was performed by simply dividing the longitudinal length of the selected stretch by the peak streamwise harmonic component (i.e. the harmonic component in streamwise direction characterised by the largest amplitude).

## 2.4 Experimental Procedure

Three series of experiments were performed, setting the flow discharge $Q$ equal to $20$ l/s, $22.5$ l/s and $25$ l/s, respectively (Table 2.1). In all the experiments, the uniform water depth $H$ over the cohensionless bottom was slightly larger than $0.1$ m, and, more precisely, $0.11$ m in Series 1 and 2 and $0.12$ m in Series 3. It follows that the depth averaged velocity $U$ was about $0.45$ m/s, $0.51$ m/s and $0.52$ m/s, respectively. The reader should notice that the value of $U$ in the third series of experiments is not significantly different from that of the second series because the increase of $Q$ is partially balanced by the increase of the water depth $h$. The initial thickness $\Delta$ of the sand layer was decreased in regular steps starting from a maximum value equal to $2.5$ cm down to $0.5$ cm. The flow was stopped after $30$ minutes from the beginning of each experiment and then the resulting bottom configuration was measured. This duration was chosen on the basis of preliminary tests which showed that, after such time, well-developed bedforms were observed under both alluvial and supply-limited conditions throughout the entire length of the flume. The shear stress $\tau_B$ induced by the flowing water on the sandy bed was large enough to cause sediment transport in the form of bed-load and, although clouds of sand occasionally swirled of the crests of the growing patterns, no suspended load was observed.

## 2.5 Experimental Results

The first experiment S1N1 of the first series was characterised by a value of the thickness $\Delta$ of the initial sand layer equal to $2.5$ cm and $12$ almost two-dimensional dunes were observed at the end of the experiment with an average crest-to-crest distance of $0.47$ m. The left panel of Figure 2.9 show a top view of the final bottom configuration of experiment S1N1, where a stick $1$ m long allows a rough estimate of the dune length. Top-left panel of Figure

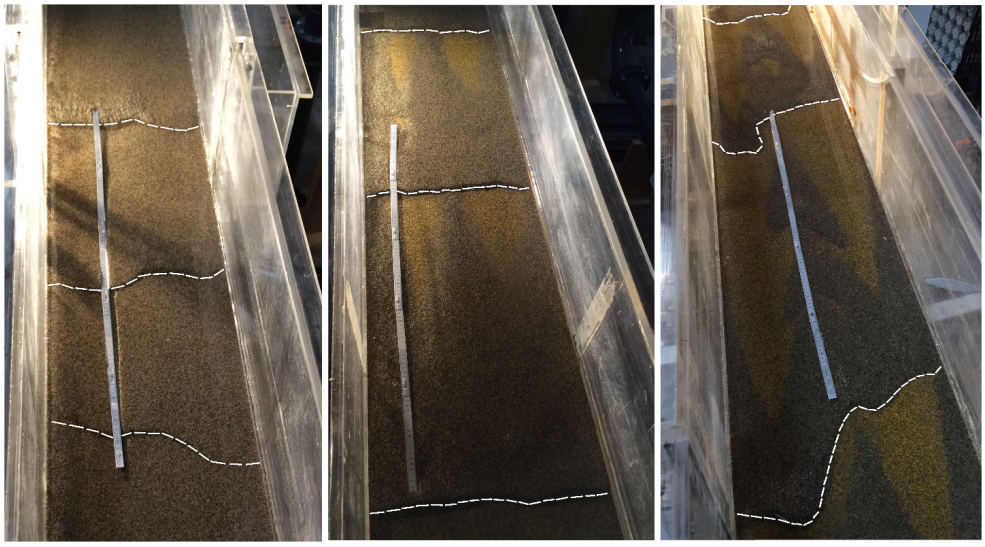

Figure 2.9: From left to right top views of the laboratory flume after $30$ minutes from the beginning of the experiments S1N1, S1N4 and S1N5. The photos clearly show the bottom topography and the presence of the dunes, the crests of which are highlighted by dashed white lines. A stick $1$ m long allows a rough estimate of the crest-to-crest distance.

2.11 shows the bottom profile measured along the selected stretch of the channel for experiment S1N1. The typical triangular dune shape, with a gently sloping stoss side and a steep lee side, can be easily recognised. In the top panel of Figure 2.12, the modulus of the complex amplitude of each harmonic component of the two-dimensional Fourier transform of the bottom elevation $|\eta_{n,m}|$ both in the streamwise and spanwise directions is plotted. The spectrum clearly shows that the $10^{th}$ streamwise component is characterised by the largest amplitude and, as the length of the selected stretch is approximately equal to $4.5$ m, it confirms that the average wavelength of the alluvial dunes is about $0.45$ m. Although the harmonic components characterised by a transverse wavelength equal to the channel width and its multiples have a non-vanishing amplitude, the bottom configuration is practically two-dimensional.

Similar bottom configurations were observed at the end of experiments S1N2 and S1N3 which were characterised by the same values of $Q$ and $H$ but values of $\Delta$ equal to $2$ and $1.5$ cm, respectively. Indeed, for these experiments, the amplitude of the bottom forms, which were generated by the flowing water, was not large enough to bare the rigid bottom. Hence, for both the experiments, the average wavelength of the dunes was equal to about

| $Q$ $[ls^{-1}]$ | $H$ $[cm]$ | $U$ $[ms^{-1}]$ | $D$ $[cm]$ | $\tau$ $[Nm^{-2}]$ | $F_R$ $[-]$ | $C$ $[-]$ | $\Theta$ $[-]$ |
|---|---|---|---|---|---|---|---|
| 20.0 | 11 | 0.45 | 8.8 | 0.94 | 0.48 | 14.7 | 0.052 |
| 22.5 | 11 | 0.51 | 9.4 | 1.19 | 0.52 | 14.8 | 0.065 |
| 25.0 | 12 | 0.52 | 9.8 | 1.22 | 0.53 | 15.0 | 0.067 |

Table 2.1: Overview of the hydraulic conditions imposed in the experimental series and the uniform rough wide open channel flow parameters determined by the side-wall correction.

$0.47$ m. In experiment S1N4, where the thickness $\Delta$ was equal to $1$ cm, the rigid bottom was exposed and the geometrical characteristics of the bottom forms changed. In particular only $9$ bottom forms were observed with an average crest-to-crest distance equal to $0.65$ m. The first series of experiments includes one further experiment which was made with an initial uniform thickness of the sand layer equal to $0.5$ cm. In this case only $6$ bedforms were observed within the downstream half of the channel and the estimated wavelength of the dunes was equal to $0.92$ m. The right panel of Figure 2.9 show a top view of the flume and of the bottom configuration at the end of the experiment S1N5. A rough comparison with the final bottom configuration of experiment S1N1 (left panel) confirms that the dune length measured at the end of the last experiment of the series is nearly twice that of the first experiment. The left panel of Figure 2.10 shows the scans of the bottom profile along a stretch of the channel, which is $5$ meter long, for the first five experiments. The morphological patterns can be readily identified and the lengthening of the bedforms with a decreasing initial sand layer thickness is clearly visible. Most of the final bottom configurations are characterised by the presence of a longitudinal sand ridge along the channel axis, which is particularly evident in the experiments of the first series. The mechanism which gives rise to these longitudinal sand ridges can be related to the existence of secondary cellular flows in the plane perpendicular to the channel axis that are generated by the imbalance of the normal Reynolds stresses in the cross-sectional plane and in particular in the corners of the rectangular section (Gerard, 1978). Figure 2.11 represents the bottom elevation with respect to the rigid bottom of the flume measured along downstream selected stretches of the channel for each experiment of the first series. Left panels of this figure show the bottom profiles recorded at a distance of $10$ cm from the right sidewall of the flume, this choice has been made in order to neglect the presence of the sand ridge at the centerline. Right panels of the figures show the histograms of the distribution of the bed elevations, which allow a rough evaluation of the average height of the bedforms and, more importantly, an estimation of how often the rigid bottom of the flume is exposed by the bedform development. Figure 2.12 shows the two-dimensional spectra of the final bottom configurations for all the experiments of the first series. The results show that the peak harmonic component in the streamwise direction shifts towards lower frequencies as the thickness of the initial sand layer decreases confirming the lengthening of the starved dunes. The spectra of experiments S1N4 and S1N5 show that, in the transverse direction, the largest harmonic component is the second one, which represents the longitudinal sand ridge appearing along the axis of the channel. When looking at the results of Figure 2.12, the reader should realise that the length $L$ of the selected stretch where the Fourier decomposition is applied differs from experiment to experiment. By evaluating $L$ from Figure 2.11, it is important to note that the $10^{th}$ harmonic component of experiment S1N1 has approximately the same wavelength of the $8^{th}$ harmonic component of experiment S1N3.

The second series of experiments was carried out by increasing the flow discharge but keeping fixed all the other parameters and progressively decreasing the sediment supply. In this series, the rigid bottom was not exposed at the end of the experiments with $\Delta$ equal to $2.5$ and $2$ cm and the average wavelength of the dunes which shaped the alluvial bed was equal to about $0.50$ m. Experiment S2N3 was characterised by the same hydrodynamic parameters but $\Delta$ was equal to $1.5$ cm. The larger flow discharge of this series led to the baring of the rigid bottom even for such sand layer thickness and to the lengthening of the bedforms. In particular, a smaller number of bottom forms was observed at the end of this experiment and the average crest-to-crest distance was about $0.57$ m. This second series

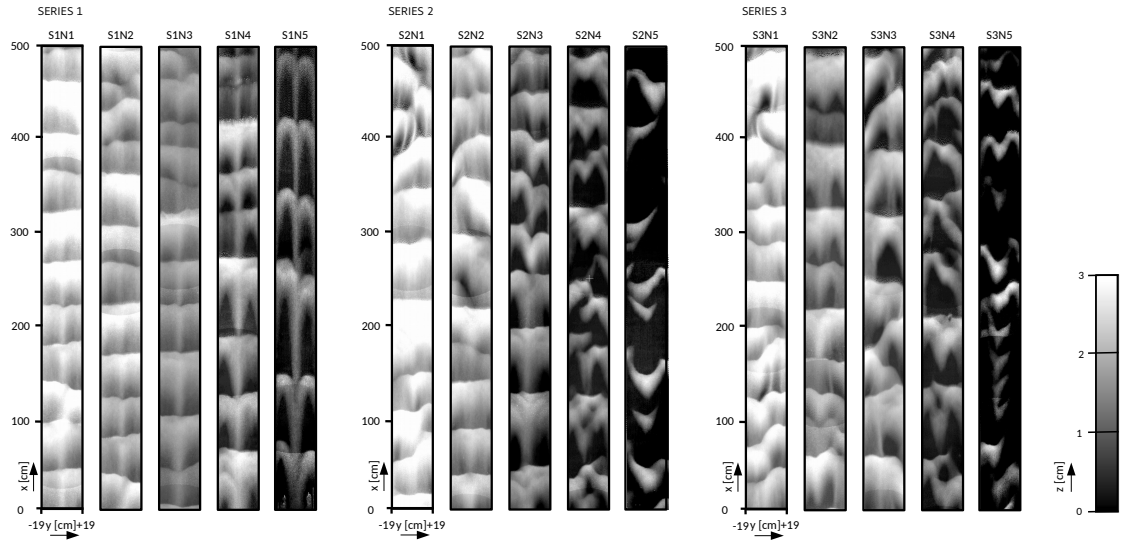


Figure 2.10: Laser scans representing the final bottom configuration within the $5$ m downstream stretch of the channel at the end of each experiment. Bottom elevation is shown in shades of grey, lighter colours corresponding to higher values. Rigid bottom level is black. Flow is from bottom to top.

of experiments includes two further experiments which were made with an initial uniform thickness of the sand layer equal to $1.0$ cm and $0.5$ cm, respectively. In the former case, $8$ bedforms were detected along the downstream part of the channel, while, in the latter, approximately $5$ bedforms were identified. The estimated wavelength of the dunes was about $0.68$ m and $1.12$ m, respectively. The central panel of Figure 2.10 shows the sequence of scans of a $5$ m long stretch of the channel for the different experiments of the second series. The data show also that, for the smallest value of the sand layer thickness $\Delta$, the bottom profile became quite irregular and barchan dunes appear. Figure 2.13 shows the bottom profile measured at the end of all the experiments of the second series along with the histograms of the distribution of the bed elevations. The results of the two-dimensional Fourier analysis are presented for the experiments of the second series in Figure 2.14. In line with the previous series of experiments, the results show that the peak harmonic component in the streamwise direction shifts towards lower frequencies as the initial volume of mobile sediment decreases. Furthermore, as the sediment starvation increases, the amplitude of the spanwise harmonic components becomes comparable with the amplitude of the streamwise components and, in some case, even larger. Indeed, the increased flow discharge of this series makes the resulting bottom configurations more three-dimensional. The regularly spaced transverse dunes progressively disappear, leading to barchan dunes, the transverse dimension of which is approximately equal to the channel width.

In the third series of experiments, the rigid bottom of the flume was not exposed by the formation of the dunes only for the largest value of the thickness $\Delta$ of the initial sand layer, which was equal to $2.5$ cm. As already pointed out, the bulk velocity in these experiments did not significantly differ from that of the second series because the increase of $Q$ was balanced by an increase of the water depth $H$. Hence, the final average wavelength of the dunes was slightly smaller than $0.50$ m, a value close to the wavelength of the alluvial bedforms observed

in the experiments of the second series. The rigid bottom was exposed at the end of all the other experiments of series $3$. Experiments S3N2, S3N3 and S3N4 show an increasing value of the mean crest-to-crest distance $\lambda$ which increased to $0.55$ m, to $0.60$ m and to about $0.73$ m, respectively. Experiment S3N5 was characterised by strongly limited supply conditions. The largest value of the flow discharge along with the smallest value of the initial thickness of the sand layer led to the appearance of markedly three-dimensional bottom forms. The high degree of irregularity, which characterised the observed bottom forms, made it difficult to estimate an average wavelength. The right panel of Figure 2.10 shows the sequence of scans of a $5$ m long stretch of the channel. Figures 2.15 and 2.16 show the bottom profile and the results of the two-dimensional Fourier analysis for all experiments of the third series. The results are similar to those of the previous series, even though a few qualitative differences are present. Indeed, for the smallest value of $\Delta$, amorphous three-dimensional bottom forms (sandy mounds) appear and the bedforms become more irregular in the streamwise direction. In fact the bottom panel of Figure 2.16 shows a wide spectrum both in the streamwise and spanwise directions. Figure 2.17, where the average streamwise wavelength of the dunes is plotted versus the initial sand layer thickness for each experiment, and Table 2.2 summarise the experimental results.

| Series | Exp. | $\Delta$ $[cm]$ | $Q$ $[ls^{-1}]$ | $h$ $[cm]$ | $\lambda$ $[cm]$ |
|---|---|---|---|---|---|
| 1 | $S1N1$ | 2.5 | 20 | 11 | 0.47 |
| | $S1N2$ | 2.0 | 20 | 11 | 0.47 |
| | $S1N3$ | 1.5 | 20 | 11 | 0.47 |
| | $S1N4$ | 1.0 | 20 | 11 | 0.65 |
| | $S1N5$ | 0.5 | 20 | 11 | 0.92 |
| 2 | $S2N1$ | 2.5 | 22.5 | 11 | 0.52 |
| | $S2N2$ | 2.0 | 22.5 | 11 | 0.53 |
| | $S2N3$ | 1.5 | 22.5 | 11 | 0.57 |
| | $S2N4$ | 1.0 | 22.5 | 11 | 0.68 |
| | $S2N5$ | 0.5 | 22.5 | 11 | 1.12 |
| 3 | $S3N1$ | 2.5 | 25 | 12 | 0.49 |
| | $S3N2$ | 2.0 | 25 | 12 | 0.55 |
| | $S3N3$ | 1.5 | 25 | 12 | 0.60 |
| | $S3N4$ | 1.0 | 25 | 12 | 0.73 |
| | $S3N5$ | 0.5 | 25 | 12 | 2.05 |

Table 2.2: Summary of the key variables measured at the end of each experiments.

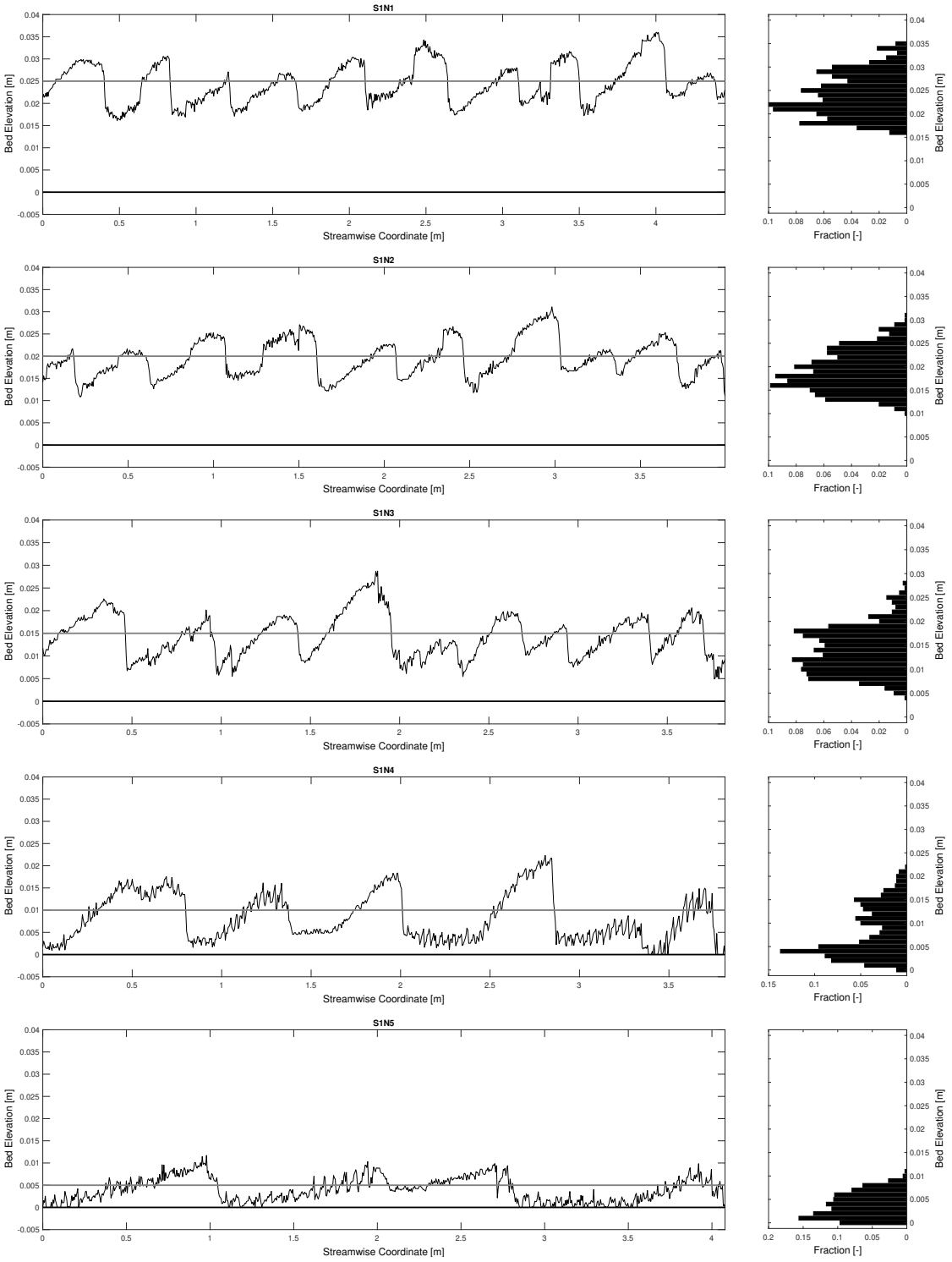


Figure 2.11: Left panels: bed elevation along a selected stretch of the channel (thin black line), for each experiment of Series 1. The rigid bottom of the flume is represented by the thick line while the initial level of the sand layer is represented by the thick grey line. Right panels: histogram of the distribution of the bed elevation. The label at the top of the panels indicate the experiment number listed in table 2.2.

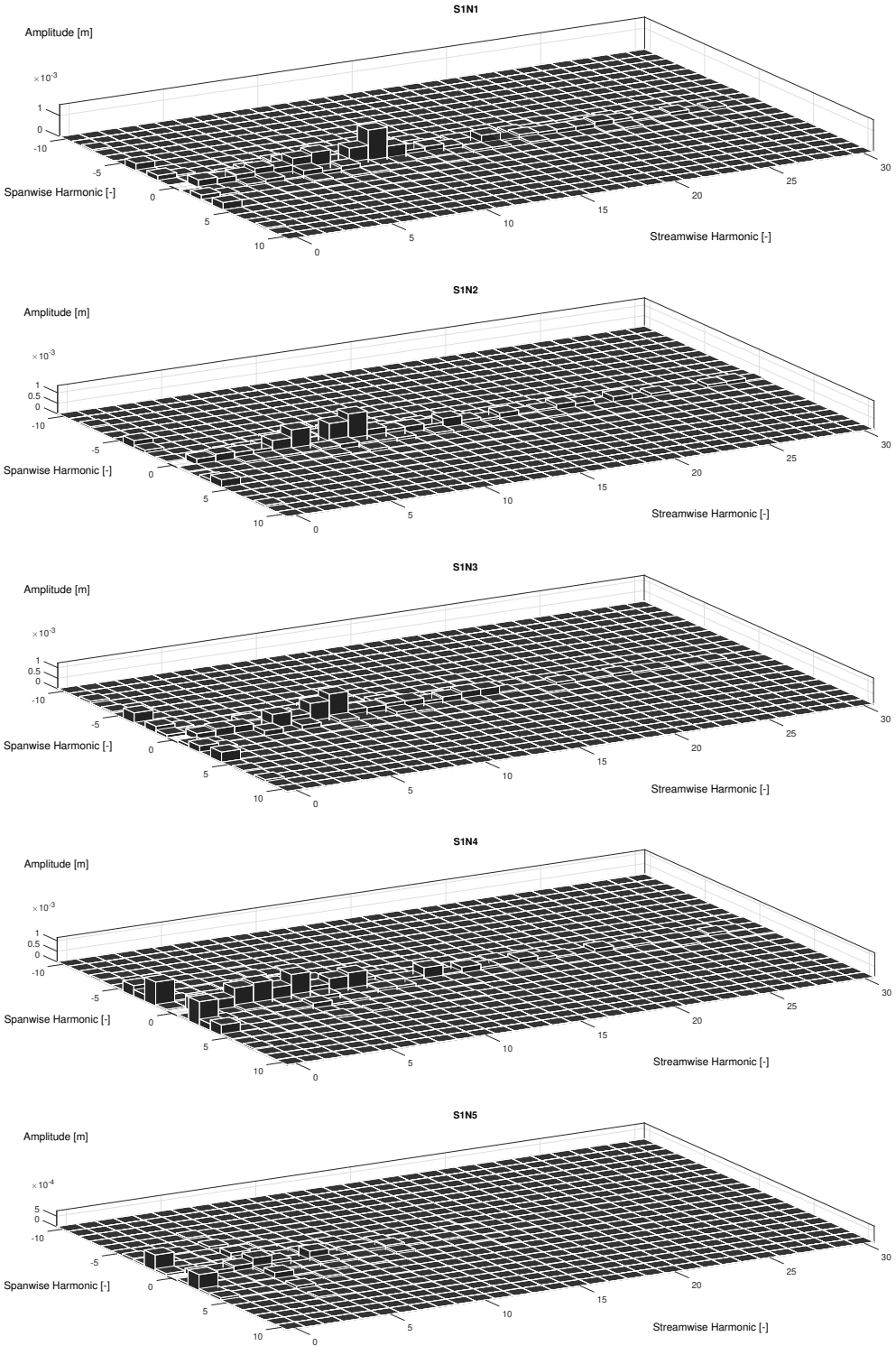


Figure 2.12: Results of the two-dimensional Fourier analysis of the bottom profile observed along the selected stretch at the end of each experiment of Series 1 (the reader should notice that, as pointed out in the text and shown in figure 2.11, the length of the selected stretches changes from experiment to experiment). The modulus of the Fourier components is plotted versus both the streamwise and the spanwise harmonics.

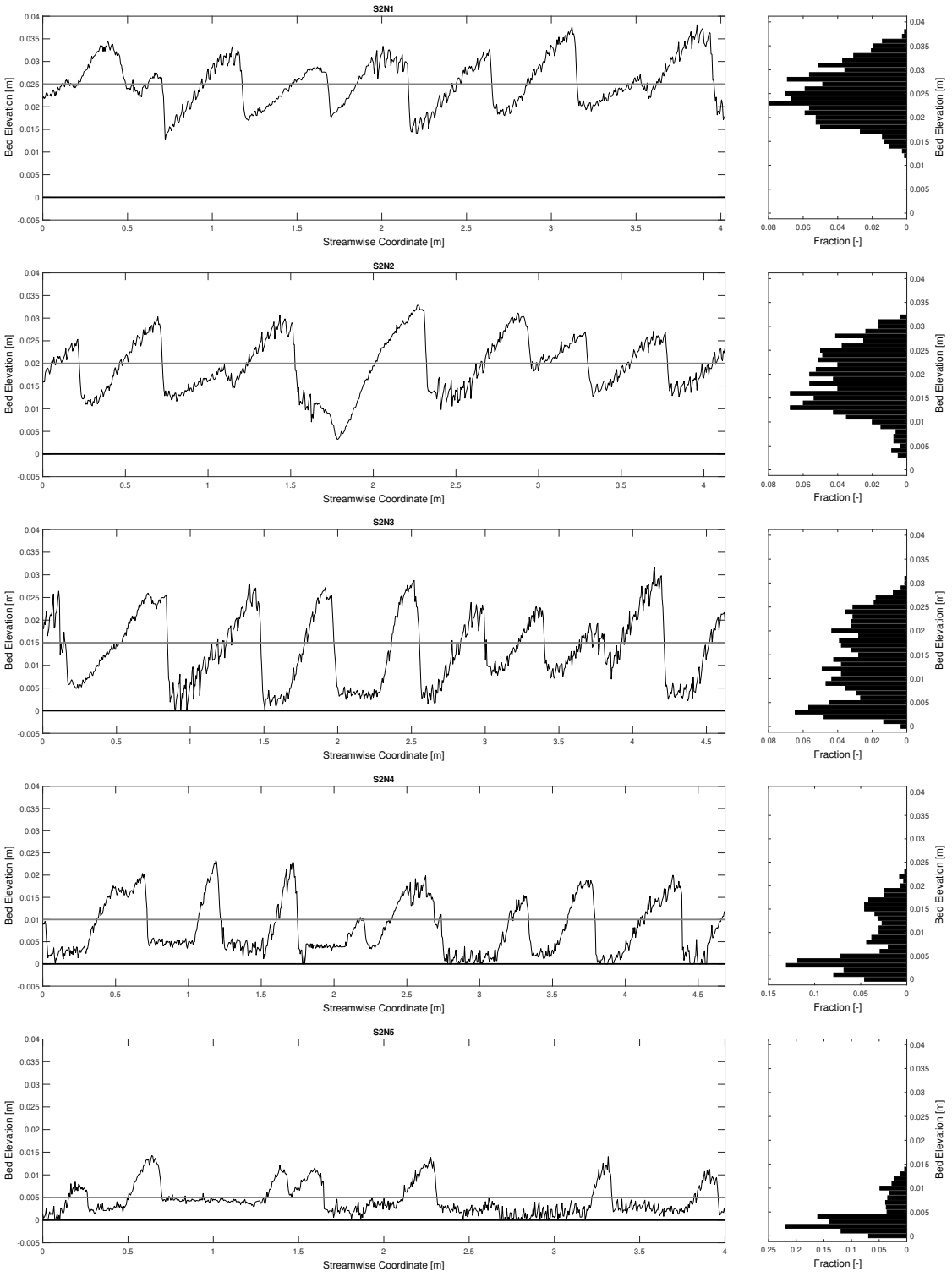


Figure 2.13: Left panels: bed elevation along a selected stretch of the channel (thin black line), for each experiment of Series 2. The rigid bottom of the flume is represented by the thick line while the initial level of the sand layer is represented by the thick grey line. Right panels: histogram of the distribution of the bed elevation. The label at the top of the panels indicate the experiment number listed in table 2.2.

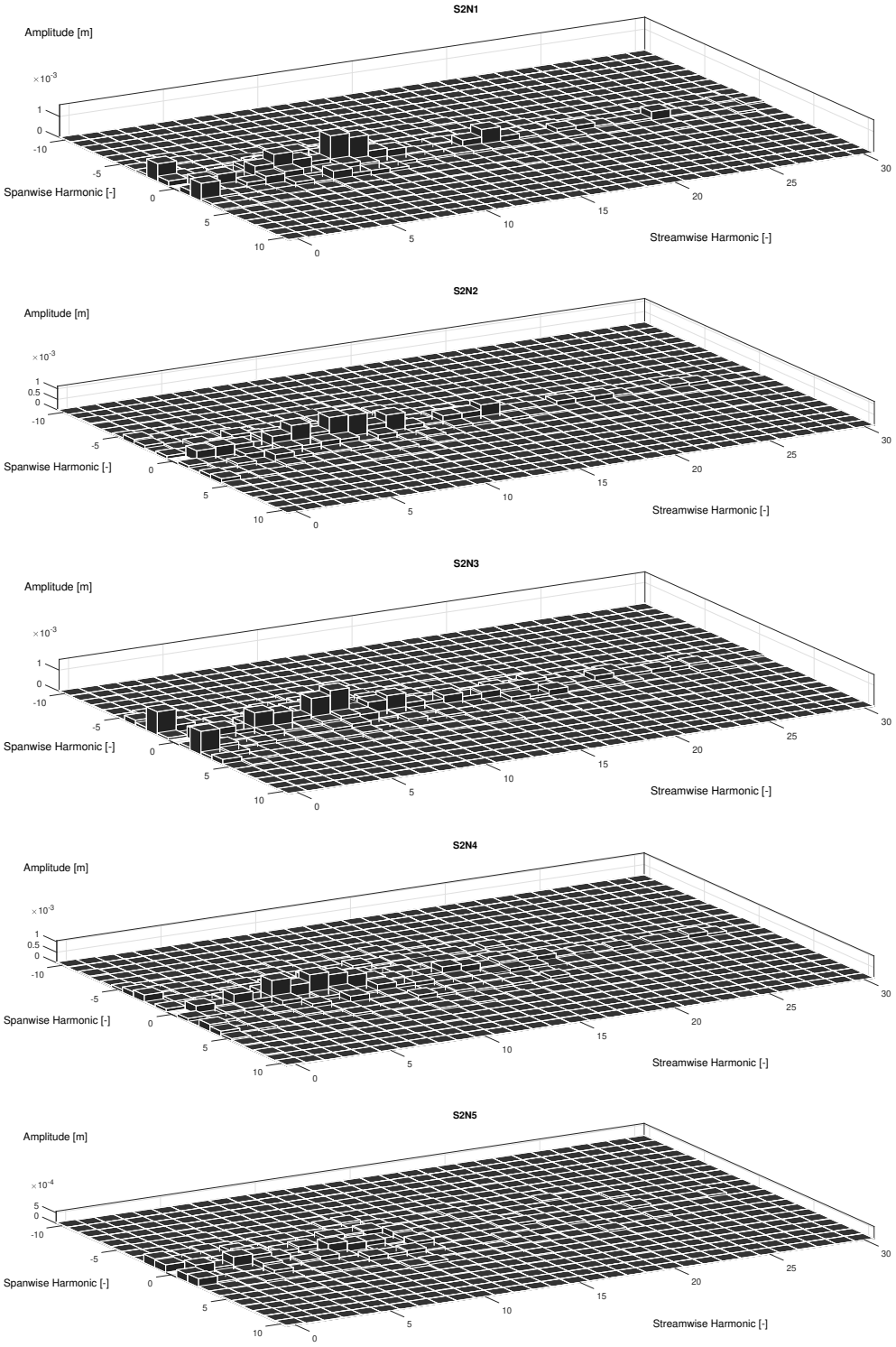


Figure 2.14: Results of the two-dimensional Fourier analysis of the bottom profile observed along the selected stretch at the end of each experiment of Series 2 (the reader should notice that, as pointed out in the text and shown in figure 2.13, the length of the selected stretches changes from experiment to experiment). The modulus of the Fourier components is plotted versus both the streamwise and the spanwise harmonics.

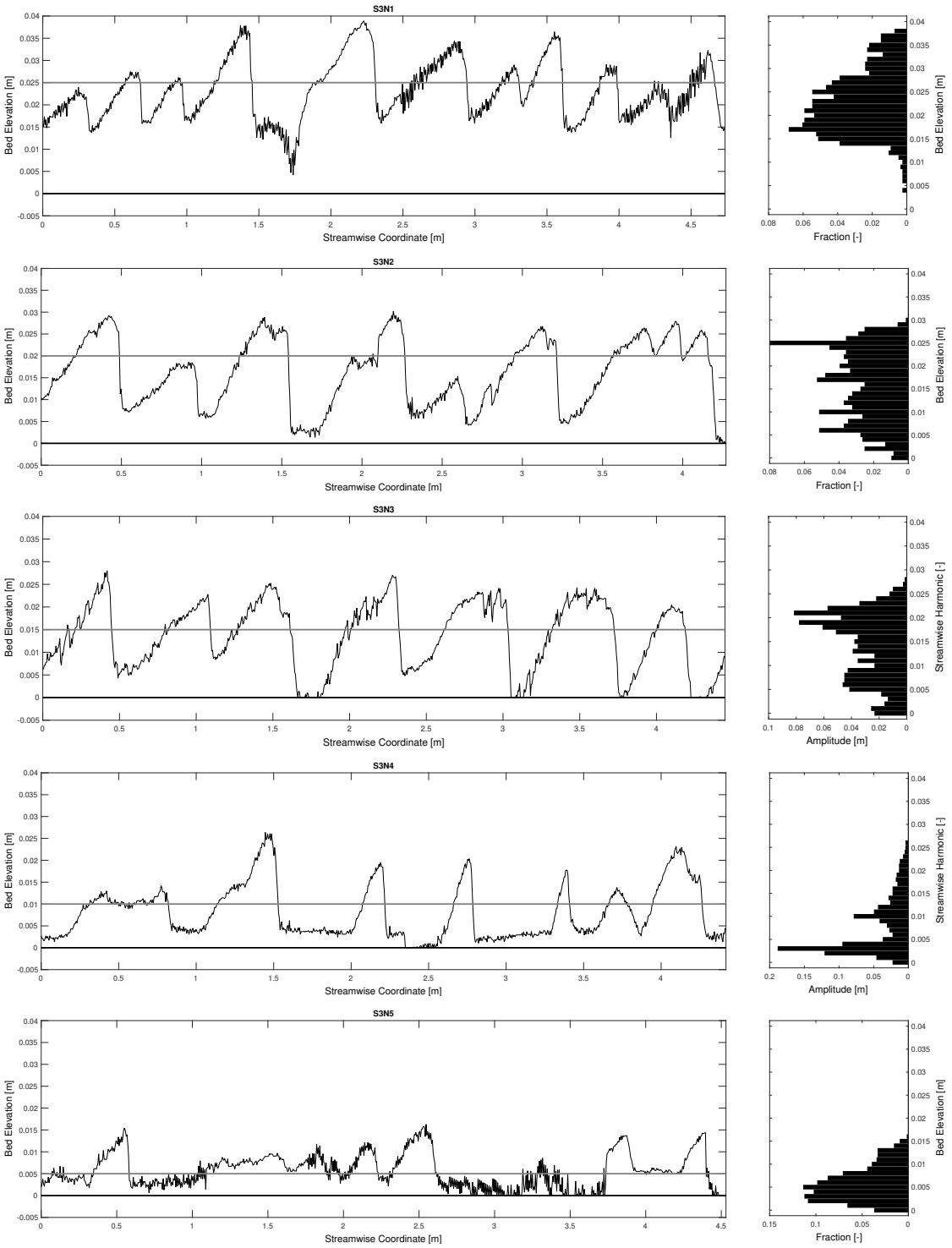


Figure 2.15: Left panels: bed elevation along a selected stretch of the channel (thin black line), for each experiment of Series 3. The rigid bottom of the flume is represented by the thick line while the initial level of the sand layer is represented by the thick grey line. Right panels: histogram of the distribution of the bed elevation. The label at the top of the panels indicate the experiment number listed in table 2.2.

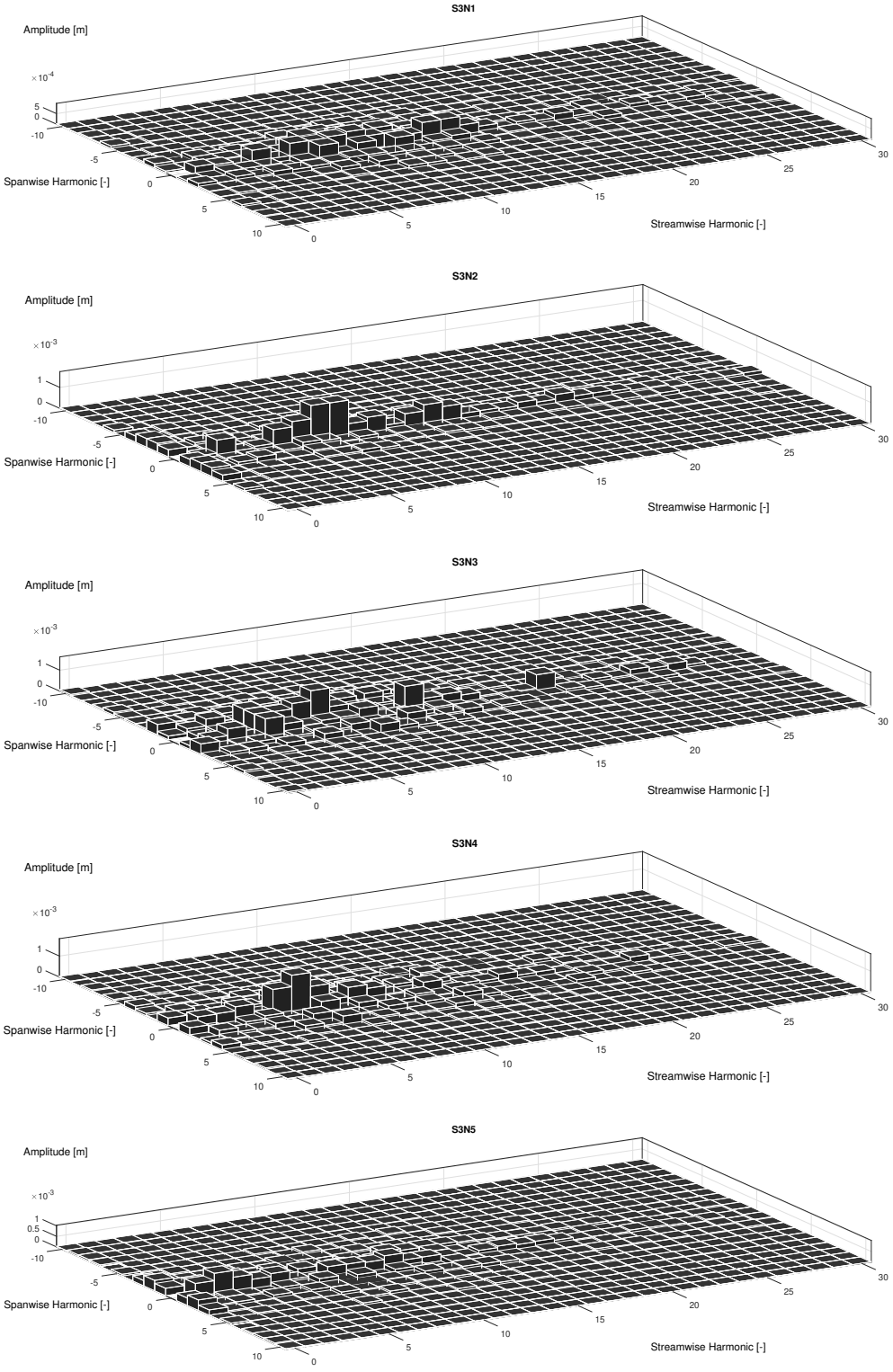


Figure 2.16: Results of the two-dimensional Fourier analysis of the bottom profile observed along the selected stretch at the end of each experiment of Series 3 (the reader should notice that, as pointed out in the text and shown in figure 2.15, the length of the selected stretches changes from experiment to experiment). The modulus of the Fourier components is plotted versus both the streamwise and the spanwise harmonics.

## 2.6 Discussions

The experimental measurements described in the previous section indicate that, when the rigid bottom of the flume is exposed by the formation of sand dunes, sediment starvation strongly affects the dune morphology. In particular, the average crest-to-crest distance of the dunes tends to increase as soon as the rigid bottom of the flume is exposed by their formation, the stronger the sediment starvation, the larger their average spacing. Furthermore, progressively decreasing the initial sand layer thickness, regularly spaced alluvial dunes are replaced by amorphous sandy mounds that are more irregularly spaced in the longitudinal direction. A further decrease of the initial sand layer thickness eventually results in the appearance of three-dimensional barchan dunes. These findings are in agreement with the field observations of Kleinhans et al. (2002) and Carling et al. (2000) and with those of Le Bot and Trentesaux (2004), even though the latter were carried out in a coastal region dominated by oscillatory tidal currents.

Kleinhans et al. (2002) described the observations and measurements of several type of bedforms in the gravel-bed river Allier (Moulis, France) over a period of low flow during which the river bed was fully armoured. Sand wave fields of fine sand ($d_s = 0.5$ mm), the area of which ranges from few squared metres to few hundreds of metres, were found to migrate over the armour layer ($85\%$ gravel, $d_s = 18$ mm) as a result of bank erosion and detachment of sand from meander pools. These sand waves provided a spatially varying supply of mobile sediment for the formation of bedforms in equal hydrodynamic conditions and sediment parameters. Regularly spaced transverse dunes appeared in the inner part of these sand deposits, where the thickness of the sand coverage attains its maximum value, and thus gradually changed in both the upstream and the downstream directions resulting into amorphous bedforms with more sinuous crests (Figure 2.18). At the front and rear edge of each sand wave field the armour layer was fully exposed and barchan dunes concurrently

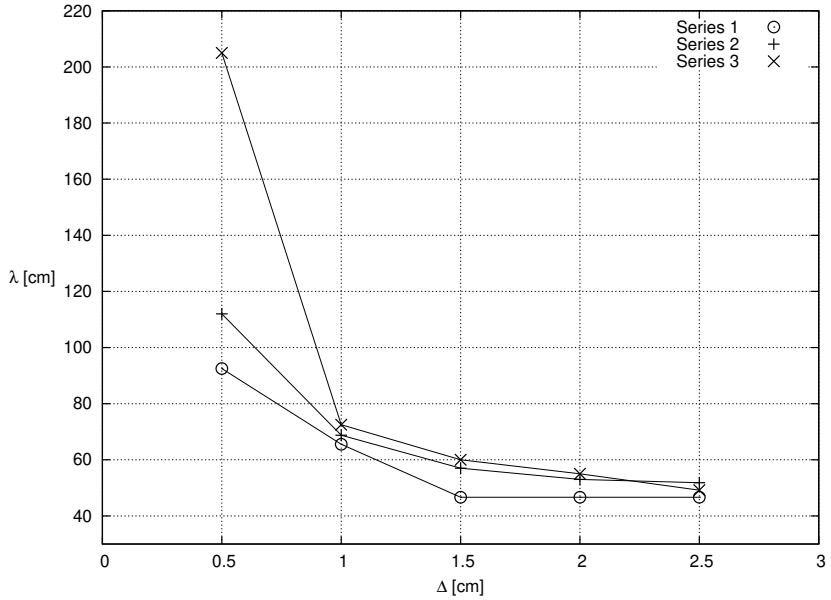


Figure 2.17: Wavelength $\lambda$ of the bottom forms plotted versus the thickness $\Delta$ of the sand layer initially present over the rigid bottom.

with sand ribbons were observed. Analogously to the laboratory measurements described in the previous section, the field observations of Kleinhans et al. (2002) suggest that the main factor in determining the geometric characteristics of the emerging bedforms is the thickness of the layer of sediment available for transport. The gradual transition from two-dimensional transverse dunes to strongly three-dimensional barchan dunes is the same as that observed through the present experimental investigation.

Carling et al. (2000) described the dynamics of sand dunes in a supply limited reach of the river Rhine (Mainz, Germany). Well sorted medium sand ($d_s = 0.9$ mm) was present in the form of different morphological patterns migrating over gravel lags mainly composed of pebbles and cobbles ($d_s = 10$ mm). Two distinct populations of dunes were identified: two-dimensional small dunes ($\lambda = 1 \div 5$ m) with relatively straight crest lines, which were roughly transverse to the primary flow direction, and three-dimensional large dunes ($\lambda = 20 \div 50$ m) with either amorphous or barchanoid planforms. Carling et al. (2000) described in detail two isolated dunes very different in terms of morphology and dimensions (Figure 2.19). During the observations, the river bed upstream and downstream of these isolated large dunes consisted of starved small dunes whose crest-to-crest distance was approximately $2$ m. When these small dunes were found to migrate over the stoss side of the parent isolated dunes, they decreased in length ($\lambda \sim 1$ m). These small dunes then attained an equilibrium geometry growing in dimensions ($\lambda \geq 1.5$ m) across the gentle stoss side of the parent isolated dunes up to their crestal regions, where the transition to upper-stage plane bed was observed. Furthermore, where the lee side angles of the isolated dunes were small, small dunes often reformed and they progressively increased in length moving downstream towards the intervening gravel lags. All that being said, these field observations seem to indicate that sediment starvation manifests itself by forming isolated barchan dunes as well as by affecting the dimensions of the small dunes. In particular, the lengthening of the small dunes as they migrate from the gentle lee side of isolated barchan dunes to the gravel lags is consistent with the lengthening of the starved dunes observed in the present experiments.

In contrast, the laboratory observations of Tuijnder et al. (2009) indicate that the sandy patterns interspersed with exposed parts of the rigid bottom of their flume are shorter than the alluvial ones that develop for similar values of the flow and sediment parameters (Figure 2.20). There are several possible explanations to this contradiction between laboratory experiments that present many similarities.

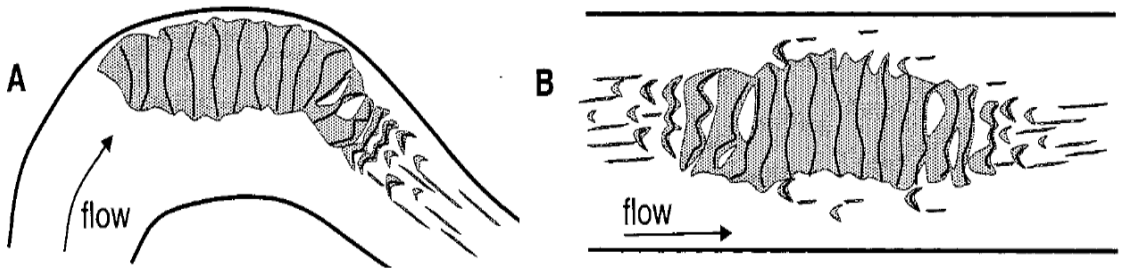


Figure 2.18: Observations of sand waves migrating over an immobile armour layer in the river Allier (Kleinhans et al., 2002). Panel A: Supply limited bottom forms emerging from a sand deposit in a meander pool. Panel B: Bottom forms in a migrating wave of sand. Crests are denoted by solid lines, sand is represented by stippled patches.

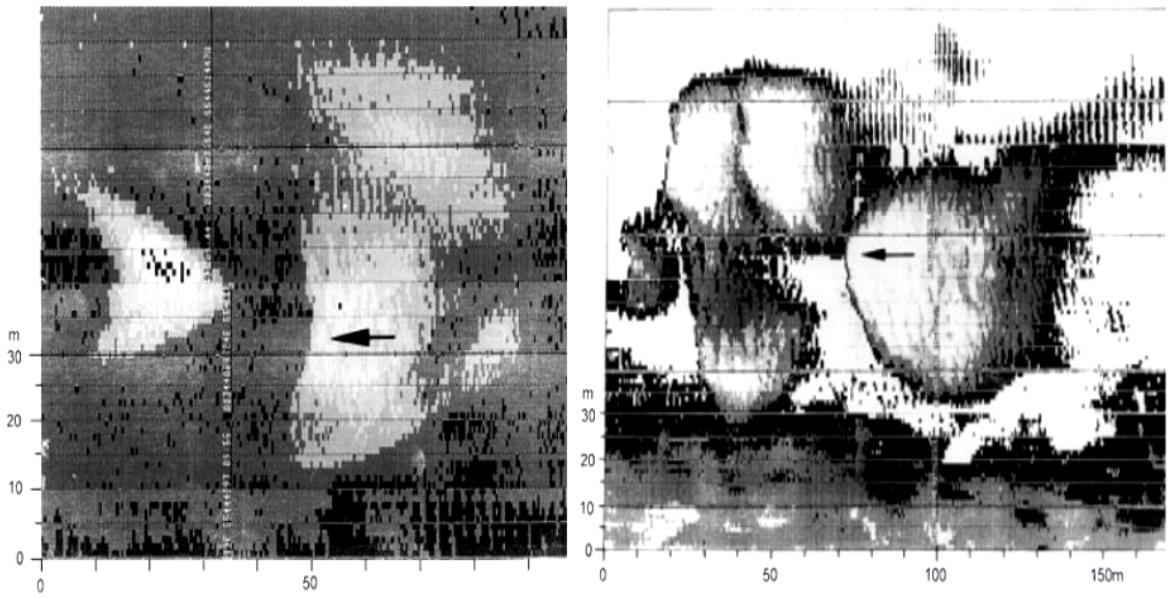


Figure 2.19: Plan views of the bed of River Rhine derived from acoustic reflection surveys (Carling et al., 2000). Arrows represents the direction of the river flows. Grey banding represents small dunes crossing the gravel lags (black areas). These dunes traverse onto the stoss of large isolated dunes, where they appear as light banding separated by grey portions. Tonal variations near the arrows represents secondary dunes of increasing length. Grey and black areas at the bottom of the figures represent gravels lags largely devoid of sand.

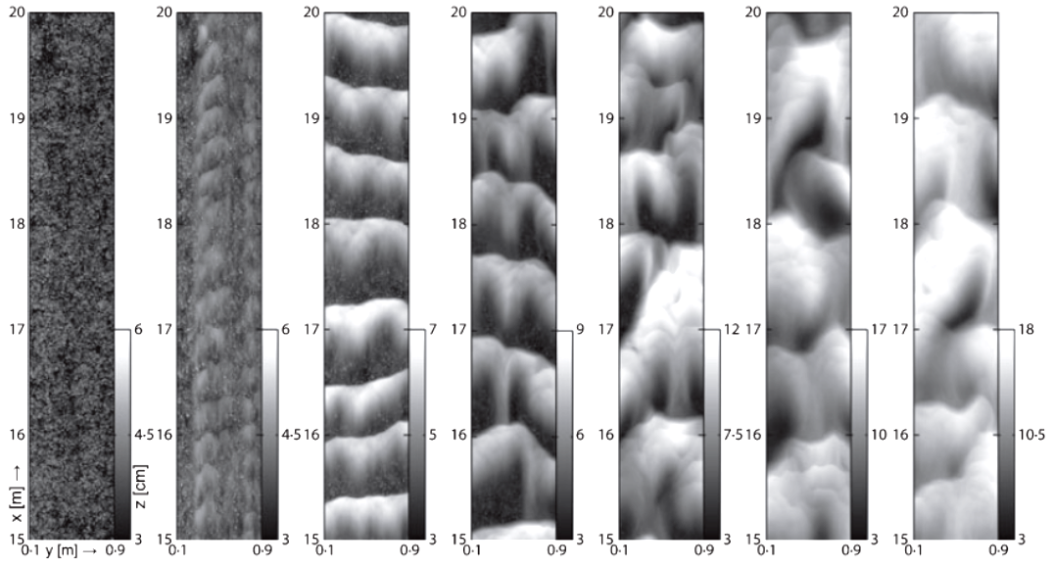


Figure 2.20: Laser surface scans from the experimental work by Tuijnder et al. (2009), situation after their experiments of Series 1. The level of grey indicates the height. The mean bed level is grey. Flow is from bottom to top.

Firstly, the duration of the experiments of Tuijnder et al. (2009) was remarkably different, depending on the amount of supply limitation. For strong supply-limited conditions, their experiments lasted for a few hours, whereas they were stopped after more than one day when the coarse layer was completely covered. It is likely that the size of the dunes increased in time reaching equilibrium wavelengths typically larger than those at the first stage of their formation. It is worth noting that alluvial dunes, which develop for extended periods of time, experience longitudinal elongation as a result of different physical mechanisms. These mechanisms have been extensively addressed by prior researches. At the very first stage of each experiment of the present investigation, small indentations, similar to those observed by Bagnold (1956), appear throughout the sandy bed and these patterns subsequently elongate as described by the laboratory observations of Coleman and Melville (1994). As discussed in Camporeale and Ridolfi (2011), this initial progressive elongation can be interpreted as a transient growth which can be predicted by a non-modal linear stability analysis, even neglecting nonlinear effects. All that being said, in the present study the formation of sand dunes was monitored during half an hour from the beginning of each experiment. The choice of fixing the same duration of the experiments for both the alluvial and the supply limited case was made to compare final bottom configurations obtained at the same stage of the evolution, thus highlighting the effect of supply limitation. A time interval of half an hour was set because the dunes, which were observed under both alluvial and supply limited conditions, can be readily identified and their further time development turned out to be relatively slow.

Secondly, two different grain sizes were employed in the experiments of Tuijnder et al. (2009): a coarser one for the substrate and a finer one for the mobile layer. The two sand diameters were chosen so as to be sure that the coarser fraction, when exposed to the flow, remained still. As a consequence, the more substrate was exposed, the higher the averaged bed roughness and the lower the averaged Shields stress, for the same Froude number. Although it is not clear how the bedform wavelength evolves due to a change of roughness, this effect can be so strong to reserve that of supply limitation. On the contrary, in the present experiments the substrate was made with the same sand, glued to the bottom of the flume. Once again, this was made purposely in order to enhance the effect of supply limitation alone.

Thirdly, the width of the flow cross-section in the experiments of Tuijnder et al. (2009) was more than twice that of the present experiments. Such a difference can strongly affect the emergence of bedforms at the bottom of laboratory steady streams. Colombini and Stocchino (2012), within the linear framework of sand dune formation, described the transition from transverse dunes to alternate bars owing to three-dimensional effects. In particular, as the width-to-depth ratio of the forcing flow increases, the most unstable mode predicted by their stability analysis and corresponding to transverse dunes is shown to loose stability towards three-dimensional configurations resulting into alternate bars, the longitudinal wavelength of which turns out to be much larger than those of typical sand dunes.

Finally, for the sake of clarity, it is worth specifying the nature of the leading mechanism for the appearance of the longitudinal sand ridges observed in most of the experiments. Secondary motions in the plane perpendicular to the main flow direction characterise turbulent flows in straight channels having turbulence as driving mechanism. These turbulence driven motions are induced by an imbalance of the normal Reynolds stresses in the cross-sectional plane that, in channels with rectangular cross-sections, is caused by the presence of the sidewalls and the corners they form with the bottom and the free surface. As a result, turbulent open channel flows host naturally an integer number of corner vortices extended from each

side of the walls to the centerline of the channel, the preferential locations of which are imposed by the aspect ratio (AR) between the channel span and the mean water depth. Sakai and Uhlmann (2016) performed direct numerical simulations of open channel flows with rectangular cross-sections describing different secondary motions depending on the aspect ratio (AR) and the flow Reynolds number (Re). Figure 2.21 shows the streamlines for a geometrical configuration similar to the present experiments and a fully developed turbulent flow. When the bottom of the channel is covered by an uniform sandy bed, it is likely that the weak transverse flow produces a continuous sediment transport that leads to the formation of longitudinal sand ridges along the channel axis (Nezu and Nakagawa, 1984).

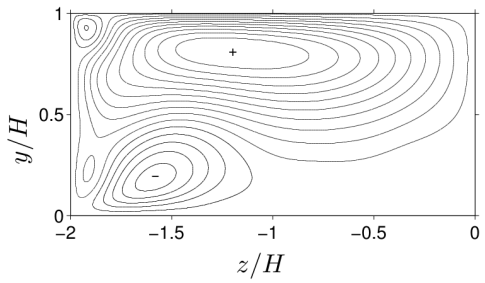


Figure 2.21: Streamlines of an open duct flow with AR=4 and Re=5000 in the left-half cross-section. Minus sign corresponds to counter-clockwise motion (Sakai and Uhlmann, 2016).

## 2.7 Conclusions

Laboratory experiments were carefully designed to investigate the formation of starved dunes in steady currents in order to focus only on the role played by sediment starvation neglecting effects due to sediment sorting, three-dimensionality and amplitude time-development. The main outcome of the experimental investigation are the following.

- Laboratory measurements of the bottom profile of both alluvial dunes and starved dunes, for the same values of the hydrodynamic and morphodynamic parameters and, in particular, for the same duration of the experiments, show that starved dunes attained longer wavelengths than alluvial dunes. This is consistent with previous field observations.
- When strong sediment starvation is enforced, three-dimensional bedforms characterised by a high irregularity appear, making it difficult to identify a well defined wavelength of the patterns. As the sediment starvation increases, alluvial two-dimensional dunes are replaced by more irregular starved dunes that then disperse in the form of amorphous sandy mounds eventually leading to the emergence of three-dimensional barchan dunes.

# Chapter 3

# A Numerical Investigation on the Formation of Starved Dunes in Steady Currents


## Abstract

The formation of fluvial dunes is a non-trivial problem which has been thoroughly investigated by prior researches using theoretical and physical models that assume an infinite availability of mobile sediments. Field observations and laboratory experiments nevertheless indicate that the volume of sediment available for transport affects the formation of sand dunes. The present investigation is intended to be a contribution to the stability theory of sand dunes in steady currents that accounts for the effect of sediment starvation on the formation of fluvial dunes. An idealised process-based model is presented which consists of a hydrodynamic module, that is based on a perturbation approach and considers a steady turbulent free-surface flow interacting with small amplitude undulations of a sandy bottom, and a morphodynamic module, that is based on a numerical integration of the sediment continuity equation and accounts for the possibility of the exposition of a motionless substratum. The main outcome of the theoretical investigation is that, when the motionless substratum is exposed by the formation of the dunes, the lack of sand affect the sediment transport and, in turn, the dune morphology. As the motionless substratum is progressively exposed by the growth of the dunes, numerical results predict the lengthening of the starved bedforms and an increasing irregularity in their spacing. The reliability of the idealised model is supported by comparisons of the theoretical findings with both field observations and the laboratory measurements described in the preceding chapter.

## 3.1 Introduction

As described in 1.1, river beds are seldom flat and those that contain sand generally exhibit a fascinating variety of bedforms, ranging from small scale ripples to large scale dunes. Whenever the bed shear stress is larger than its threshold value for sediment motion, sediment particles begin to move and, in response to this movement, sediment patterns might appear. On the one hand, flow and sediment transport produce sandy patterns, on the other hand, sandy pattern appearance profoundly influences flow and sediment transport. These bedforms have crests that are perpendicular to the main direction of the fluvial stream and, as such, their presence is a primary source of flow roughness and therefore a major factor in determining water levels. As a consequence, unravelling the processes underlying their appearance is a subject of great concern to river engineering. Fluvial ripples develop when viscosity affects the vertical velocity profile of the fluvial stream in the near-bed region (hydraulically smooth and transitional flows) and, in turn, the bed shear stress and the related sediment transport, inducing a particular bed wave instability that ultimately leads to the appearance of the aforementioned bedforms. These small-scale patterns exhibit asymmetric profiles with fairly regular crests that migrate invariably downstream and their formation is characteristic of subcritical flows in the Reynolds sense: they are likely to emerge when the grain Reynolds number is lower than a certain critical value (Sumer and Bakioglu, 1984). Ripples play an important role in sediment transport and mixing processes at the river bed as flow separation occurs at their crests eventually inducing coherent flow structures (vortices) that locally affect mass and momentum transfer. For practical purposes, the effect that these small-scale bedforms have on large-scale phenomena can be modelled by assimilating their presence as a hydraulic roughness of appropriate size. Differently, fluvial dunes develop where coarser sediment disrupts the viscous sub-layer (hydraulically rough flows) and, as a result, their formation differs substantially from that of ripples (Colombini and Stocchino, 2011), although they exhibit many comparable characteristics. The typical crest-to-crest distance of fluvial dunes scales with the flow depth and they are characteristic of subcritical flows in the Froude sense. Antidunes are a distinct class of bedforms, which scale with the flow depth and emerge from sediment mixtures forced by supercritical streams and, unlike dunes, may migrate either upstream or downstream. Because of their significance in formulating depth-discharge relations for river flows and predictor formulae for sediment transport, bedforms in general, and dunes in particular, received extensive attention from engineers and geomorphologists.

As pointed out in 2.1, in many natural environments, the morphological patterns which are commonly observed where large amounts of mobile sediment are available (i.e. alluvial bedforms) differ from those which form where the mobile sediment is insufficient to cover an underlying body of sediment which can not be moved by the flowing fluid (i.e. starved bedforms). In fluvial environments sediment starvation is common. As channel slopes decrease, rivers typically exhibit abrupt transitions from gravel to sandy bottoms. In many cases, seasonal and perennial streams subject to periods of low flow or discharge waves undergo a transient degradation until they are fully armoured (Parker et al., 1982). Then the natural formation of such a motionless substratum inhibits the entrainment of finer sediment from the bed, eventually resulting in sediment starvation. Whereby the armoured bed is developed and finer material continues to be supplied to the river stream, starved dunes are observed but how sediment starvation affects their morphology is still unclear. Carling et al. (2000) describe the dynamics of fluvial dunes migrating over a gravel lag layer within a sediment

starved reach of the Rhine river (Germany). Their data show the existence of two distinct population of dunes, two-dimensional small-scale transverse dunes with lengths of several meters and three-dimensional large-scale amorphous dunes with lengths of several tens of meters. Their data suggest that sediment starvation manifested itself by giving rise to these isolated, amorphous sandy dunes interspersed with plane gravel lags. The data also indicate that the crest-to-crest distance of the small dunes changes as they move from the immobile gravel lags to the stoss and lee sides of the large dunes where mobile sediment is largely available. In particular, the wavelength of the small dunes is longer when they move above the gravel lag layer.

The formation of fluvial dunes is a non-trivial problem which has been investigated in great details by prior researches. A first theoretical approach to the study of sand dune formation was proposed by Kennedy (1969), who's contribution proved that fluvial dunes can be interpreted as a free instability of perturbed alluvial beds forced by uniform steady flows. Later, Engelund (1970), described dune instability as a result of the balance between the stabilising effects of gravity and the destabilising effects of friction leading to a phase shift between the bottom perturbation and the perturbation of the shear stress which drives the instability process. By using suitable flow models and the sediment continuity equation, progresses were made in the modelling of the formation of fluvial dunes within the framework of linear stability encompassing various lines of research (Richards, 1980). An extensive review of the linear theory of fluvial dune formation can be found in Colombini (2004), who revisited it by overcoming some deficiencies in the state-of-the-art modelling through the use of a more refined description of both hydrodynamics and sediment transport.

All these theoretical investigations consider an infinite availability of mobile sediment and, as such, if the availability of the mobile sediment is limited they are not valid. Blondeaux et al. (2016) performed numerical and experimental investigations on the effects of sediment starvation on the formation of sea-wave-ripples. They investigated the formation of ripples in oscillatory currents by means of an idealised process-based model that accounts for the effects of sediment starvation. The present investigation is intended to be an extension of the linear stability analysis by Colombini (2004) which comprises the effect of sediment starvation on the formation of fluvial dunes. The main hypothesis of this study is that when a motionless substratum is exposed by the formation of dunes, the lack of sand affects the sediment transport, and, in turn, the dune morphology. By following the numerical approach outlined in Blondeaux et al. (2016), this hypothesis is formulated through numerical means.

The next section is devoted to the description of the linear stability analysis of the formation of alluvial dunes in steady currents and its analytic results are discussed in Section **??**. A numerical model of the formation of starved dunes in steady currents is subsequently presented in Section 3.4 and its numerical results are presented in Section 3.5. Numerical results which comprises the effect of sediment starvation are compared with the analytic results of the standard stability analysis of alluvial dunes. Furthermore, theoretical findings are compared with both field observations and laboratory measurements. The conclusions are drawn in the final section.

## 3.2 Linear stability analysis

### 3.2.1 Hydrodynamic model

Let us consider the motion of water as that of a viscous incompressible fluid flowing due to gravity through a domain bounded by a bed interface and a free surface. Since seasonal and perennial rivers are characterised by high fluid speeds and large spatial scales, the flow of water in fluvial streams is turbulent; hence the involved hydrodynamics can be described by the Reynolds-Averaged-Navier-Stokes equations which read

$$\frac{\partial v_i^*}{\partial x_i^*} = 0 \,, \tag{3.1}$$

$$\rho^* \frac{Dv_i^*}{Dt^*} = \rho^* \left( \frac{\partial v_i^*}{\partial t^*} + v_j^* \frac{\partial v_i^*}{\partial x_j^*} \right) = -\frac{\partial p^*}{\partial x_i^*} - \rho^* g^* \widehat{z}_i^* + \mu^* \frac{\partial^2 v_i^*}{\partial x_l^* \partial x_l^*} - \rho^* \frac{\partial \overline{v_i'^* v_l'^*}}{\partial x_l^*} \,, \tag{3.2}$$

where $x_i^*$ denotes the generic coordinate of a three-dimensional Cartesian frame of reference, $v_i^*$ represents the ensemble averaged fluid velocity component along $x_i^*$, while $v_i'^*$ is the random velocity fluctuation along the same coordinate and $p^*$ is the pressure (an asterisk denotes dimensional quantities). The density of water $\rho^*$ and its dynamic viscosity $\mu^*$ are assumed to be constant in space and time. Finally $g^*$ is the gravitational acceleration and $\widehat{z}_i^*$ is the component along $x_i^*$ of the vertical unit vector $\widehat{z}^*$, which is pointing upwards.

Because of the nonlinearity of convective terms of the governing equations, Reynolds stresses arise accounting for the turbulent diffusion of momentum. Once the dynamic turbulent eddy viscosity $\mu_T^*$ is introduced, it is possible to model the Reynolds stresses by a Boussinesq type closure, neglecting the viscous stresses ($\mu_T^* \gg \mu^*$)

$$T_{il}^* = -\rho^* \overline{v_i'^* v_l'^*} = \mu_T^* \left( \frac{\partial v_i^*}{\partial x_l^*} + \frac{\partial v_l^*}{\partial x_i^*} \right) - \rho^* \frac{2}{3} K^* \delta_{il} \quad , \quad K^* = \frac{\overline{v_l'^* v_l'^*}}{2} \,. \tag{3.3}$$

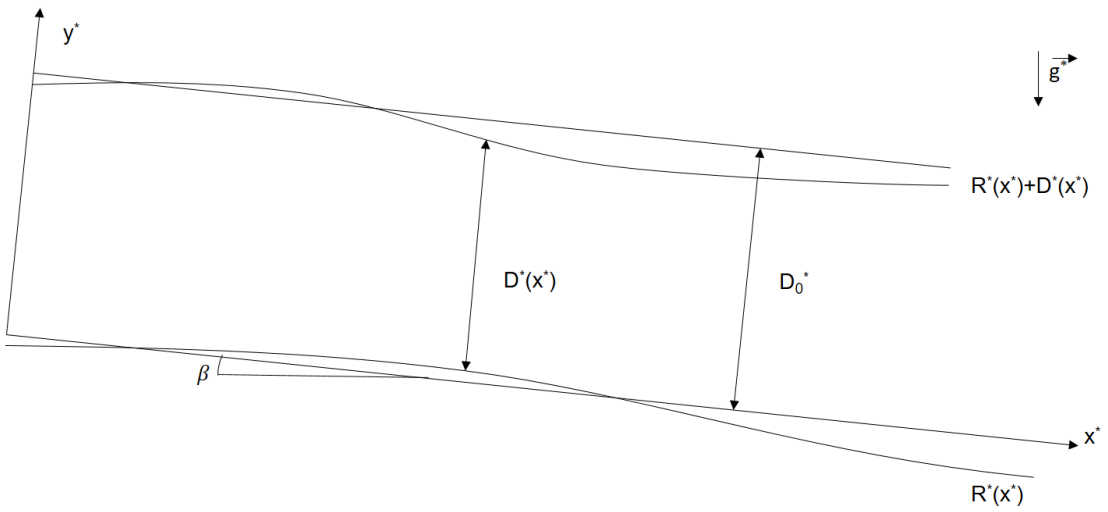


Figure 3.1: Sketch of the problem.

Since the objective of the present analysis is the investigation of the formation of fluvial dunes under simple hydrodynamic conditions, a steady flow in a wide straight channel with uniform slope $S$ ($\equiv tan(\beta)$) is considered. As fluvial dunes usually show crests almost perpendicular to the main flow direction, the steady turbulent free-surface flow is studied in a two-dimensional frame of reference $(x^*, y^*)$ with the $x^*$-axis along the channel axis and the $y^*$-axis pointing upwards with the origin at the average bottom (see Figure 3.1). The free surface is represented by the curve $y^* = R^* + D^*$, where $D^*$ is the local value of the stream depth, while the interface between the sandy bottom and the fluid flow is set at the reference level, i.e. the average level at which conventionally the mean logarithmic velocity profile vanishes, which is related to the bottom roughness. Considering small values of the uniform channel slope ($cos(\beta) \simeq 1$) along with an appropriate modified pressure $p^* = P^* - \rho^* \frac{2}{3} K^*$, the hydrodynamic model reads

$$\frac{\partial U^*}{\partial x^*} + \frac{\partial V^*}{\partial y^*} = 0 \tag{3.4}$$

$$U^* \frac{\partial U^*}{\partial x^*} + V^* \frac{\partial U^*}{\partial y^*} = -\frac{1}{\rho^*} \frac{\partial P^*}{\partial x^*} + g^* S + \frac{1}{\rho^*} \left( \frac{\partial T^*_{xx}}{\partial x^*} + \frac{\partial T^*_{xy}}{\partial y^*} \right) \tag{3.5}$$

$$U^* \frac{\partial V^*}{\partial x^*} + V^* \frac{\partial V^*}{\partial y^*} = -\frac{1}{\rho^*} \frac{\partial P^*}{\partial y^*} - g^* + \frac{1}{\rho^*} \left( \frac{\partial T^*_{yx}}{\partial x^*} + \frac{\partial T^*_{yy}}{\partial y^*} \right) \tag{3.6}$$

where $T^*_{ij}$ are the components of the Reynolds stress tensor

$$\mathbf{T}^* = \begin{bmatrix} T^*_{xx} & T^*_{xy} \\ T^*_{yx} & T^*_{yy} \end{bmatrix} = \begin{bmatrix} 2\mu^*_T \frac{\partial U^*}{\partial x^*} & \mu^*_T \left( \frac{\partial U^*}{\partial y^*} + \frac{\partial V^*}{\partial x^*} \right) \\ \mu^*_T \left( \frac{\partial U^*}{\partial y^*} + \frac{\partial V^*}{\partial x^*} \right) & 2\mu^*_T \frac{\partial V^*}{\partial y^*} \end{bmatrix} . \tag{3.7}$$

A self-similar solution for the turbulent kinematic eddy viscosity is assumed

$$\nu^*_T = \frac{\mu^*_T}{\rho^*} = L^2(y^*) \frac{\partial U^*}{\partial y^*} . \tag{3.8}$$

The problem is then closed by appropriate boundary conditions. Laboratory measurements show that the vanishing of the flow velocity should be forced at $y^* = R^* = k^*_s/30 \simeq 2.5 d^*_s/30$, where $k^*_s$ is the equivalent roughness length which is proportional to the mean grain size $d^*_s$

$$U^* = 0 \ , \quad V^* = 0 \quad \text{at} \ \ y^* = R^* . \tag{3.9}$$

Accounting for the free surface equation $F^* = y^* - (R^* + D^*) = 0$, the kinematic boundary condition is imposed at the free surface

$$\frac{DF^*}{Dt^*} = -U^* \left( \frac{\partial R^*}{\partial x^*} + \frac{\partial D^*}{\partial x^*} \right) + V^* = 0 \quad \text{at} \ \ y^* = R^* + D^* . \tag{3.10}$$

Introducing the unit vector normal to the free surface $\bar{n} \equiv \nabla^* F^* / |\nabla^* F^*|$, the dynamic boundary conditions can be expressed which force the vanishing of both normal $t^*_N$ and tangential $t^*_T$ stresses to the free surface

$$t^*_N = \bar{n} \cdot \mathbf{T}^* \cdot \bar{n} = -2 \left( \frac{\partial R^*}{\partial x^*} + \frac{\partial D^*}{\partial x^*} \right) \mu^*_T \left( \frac{\partial U^*}{\partial y^*} + \frac{\partial V^*}{\partial x^*} \right) - P^* + 2\mu^*_T \frac{\partial V^*}{\partial y^*} = 0 , \tag{3.11}$$

$$t^*_T = |\bar{t}^* - t^*_N \bar{n}| = \mu^*_T \left( \frac{\partial U^*}{\partial y^*} + \frac{\partial V^*}{\partial x^*} \right) = 0 \quad \text{at} \ \ y^* = R^* + D^* . \tag{3.12}$$

The problem is formulated in dimensionless form by introducing the following dimensionless variables

$$(x,y)=\frac{(x^*,y^*)}{D_0^*}\ ,\ \ (R,D)=\frac{(R^*,D^*)}{D_0^*}\ ,\ \ (U,V)=\frac{(U^*,V^*)}{u_{\tau 0}^*}\ ,\ \ P=\frac{P^*}{\rho^* u_{\tau 0}^{*2}}\ . \tag{3.13}$$

The mean water depth $D_0^*$ is chosen as length scale for both horizontal and vertical coordinates because the model has to be applied to study the formation of sand dunes which usually are found to scale with the mean water depth. The mean shear velocity $u_{\tau 0}^*$ is chosen as scale of flow velocity. Since a rough steady flow in a wide straight channel is being considered, the mean shear velocity can be related to the averaged flow velocity $\bar{U_0^*}$ and the mean water depth $D_0^*$ by the Chezy relationship

$$u_{\tau 0}^*=\frac{U_0^*}{\mathcal{C}}\simeq\sqrt{g^* D_0^* S}\ \ \Rightarrow \mathcal{C}=\frac{U_0^*}{u_{\tau 0}^*}\simeq\frac{F_R}{\sqrt{S}}\ , \tag{3.14}$$

where $\mathcal{C}$ is the conductance coefficient, $F_R=U_0^*/\sqrt{gD_0^*}$ is the characteristic Froude number of the flow, i.e., the ratio of the flow inertia to the external gravitational field, and $S$ is the mean longitudinal slope of the channel.

The dimensionless Reynolds-Averaged-Navier-Stokes equations read

$$\frac{\partial U}{\partial x}+\frac{\partial V}{\partial y}=0\ , \tag{3.15}$$

$$U\frac{\partial U}{\partial x}+V\frac{\partial U}{\partial y}=-\frac{\partial P}{\partial x}+1+\frac{\partial T_{xx}}{\partial x}+\frac{\partial T_{xy}}{\partial y}\ , \tag{3.16}$$

$$\frac{\partial P}{\partial y}=-\frac{1}{S}\ , \tag{3.17}$$

where $T_{ij}$ are the dimensionless Reynolds stresses

$$\mathbf{T}=\begin{bmatrix}T_{xx} & T_{xy}\\ T_{yx} & T_{yy}\end{bmatrix}=\begin{bmatrix}2\nu_T\frac{\partial U}{\partial x} & \nu_T\left(\frac{\partial U}{\partial y}+\frac{\partial V}{\partial x}\right)\\ \nu_T\left(\frac{\partial U}{\partial y}+\frac{\partial V}{\partial x}\right) & 2\nu_T\frac{\partial V}{\partial y}\end{bmatrix}\ , \tag{3.18}$$

and $\nu_T$ is the dimensionless turbulent eddy viscosity

$$\nu_T=\frac{\nu_T^*(x^*,y^*)}{D_0^* u_{\tau 0}^*}=\frac{[D^*(x^*)L(y^*)]^2}{(D_0^* u_{\tau 0}^*)}\frac{\partial U^*}{\partial y^*}\frac{D_0^*}{D_0^*}=[D(x)L(y)]^2\frac{\partial U}{\partial y}\ . \tag{3.19}$$

The dimensionless boundary conditions read

$$U=0\ \ ,\ \ V=0\ \ \text{at}\ \ y=R(x)\ , \tag{3.20}$$

$$-U\left(\frac{\partial R}{\partial x}+\frac{\partial D}{\partial x}\right)+V=0\ \ \text{at}\ \ y=R(x)+D(x)\ , \tag{3.21}$$

$$t_N=-2\left(\frac{\partial R}{\partial x}+\frac{\partial D}{\partial x}\right)\nu_T\left(\frac{\partial U}{\partial y}+\frac{\partial V}{\partial x}\right)-P+2\nu_T\frac{\partial V}{\partial y}=0\ \ \text{at}\ \ y=R(x)+D(x)\ , \tag{3.22}$$

$$t_T=\nu_T\left(\frac{\partial U}{\partial y}+\frac{\partial V}{\partial x}\right)=0\ \ \text{at}\ \ y=R(x)+D(x)\ . \tag{3.23}$$

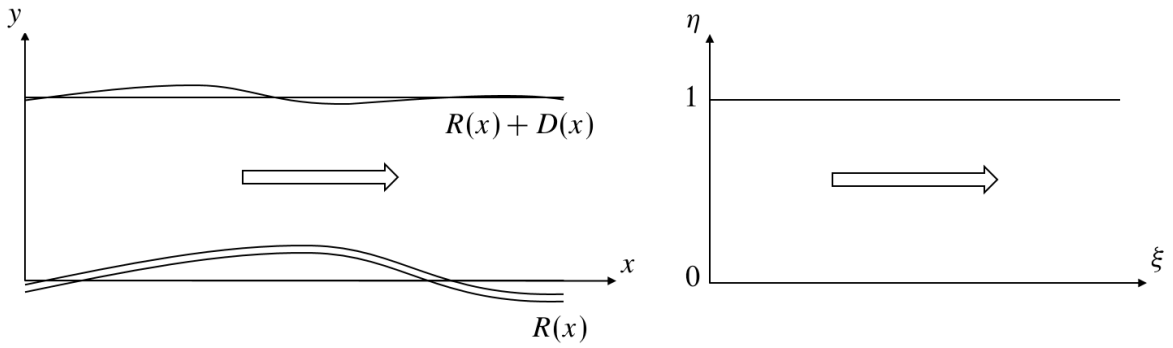


Figure 3.2: Sketch of the coordinate transformation.

Presently the problem is solved by introducing the following coordinate transformation

$$\begin{cases} \xi = x \\ \eta = \frac{y - R(x)}{D(x)} \end{cases} \tag{3.24}$$

such that the flow domain $y \in [R(x,t), R(x,t) + D(x,t)]$ is transformed into $\eta \in [0,1]$. The turbulent kinematic eddy viscosity is assumed to depend on the distance from the bed. A quadratic law with vanishing values at the reference level and at the free surface is employed

$$\nu_T = D \frac{\partial U}{\partial \eta} L(\eta)^2 \quad , \quad L(\eta) = \kappa(\eta + \eta_R)(1 - \eta)^{1/2} \quad , \quad \eta_R = \frac{R(\xi,t)}{D(\xi,t)} \simeq \frac{2.5 d_s}{30}, \tag{3.25}$$

where $d_s$ is the dimensionless mean grain size of the homogeneous sandy bed.

Assuming that the height of the sandy patterns is much smaller than the local water depth, the flow field can be evaluated by means of a perturbation approach. The hydrodynamic problem can be split into the evaluation of a basic flow field, which describes a uniform water flow over a flat sandy bottom, and the flow field perturbations owing to the presence of small amplitude dunes:

$$\begin{Bmatrix} U \\ V \\ P \\ R \\ D \\ \nu_T \\ t_N \\ t_T \end{Bmatrix} = \begin{Bmatrix} U_0(\eta) \\ 0 \\ P_0(\eta) \\ R_0 \\ 1 \\ \nu_{T0}(\eta) \\ t_{N0}(\eta) \\ t_{T0}(\eta) \end{Bmatrix} + \epsilon \begin{Bmatrix} U_1(\xi,\eta,t) \\ V_1(\xi,\eta,t) \\ P_1(\xi,\eta,t) \\ R_1(\xi,t) \\ D_1(\xi,t) \\ \nu_{T1}(\xi,\eta,t) \\ t_{N1}(\xi,\eta,t) \\ t_{T1}(\xi,\eta,t) \end{Bmatrix} \tag{3.26}$$

where $\epsilon << 1$ is the ratio between the small amplitude of the bottom perturbations and the mean water depth.

At the leading order of approximation, the continuity equation along with the no-slip condition lead to the vanishing of the vertical velocity component:

$$\frac{dV_0}{d\eta} = 0 \, , \tag{3.27}$$

$$V_0 = 0 \quad \text{at} \quad \eta = 0 \, . \tag{3.28}$$

Momentum equations and boundary conditions constitute a system of ordinary differential equations which reads

$$1 + \frac{d\nu_{T0}}{d\eta}\frac{dU_0}{d\eta} + \nu_{T0}\frac{d^2U_0}{d\eta^2} = 0 \tag{3.29}$$

$$\frac{dP_0}{d\eta} = -\frac{1}{S} \tag{3.30}$$

$$U_0 = 0 \quad \text{at} \quad \eta = 0 \tag{3.31}$$

$$t_{N0} = -P_0 = 0 \quad \text{at} \quad \eta = 1 \tag{3.32}$$

$$t_{T0} = \nu_{T0}\frac{dU_0}{d\eta} = 0 \quad \text{at} \quad \eta = 1 \tag{3.33}$$

The vertical momentum equation along with the vertical dynamic condition at the free surface give the hydrostatic pressure distribution

$$P_0 = \frac{1-\eta}{S}\,, \tag{3.34}$$

while the horizontal momentum equation along with the remaining boundary conditions at the free surface lead to the well-known logarithmic law for the profile of the horizontal velocity component

$$U_0 = \frac{1}{\kappa}\log\left(\frac{\eta+\eta_R}{\eta_R}\right)\,. \tag{3.35}$$

It turns out that the kinematic turbulent eddy viscosity is consistent with the logarithmic velocity profile

$$\nu_{T0} = \kappa(\eta+\eta_R)(1-\eta)\,. \tag{3.36}$$

Once the dimensionless mean grain size of the homogeneous sandy bed is given, the equivalent roughness length can be evaluated, and, in turn, the vertical profile of both the uniform flow velocity and turbulent eddy viscosity at the leading order of approximation can be found (Figure 3.3).

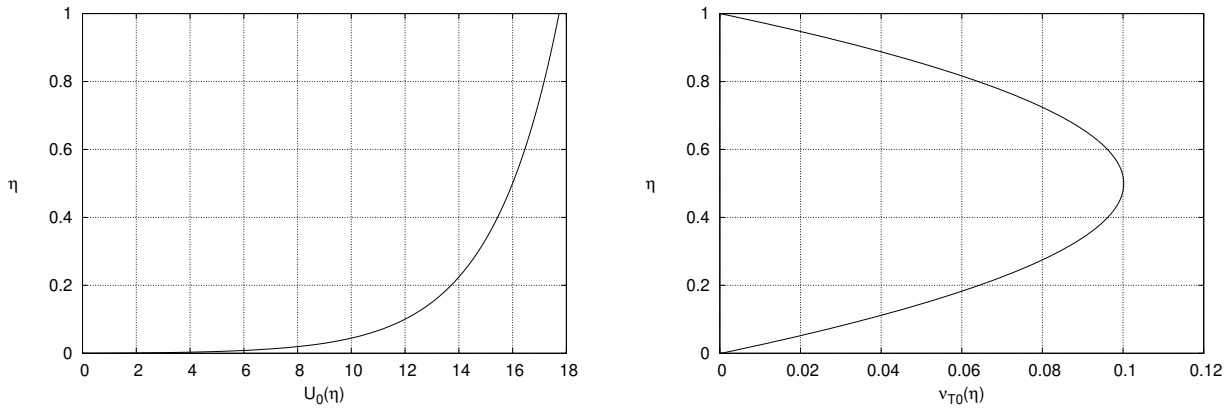


Figure 3.3: Dimensionless horizontal velocity component (left panel) and kinematic eddy viscosity (right panel) over the transformed vertical coordinate considering a dimensionless mean grain size $d_s = 0.01$, a value close to the physical modelling presented in Chapter 1.

As far as the formation of regularly spaced dunes is concerned, it is possible to assume the periodicity of the bottom geometry. The sandy bottom is expressed as superposition of different spatial components and the flow field perturbations, owing to the presence of each spatial component, can be expressed in the following form:

$$\begin{Bmatrix} U \\ V \\ P \\ R \\ D \\ \nu_T \\ t_N \\ t_T \end{Bmatrix} = \begin{Bmatrix} U_0(\eta) \\ 0 \\ P_0(\eta) \\ R_0 \\ 1 \\ \nu_{T0}(\eta) \\ t_{N0}(\eta) \\ t_{T0}(\eta) \end{Bmatrix} + \epsilon \begin{Bmatrix} u(\eta,t) \\ v(\eta,t) \\ p(\eta,t) \\ r(t) \\ d(t) \\ \nu_t(\eta,t) \\ t_n(\eta,t) \\ t_t(\eta,t) \end{Bmatrix} e^{i\alpha\xi} + c.c. \,, \tag{3.37}$$

where $\alpha$ denotes the longitudinal dimensionless wavenumber of the bottom waviness.

At order $O(\epsilon)$, a set of linearly independent first order ordinary differential problems describes the flow field perturbations:

$$\frac{du}{d\eta} + \frac{i\alpha}{2} v - \frac{t_t}{2\nu_{T0}} = 0 \tag{3.38}$$

$$i\alpha u + \frac{dv}{d\eta} = i\alpha(r + \eta d)\frac{dU_0}{d\eta} \tag{3.39}$$

$$-i\alpha U_0 u - 4\nu_{T0}\alpha^2 u - \frac{dU_0}{d\eta} v + \frac{dt_t}{d\eta} + i\alpha t_n = \left[-i\alpha U_0 \frac{dU_0}{d\eta} + \frac{i\alpha}{S} - 2\alpha^2(1-\eta)\right](r+\eta d) - d \tag{3.40}$$

$$-i\alpha U_0 v + i\alpha t_t + \frac{dt_n}{d\eta} = \frac{d}{S} + i\alpha(r + \eta d) - 2i\alpha(1-\eta)d \tag{3.41}$$

The boundary conditions read

$$u = 0 \quad , \quad v = 0 \quad \text{at} \quad \eta = 0 \tag{3.42}$$

$$t_t = 0 \quad , \quad t_n = 0 \quad \text{at} \quad \eta = 1 \tag{3.43}$$

$$v = i\alpha(r + \eta d)U_0 \quad \text{at} \quad \eta = 1 \tag{3.44}$$

### 3.2.2 Morphodynamic model

From the knowledge of the flow field, it is possible to obtain an estimate of the net sediment transport. In the present formulation, suspended sediment transport is neglected and only the bed-load transport is considered, i.e. sliding, rolling and saltating grain particles. Such assumption seems reasonable since sand dunes are more likely to appear in sub-critical flows (Fredsøe, 1974), the bottom shear stress generated by which turns out to be too weak to produce large suspension of the sediment.

A common and useful approach to the quantification of bed-load transport is to empirically relate the sediment transport rate $q_B^*$ with both the bottom shear stress $t_{TB}^*$ and its critical threshold value for incipient motion $t_{TC}^*$. A large number of empirical relations have been derived using flume data from many laboratory experiments. Most of the available relations posed in a suitable dimensionless form share the structure

$$\frac{q_S^*}{\sqrt{(s-1)g^* d_s^{*3}}} = \Phi(\Theta_B, \Theta_C) \ , \tag{3.45}$$

where $s$ represents the relative density of the sediment, $\Phi$ is the dimensionless bed-load transport rate and $\Theta_B$ is the Shields parameter, which represents the dimensionless shear stress at the bottom

$$\Theta_B = \frac{t_{TB}^*}{g^* \rho^* (s-1) d_s^*} \ . \tag{3.46}$$

The Shields parameter is evaluated at the saltation level $B(\xi, t)$, which is the interface between the flowing fluid and the very thin saltation layer where grains are involved in bed-load transport processes (Colombini, 2004). The saltation level is assumed parallel to the reference level at a distance equal to the saltation layer thickness, which, under uniform flow condition, is estimated on the basis of some empirical formulae by Sekine and Kikkawa (1992)

$$B(\xi, t) = R(\xi, t) + h_B \ \ , \quad h_B = l_B d_s = \left\{ 1 + A_B \left( \frac{t_{TR}^* - t_{TC}^*}{t_{TC}^*} \right)^{m_B} \right\} d_s. \tag{3.47}$$

where $t_{TR}^*$ is the shear stress evaluated at the reference level and $A_B$, $m_B$ are empirical parameters. Such a slight modification of the absolute value of the shear stress leads to a remarkable difference in terms of the phase of the shear stress relative to the bottom elevation, which drives the instability of the sandy bed forced by the fluid flow (Colombini, 2004).

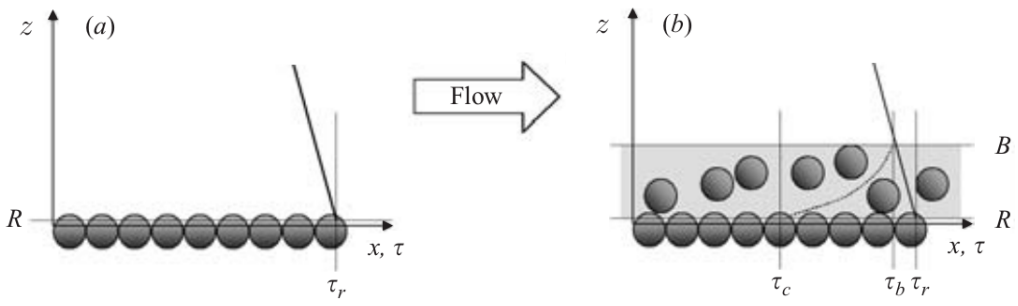


Figure 3.4: Sketch of the bed-load level and the thickness of the saltation layer.

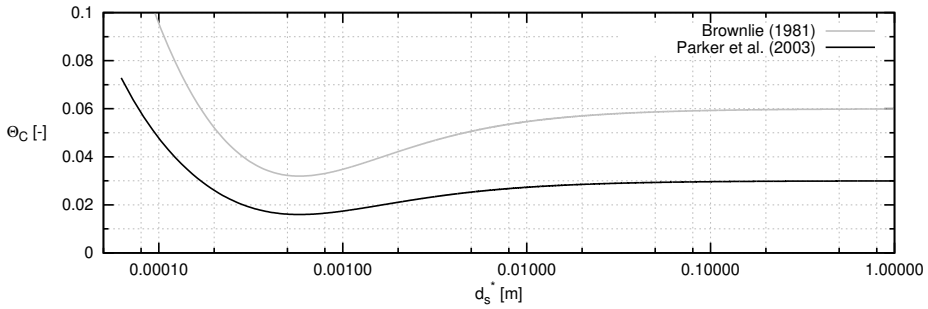


Figure 3.5: Shields threshold value versus the mean grain size of the sediment. Grey line represents the fitted curve by Brownlie (1981), while black line represents the modified Shields threshold by Parker et al. (2003).

In the case of an unperturbed flat bed consisting of non-cohesive sediment, Shields (1936) determined experimentally that a threshold value of the Shields parameter is required to initiate the motion of the sediment particles. The critical Shields parameter can be estimated following Brownlie (1981), who fitted a curve to the experimental line of Shields. In the limit of sufficiently large particle Reynolds number $R_p$, based on information contained in Neill (1968), Parker et al. (2003) amended the Brownlie's relation to

$$\Theta_C = \frac{1}{2}\left(0.22R_p^{-0.6} + 0.06e^{-17.77R_p^{-0.6}}\right) , \tag{3.48}$$

where $R_p$ is the particle Reynolds number of the sediment

$$R_p = \frac{\sqrt{(s-1)g^* d_s^{*3}}}{\nu} . \tag{3.49}$$

Since the problem under formulation accounts for the presence of bottom perturbations, the bed is far from being flat and the stabilising effect of gravity, which opposes uphill motion and favour downhill motion, is considered adopting a correction for the threshold Shields stress (Fredsøe and Deigaard, 1992)

$$\Theta_{TH} = \Theta_C \left[1 - \left(S - \frac{\partial B}{\partial \xi}\right)\frac{1}{\mu_c}\right] , \tag{3.50}$$

where $\mu_c$ is the Coulomb coefficient. A pile of sediment under water at resting at the angle of repose $\Psi$ represents a threshold condition. Any slight disturbance causes the failure of the pile, and thus the motion of the sediment. The difference between the gravitational force and the buoyancy force acting on a single grain particle lying on the slope of the pile results in a net downslope force. The balance between this destabilising force and the stabilising friction force requires that $\mu_c = \tan(\Psi)$. For natural sediments, the angle of repose $\Psi$ ranges between $30$ and $50$ resulting in friction coefficient $\mu_c$ ranging between $0.58$ and $1.2$. Such a static representation strongly simplify the sediment particle dynamics. It turns out that the dynamic friction coefficient assumes smaller values than its static counterpart. Since in the literature no well established values of the dynamic friction coefficient can be found, following the recommendations by Fredsøe and Deigaard (1992), a dynamic friction coefficient $\mu_d$ has been employed, the value of which has been set equal to $0.5\mu_c$.

A large assortment of sediment transport predictors based on good data sets exists which estimates bed-load transport for well-sorted sediment mixtures. The most important relation from a historical point of view is the classical Meyer-Peter and Müller (1948) formula. The relation was derived using flume data pertaining to uniform sediment in the gravel sizes ($d_s^*$ ranging between $5.21$ mm and $28.65$ mm). Later, Wong and Parker (2006) found an error in the analysis of Meyer-Peter and Müller (1948). A subsequent analysis of the experimental data used by Meyer-Peter and Müller (1948) resulted in the following corrected relation

$$\Phi = 3.97\,(\Theta_B - \Theta_C)^{3/2} \quad \text{with} \quad \Theta_C = 0.0495\ . \tag{3.51}$$

The fixed critical Shields parameter must be considered as only a matter of convenience for correlating the experimental data. As already pointed out, the critical Shields parameter should be a function of the mean grain size, and this fact results in some of the scatter between the existing relations. Among the commonly-quoted bed-load transport predictors is the Fernandez Luque and Van Beek (1976) formula, which reads

$$\Phi = 5.7\,(\Theta_B - \Theta_C)^{3/2} \quad \text{with} \quad \Theta_C = 0.037 \div 0.0455\ . \tag{3.52}$$

The predictor relation appears to contain the main physical ingredients controlling the process of sediment transport for values of the Shields parameter close to its threshold. Furthermore, the bed material tested in the experiments on which the above relation is based included different grain sizes ranging from sand to gravel. The experimental values of the critical Shields stress generally track the Brownlie's curve. It is worth pointing out that this relation has been plotted well outside of the experimental data used to derive it. In the data used by Fernandez Luque and Van Beek (1976), $\Theta_B$ never exceeded $0.11$, whereas their plot extends to $\Theta_B = 1$.

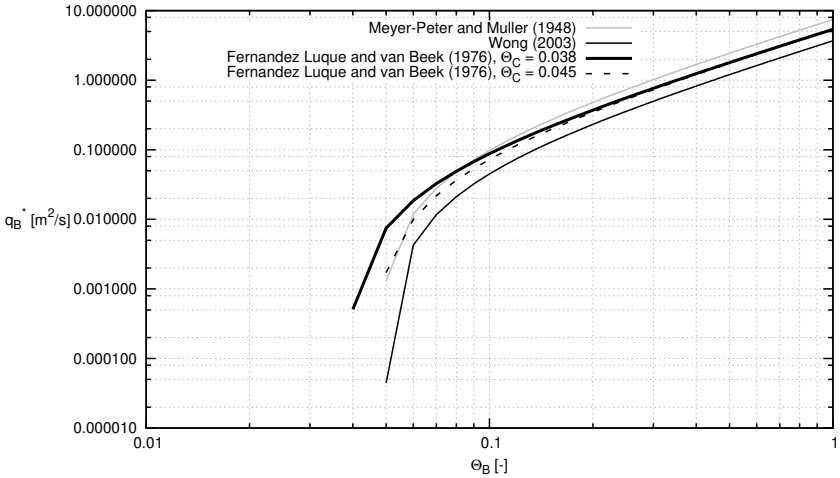


Figure 3.6: Bed-load sediment transport rate versus the Shields stress. The thin grey line represents the original Meyer-Peter and Müller (1948) relation, while the thin black line represents its modified version Wong and Parker (2006). The thik black line represents the Fernandez Luque and Van Beek (1976) formula with a critical Shields parameter equal to $0.038$ ($d_S^* \sim 1$ mm), while for a critical Shields parameter equal to $0.045$ ($d_S^* \sim 3$ mm) the relation is plotted by a dashed black line.

Finally, the local time development of the bottom configuration can be estimated by the sediment continuity equation, which simply states that locally the positive (negative) divergence of the sediment transport rate should be balanced by the increase (decrease) of the bottom elevation,

$$\frac{\partial B(\xi,T)}{\partial T} = -\frac{\partial \Phi(\xi,T)}{\partial \xi} \quad , \quad T = \frac{t^*\sqrt{(s-1)g^* d_s^{*3}}}{D_0^{*2}(1-p)} \, , \tag{3.53}$$

where $T$ is a slow morphodynamic time scale.

Linearizing all the above introduced morphodynamic formulae, and coupling them with the linear hydrodynamics previously described, it is possible to perform a linear stability analysis. Such stability analysis entails few main steps. First of all, the generic bottom perturbation of small amplitude is written as an exponential function of the longitudinal coordinate

$$B(\xi,T) = R_0 + h_B + \epsilon B_1(\xi,T) = R_0 + h_B + \epsilon b(T) e^{i\alpha\xi} + c.c. \, . \tag{3.54}$$

At this point it is worth noting that the time-varying amplitude of the perturbation of the bed-load level $b$ equals the amplitude of the perturbation of the reference level $r$.

Directly from the knowledge of the perturbed flow field, it is possible to evaluate the perturbation of the Shields parameter which is related with the shear stress exerted by the flow over the perturbed sandy bottom

$$\Theta_B(\xi,t) = \Theta_{B0} + \epsilon\theta_b(t)e^{i\alpha\xi} + c.c. = \frac{S}{(s-1)d_s}\left[t_{TB0} + \epsilon t_{tb}(t)e^{i\alpha\xi} + c.c.\right] \tag{3.55}$$

At the leading order of approximation the Shields parameter turns out to be

$$\Theta_{B0} = \frac{S}{(s-1)d_s} t_{TB0} = \frac{S}{(s-1)d_s}\left[\nu_{T0}\frac{dU_0}{d\eta}\right]_{\eta_B} = \frac{S}{(s-1)d_s}(1-\eta_B) \, , \tag{3.56}$$

where $\eta_B = \eta_R + h_B$ represents the dimensionless distance between level $B$ and level $R$, while at the first order of approximation the perturbed Shields parameter turns out to be

$$\theta_b = \frac{S}{(s-1)d_s} t_{tb} = \frac{S}{(s-1)d_s}\left[2\nu_{T0}\left(\frac{du}{d\eta} + \frac{i\alpha}{2}v\right)\right] \, . \tag{3.57}$$

Then, accounting for the gradient of the bed level along the longitudinal coordinate, the perturbation of the threshold Shields stress reads

$$\Theta_{TH}(\xi,t) = \Theta_{TH0} + \epsilon\theta_{th}(t)e^{i\alpha\xi} + c.c. = \Theta_{C0}\left(1 - S/\mu_d\right) + \epsilon i\alpha\Theta_{C0}/\mu_d b(t)e^{i\alpha\xi} + c.c. \tag{3.58}$$

Finally, it is possible to evaluate the sediment transport rate related with the presence of the generic bottom perturbation

$$\Phi(\xi,T) = \Phi_0 + \epsilon\phi(t)e^{i\alpha\xi} + c.c. = \Phi_0 + \epsilon\left(\frac{\partial\Phi}{\partial\Theta_B}\right)_0(\theta_b - \theta_{th})e^{i\alpha\xi} + c.c. \tag{3.59}$$

The linearised sediment continuity equation leads to the following dispersion relationship

$$\frac{1}{b}\frac{db}{dT} = -i\alpha\frac{\phi}{b} = -i\omega_\alpha \quad \Rightarrow \quad b(T) = e^{-i\omega_\alpha T} = e^{-i\omega_{\alpha R}T}e^{\omega_{\alpha I}T} \, . \tag{3.60}$$

An exponential dependence of the solution on time emerges, and, in turn, its complex argument is able to describe the time development of the generic bottom perturbation. It turns out that the imaginary part of the complex quantity $\omega_{\alpha I}$ describes the growth (decay) of the bottom perturbation related to the wavenumber $\alpha$, while its real counterpart $\omega_{\alpha R}$ describes its migration.

## 3.3 Semi-analytical results

The linear system of coupled ordinary differential equations can be re-written in the general form

$$\mathcal{A}\,\mathbf{x} = d\,\mathcal{B}_d + r\,\mathcal{B}_r \tag{3.61}$$

where $d$ is considered as a parameter to be determined and $r$ represents the amplitude of the perturbation of the reference level. The vector $\mathbf{x}$ of the unknowns of the problem is

$$\mathbf{x} = (u, v, t_t, t_n)^T. \tag{3.62}$$

The linear differential operator $\mathcal{A}$ in (3.61) is

$$\mathcal{A} = \begin{pmatrix} \frac{d}{d\eta} & \frac{i\alpha}{2} & -\frac{1}{2\nu_{T0}} & 0 \\ i\alpha & \frac{d}{d\eta} & 0 & 0 \\ -i\alpha U_0 - 4\nu_{T0}\alpha^2 & -\frac{dU_0}{d\eta} & \frac{d}{d\eta} & i\alpha \\ 0 & -i\alpha U_0 & i\alpha & \frac{d}{d\eta} \end{pmatrix}, \tag{3.63}$$

while the vector $\mathcal{B}_d$ and $\mathcal{B}_r$ are

$$\mathcal{B}_d = \begin{pmatrix} 0 \\ i\alpha\eta\frac{dU_0}{d\eta} \\ \left[-i\alpha U_0\frac{dU_0}{d\eta} + \frac{i\alpha}{S} - 2\alpha^2(1-\eta)\right]\eta - 1 \\ \frac{1}{S} + i\alpha\eta - 2i\alpha(1-\eta) \end{pmatrix} \tag{3.64}$$

and

$$\mathcal{B}_r = \begin{pmatrix} 0 \\ i\alpha\frac{dU_0}{d\eta} \\ -i\alpha U_0\frac{dU_0}{d\eta} + \frac{i\alpha}{S} - 2\alpha^2(1-\eta) \\ i\alpha \end{pmatrix}. \tag{3.65}$$

The problem involving the above ordinary differential operators is not completely defined by its equations. Even more crucial in determining how to attack the problem numerically is the nature of its boundary conditions. Presently the available boundary conditions are specified at two different boundaries, which are the mean bottom and the free surface. As already pointed out these boundary conditions yield the vanishing of $u$ and $v$ at the reference level ($\eta = 0$), the vanishing of $t_t$ and $t_n$ at the free surface ($\eta = 1$), where the kinematic condition is imposed as well. The solution of the ordinary differential problem is found with a standard shooting procedure from the bottom up to the free surface. Equations are numerically integrated by means of a fifth-order Runge-Kutta method with adaptive step-size control. Linearity of the differential system allows to express its solution in the form

$$\mathbf{x} = c_1\mathbf{x}_1 + c_2\mathbf{x}_2 + d\mathbf{x}_d + r\mathbf{x}_r\ . \tag{3.66}$$

Thus, $\mathbf{x}$ is a linear combination of two linearly independent solutions of the homogeneous initial value problems

$$\mathcal{A}\,\mathbf{x}_1 = 0 \quad , \quad \mathcal{A}\,\mathbf{x}_2 = 0\ , \tag{3.67}$$

plus particular solutions of the non-homogeneous differential systems

$$\mathcal{A}\,\mathbf{x}_d = \mathcal{B}_d \quad , \quad \mathcal{A}\,\mathbf{x}_r = \mathcal{B}_r\ , \tag{3.68}$$

each satisfying the no-slip boundary conditions at the reference level. Using the splitting (3.66) on the boundary conditions at the free surface, a linear $3 \times 3$ non-homogeneous algebraic system in the three unknowns $c_1$, $c_2$ and $d$ is found, the solution of which is proportional to $r$

$$\mathbf{c} = (c_1, c_2, d, r)^T = r(t_{tr}, t_{nr}, d/r, 1)^T = r\ \mathbf{C} \tag{3.69}$$

where the two linearly independent solutions of the homogeneous problems have been chosen so that $c_1/r$ and $c_2/r$ are the values of the perturbation of the tangential $t_{tr}$ and normal $t_{nr}$ stress at the reference level, respectively. The vector $\mathbf{C}$ thus provides the forced response of the flow to a unit reference level perturbation. The amplitude $t_{tb}$ of the perturbation of the shear stress evaluated at the bed-load level $t_{TB}$ can be expanded as in (3.66),

$$t_{tb} = c_1 t_{tb1} + c_2 t_{tb2} + d t_{tbd} + r t_{tbr}\ , \tag{3.70}$$

and the amplitude $\theta_b$ of the perturbation of the Shields stress $\Theta_B$ can be expanded as well,

$$\theta_b = \frac{S}{(s-1)d_s} t_{tb} = \frac{S}{(s-1)d_s}\left(c_1 t_{tb1} + c_2 t_{tb2} + d t_{tbd} + r t_{tbr}\right)\ . \tag{3.71}$$

Analogously the amplitude $\phi$ of the perturbation of the bed-load discharge $\Phi$ can be expanded as follows

$$\phi = c_1\phi_1 + c_2\phi_2 + d\phi_d + r\phi_r = \boldsymbol{\phi}\cdot\mathbf{c} = \boldsymbol{\phi}\cdot r\ \mathbf{C} \tag{3.72}$$

where

$$\boldsymbol{\phi} = \begin{pmatrix}\phi_1\\ \phi_2\\ \phi_d\\ \phi_r\end{pmatrix} = \frac{S}{(s-1)d_s}\left(\frac{\partial\Phi}{\partial\Theta_B}\right)_0 \begin{pmatrix} t_{tb1}\\ t_{tb2}\\ t_{tbd}\\ t_{tbr} - \frac{i\alpha\mu}{S/(s-1)d_s}\end{pmatrix}\ . \tag{3.73}$$

Making use of (3.71) and (3.72), the dispersion relationship can be rewritten in the form

$$\omega = \alpha\ \boldsymbol{\phi}\cdot\mathbf{C}\ , \tag{3.74}$$

and determining the imaginary part it is possible to obtain an expression for the growth rate

$$\omega_I = \alpha^2 \frac{S}{(s-1)d_s}\left(\frac{\partial\Phi}{\partial\Theta_B}\right)_0 \left(\frac{t_{tbI}}{\alpha} - \frac{\Theta_{C0}}{\mu_d}\frac{(s-1)d_s}{S}\right) \tag{3.75}$$

which clearly shows how the emergence of small amplitude bottom perturbations is related to a balance between the destabilising effect due to the steady current, represented by the shear stress at the bed-load level, and the stabilising effect due to the gravity, represented by the dynamic friction coefficient.

The investigation of the dispersion relationship allows possible instability regions to be isolated in the parameter space. Among the free parameters of the stability-based model are the unperturbed flow depth $D_0^*$ and the uniform mean grain size of the sediment $d_s^*$, which determines the equivalent roughness length $k_s^*$, and, in turn, the conductance coefficient characterising the unperturbed steady stream

$$\mathcal{C} = \frac{1}{\kappa}\ln\left(\frac{11.09 D_0^*}{k_s^*}\right)\quad,\quad k_s^* = 2.5 d_s^*\ . \tag{3.76}$$

Once the angle of repose of the bed material $\Psi$ is assigned, the dynamic friction coefficient $\mu_d$ can be evaluated which regulates the effect of gravity.

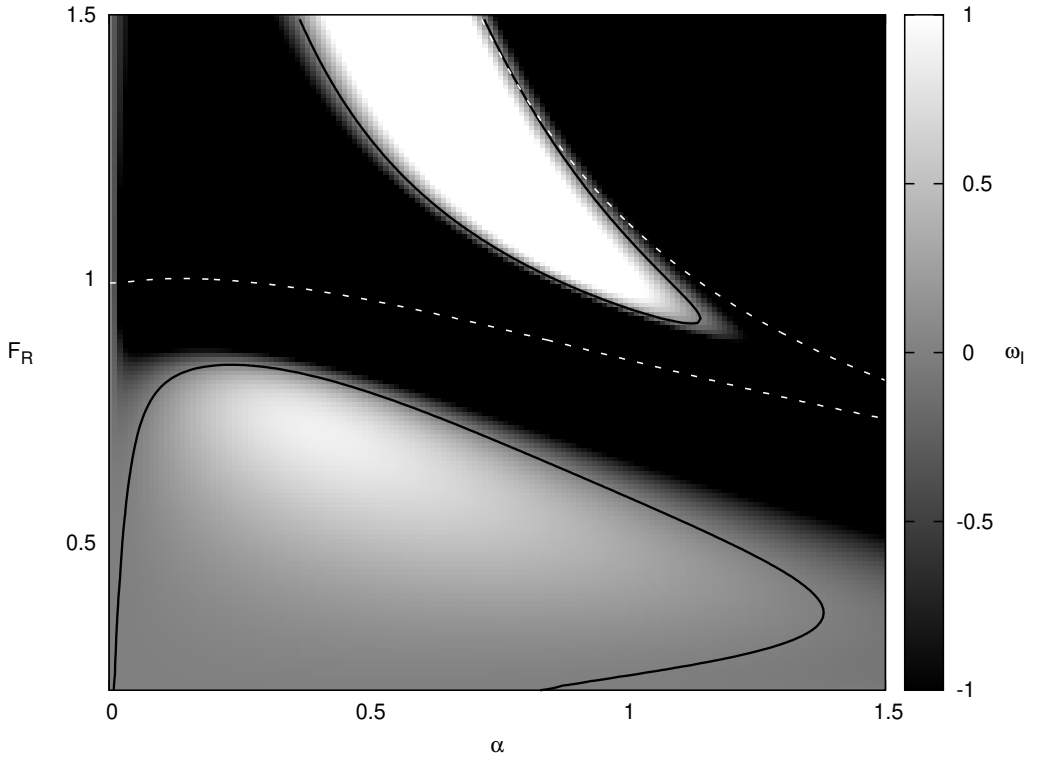


Figure 3.7: Growth rate plotted in shades of grey for values of the free parameters $\mathcal{C} = 20$, $\Psi = 40°$. Thick black lines represent the curves of vanishing growth rate, while dashed white lines represent the curves of vanishing celerity.

Finally, it is possible to compute the growth rate $\omega_{\alpha I}$ related with the generic bottom perturbation represented by its dimensionless wavenumber $\alpha$ by varying the Froude number $F_R$ of the unperturbed flow. Employing the classical Meyer-Peter and Müller (1948) formula and setting appropriate free parameters (i.e. $\mathcal{C} = 20$, $\Psi = 40°$), the model results confirm the numerical findings by Colombini (2004), which successfully presented an unification of the stability theory of dune and antidunes formation (see Figure 3.7). Two distinct regions of instability can be clearly identified. Values of the parameters for which the growth rate is positive lead to the growth of a limited range of perturbations, indicating instability. The migration rate $\omega_{\alpha R}$ related with the range of unstable modes determines the perturbation celerity. Positive values of the migration rate result in downstream migration, while negative values indicate upstream migration. In Figure 3.7, broken white lines represent vanishing values of the migration rate. Below the lower broken line the celerity of the unstable perturbations turns out to be positive (i.e. downstream migration, dunes), while the unstable perturbations lying above this line has negative celerity (i.e. upstream migration, antidunes).

A comparison of the results of the linear stability analysis with laboratory observations is difficult because experimental data are usually collected when the bottom perturbations are fully developed. On the other hand, to perform a classical linear stability analysis, information on the unperturbed flow are crucial. Colombini (2004) compare the numerical findings with the experimental data by Guy et al. (1966). In the following, the comparison of the results of the present linear stability analysis with the same observations is performed by

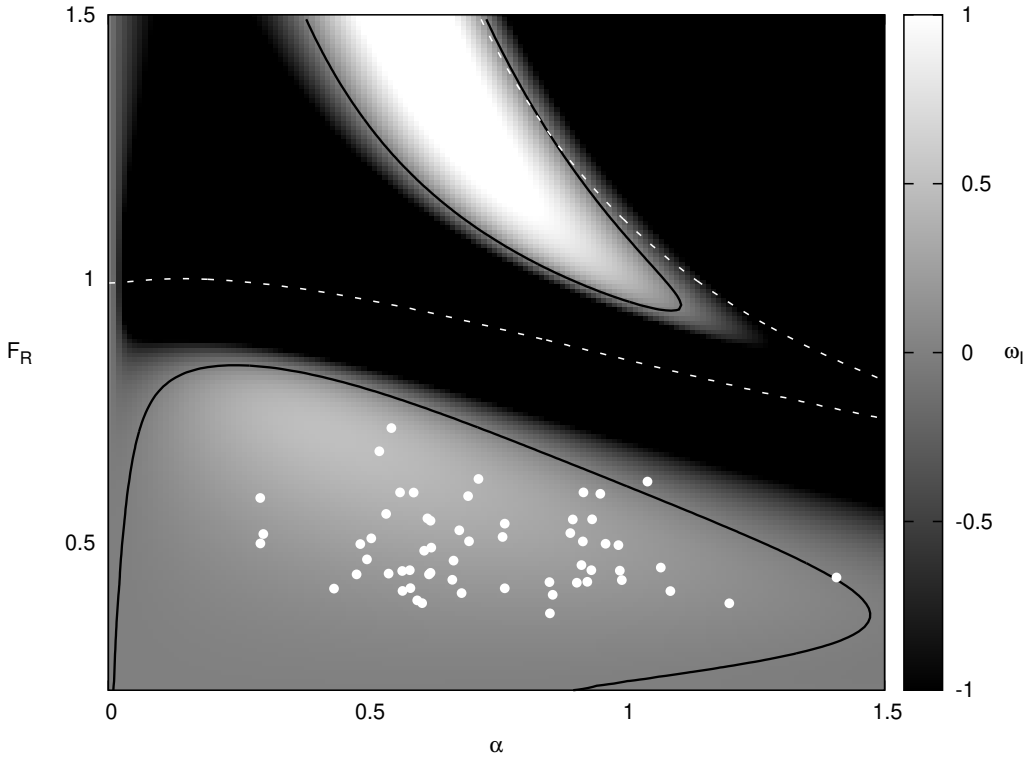


Figure 3.8: Growth rate plotted in shades of grey for values of the free parameters $\mathcal{C} = 19$, $\Psi = 40^\circ$. Thick black lines represent the curves of vanishing growth rate, while dashed white lines represent the curves of vanishing celerity. White points represent the experimental observations by Guy et al. (1966).

employing the Wong and Parker (2006) transport formula, which allows a better matching between numerical results and experimental data. Since the growth of bottom perturbations induces considerable changes of the flow resistance, the mean water depth and the slope of the final equilibrium state observed in the flumes are considerably different from those characterising the initial uniform flow. Furthermore, another difficulty in the interpretation of the experimental results arises because of the presence of smooth sidewalls in the laboratory flumes usually employed for the physical modelling of the problem under investigation. An equivalent uniform flow in an infinitely wide plane bed channel was evaluated from the experimental data disregarding information on the measured slope and friction coefficient and following a procedure similar to the side-wall correction presented in Chapter 2.

Figure 3.8 shows the numerical findings obtained imposing an average value for the conductance coefficient $\mathcal{C} = 19$ characterising the experimental observations by Guy et al. (1966) and a value of the angle of repose equal to $40^\circ$. The successful agreement between the results of the present stability analysis and the experimental data is confirmed by the fact that almost the whole set of measurements concerning the formation of sand dunes falls within the appropriate region of instability. Of note, agreement of model predictions with experimental measurements that confirm the negative growth rates (points outside the solid lines of Figure 3.8: absence of dunes and plane bed or transitional conditions, i.e. upper-stage plane bed) can be found in Colombini and Stocchino (2008).

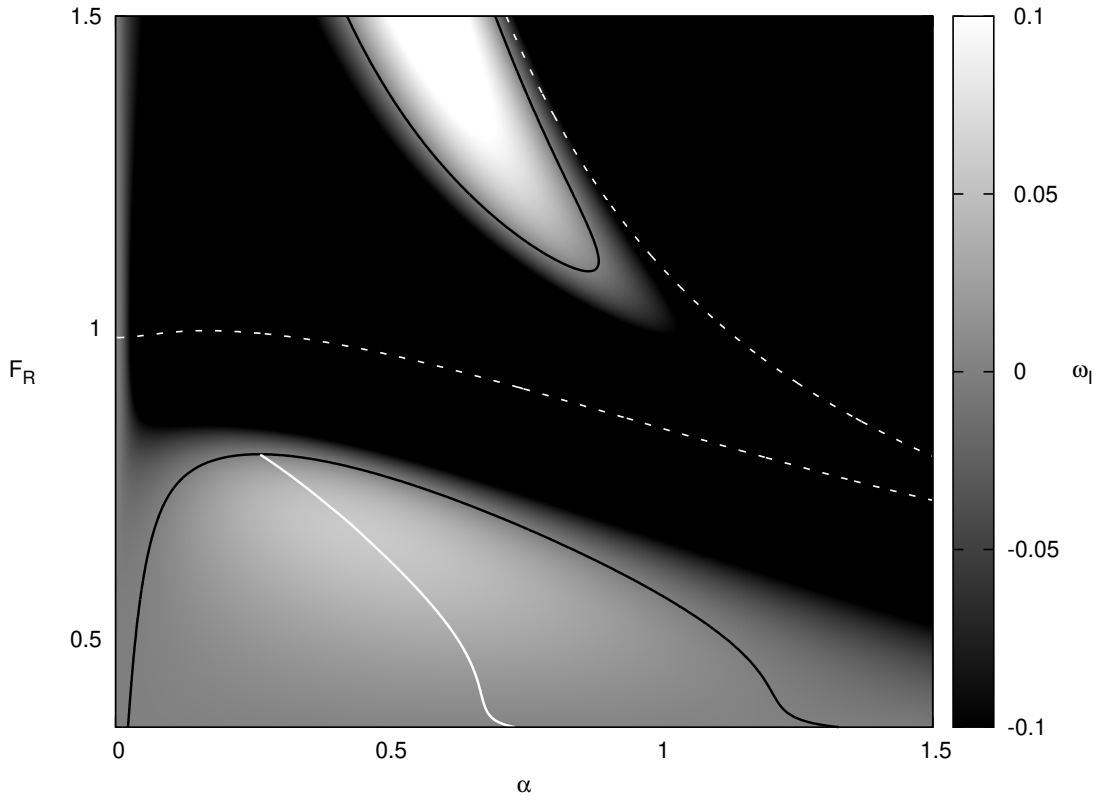


Figure 3.9: Growth rate plotted in shades of grey for values of the free parameters $\mathcal{C} = 15$, $\Psi = 50°$. Thick black lines represent the curves of vanishing growth rate, dashed white lines represent the curves of vanishing celerity, white line represents the fastest growing modes.

In order to compare the results of the linear stability analysis with the experimental observations described in Chapter 2, the value of the mean grain size was set equal to the mean diameter of the well sorted sediment used in the physical modelling $d_s^* = 0.1$. The value of the unperturbed mean water depth was set equal to the uniform depth of the wide open channel flow evaluated by the side-wall correction. Since the experimental work was performed with low energy flows which lead to weak sediment transport during all the experiments, the comparison of the results of the present linear stability analysis with the experimental observations described in the previous chapter is performed by employing the transport predictor by Fernandez Luque and Van Beek (1976), which allows a better matching between numerical results and experimental data.

Furthermore, the study of the dispersion relationship allows the fastest growing mode to be selected among those modes that turn out to be unstable for the assumed hydrodynamic and morphodynamic conditions. By considering a value of the Froude number of the forcing flow close to the value measured during the experiments described in Chapter 2, it is possible to extrapolate from the previous plot the growth curve describing the unstable perturbations for the hydrodynamic and morphodynamic parameters that characterise the physical modelling. Finally, assuming the most unstable mode to prevail on the other over the short-term morphodynamic evolution of the sandy bed, the wavelength of the emerging dunes which is more likely to form can be predicted. Figure 3.10 shows that the present model predicts a

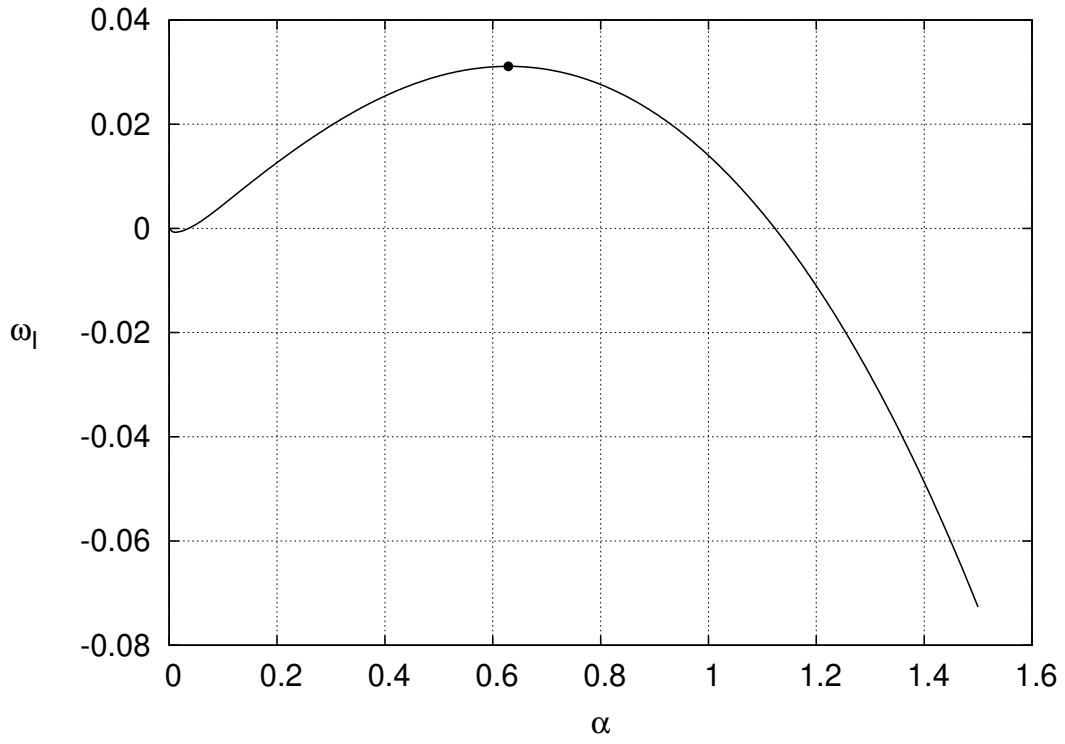


Figure 3.10: Growth rate of the bottom perturbations plotted versus the perturbation wavenumber evaluated by means of the linear stability analysis for the following values of the parameters $\mathcal{C} = 15$, $\Psi = 50°$, $Fr = 0.5$.

fastest growing mode related with the experiments which is associated with the wavenumber $\alpha = 0.6$, that corresponds to a value of the dimensional wavelength of the fastest growing perturbation approximately equal to $\lambda^* = 1\ m$, a value which is of the same order of the wavelengths of the alluvial dunes observed at the end of the experiments.

## 3.4 Numerical modelling

Among the main limitations of standard linear stability analyses is the assumption of full mobility conditions. When a motionless substratum is exposed by the formation of sand dunes, the lack of sediment affects its transport, and, in turn, the pattern morphology. The baring of the motionless substratum leads to supply-limited conditions. Local entrainment of sediment is prevented by the presence of the motionless substratum, and, therefore, the amount of sediment in motion is smaller than the local transport capacity. All the previously introduced predictor formulae quantifying the sediment transport rate cannot be applied in the case of supply-limited conditions unless a suitable numerical procedure is introduced that is capable of account for the local lack of mobile sediment. Presently the numerical procedure outlined by Blondeaux et al. (2016) has been employed. Where sand is available, the sediment transport is thought to be dependent only on the bottom shear stress. If the shear decreases (increases) in the flow direction, the sediment transport rate can be predicted by standard predictor formulae and some deposition (erosion) occurs accordingly with the sediment continuity. Differently, where the motionless substratum is locally exposed ($x^* = x^*_{exp}$), the value of the local sediment transport rate $\Phi(x^*)$ depends not only on the local value of the shear stress $\Theta_B(x^*)$ but on its spatial derivative as well. If the shear stress increases in the direction of the flow, the sediment transport rate remains constant since the flow cannot entrain additional mobile sediment. On the other hand, if the shear stress decreases in the direction of the flow, two different scenarios are possible depending on the upstream value of the sediment transport rate. If the upstream value of the sediment transport rate is smaller than the value predicted locally by standard predictor formulae $\Phi_P(x^*)$ due to the upstream baring of the motionless substratum, the local sediment transport rate should be assumed equal to its upstream value. Otherwise, the local value of the sediment transport rate should be the value predicted by standard predictor formulae and some deposition of sediment over the exposed substratum should occur accordingly with the sediment continuity.

$$\Phi(x^*_{exp}) = \Phi(x^*_{exp} - dx^*) \quad \text{if} \quad \left.\frac{d\Theta_B}{dx^*}\right|_{x^*_{exp}} > 0 \,, \tag{3.77}$$

$$\Phi(x^*_{exp}) = \Phi(x^*_{exp} - dx^*) \quad \text{if} \quad \left.\frac{d\Theta_B}{dx^*}\right|_{x^*_{exp}} < 0 \;\text{ and }\; \Phi(x^*_{exp} - dx^*) < \Phi_P(x^*_{exp}) \,, \tag{3.78}$$

$$\Phi(x^*_{exp}) = \Phi_P(x^*_{exp}) \quad \text{if} \quad \left.\frac{d\Theta_B}{dx^*}\right|_{x^*_{exp}} < 0 \;\text{ and }\; \Phi(x^*_{exp} - dx^*) > \Phi_P(x^*_{exp}) \,. \tag{3.79}$$

These simple rules (3.77-3.79) introduce strong nonlinearities and the time-development of the bottom configuration can be obtained only by numerical means. The present numerical model integrates in time and space the dimensionless sediment continuity equation. The time-advancement of (3.53) is obtained by means of a Runge-Kutta second-order approach, while the spatial derivatives are replaced by their second-order finite difference approximation. A computational domain of length $L^*_d$ along the horizontal axis $x^*$ is considered and periodic boundary conditions are applied at its ends ($x^* = 0$, $x^* = L^*_d$). The dimensionless length of the computational domain $L_d = L^*_d/D^*_0$, the thickness of the initial sand layer $\Delta = \Delta^*/D^*_0$, the initial small amplitude of the bottom configurations $A_0 = A^*_0/D^*_0$ and its wavenumber $\alpha^* = 2\pi D^*_0/\lambda^*_\alpha$ are the free geometrical parameters of the numerical model. At this point it is worth noting that when sediment starvation leads to the emergence of starved bedforms which are no longer purely sinusoidal, the conservation of the volume of sand

forces the amplitude $A(T) = \Delta\lambda_\alpha/\lambda_{TT}$, where $\lambda_{TT}$ is the trough-to-trough distance (chord) of the emerging starved dunes. The value of $L_d$ is chosen large enough to assume its influence on the time-development of the bottom configuration to be negligible. Furthermore, $L_d$ should be large enough to represent fairly well the formation of the fastest growing mode predicted by the linear stability analysis. Since the time-development of the entire range of unstable modes has to be described with sufficient accuracy, the spatial discretization should be accurate enough to represent the smaller wavelength of the unstable modes predicted by the linear stability analysis with a suitable number of computational points. Of note, in those regions of transition between the rigid substratum and the sandy bed, oscillations of small amplitude and wavelength appear that are a spurious output of the numerical approach as a result of the Gibbs' effect related with the local discontinuity of the bottom elevation. In its numerical time stepping, the present numerical model forces the bed elevation to never drop below the substratum's level by introducing a filtering procedure which remove the small-scale spurious oscillations that has to be in accordance with the sediment continuity. Finally, denoting with $\Delta x^*$ and $\Delta T$ the grid size and the time step used in the numerical integration of equation (3.53), some of the numerical simulations were repeated halving both the grid size and the time step. The results indicate that the chosen couple of values ($\Delta x^*$, $\Delta T$) does not affect the time-development of the bottom configuration.

## 3.5 Numerical results

### 3.5.1 Numerical Stability Analysis

In the present subsection, we explore the possibility of performing a stability analysis of the formation of small amplitude fluvial dunes where the supply limitation affects their dynamics and morphology. To test whether the numerical model can provide a reliable description of the nonlinear effects triggered by the baring of a motionless substratum, the time development of an initial bottom perturbation is numerically integrated in space and time by considering two different cases. The first case is characterised by an infinite availability of the sediment, i.e. alluvial conditions, whereas in the second case the formation of sandy patterns bares a motionless substratum underlying a finite layer of sand of given thickness $\Delta^*$, i.e. supply limited conditions.

In order to compare the numerical results with the analytical findings provided by the linear stability analysis, small amplitude perturbations of the interface between the sandy bottom and the flowing fluid are considered in both cases. In alluvial conditions, for values of the flow and sediment parameters so as the sandy bottom is unstable, the wavelength of the emerging alluvial dunes can be predicted by means of the linear stability analysis described in the previous section. Such analytical findings describe an exponential growth of the amplitude of the unstable modes [see (3.60)] which takes place on the slow morphodynamic time scale [see (3.53)], the growth rate of which can be computed for the range of unstable modes by (3.75).

An alternative description of the exponential growth of the unstable modes predicted by analytical means can be performed by the present numerical model. Considering the wavenumber range of the unstable modes, numerical simulations are performed starting from

an initial bottom perturbation $A_0 cos(\alpha x)$ and the numerical growth rate $\omega_{\alpha N}$ is computed as

$$\omega_{\alpha N} = \frac{\ln\left[A(T_{end})_\alpha / A_0\right]}{T_{end}} \,, \tag{3.80}$$

where $A(T_{end})$ represents the amplitude of the generic bottom perturbation at the end of the simulation time window $T_{end}$. If the final amplitude of the growing perturbation is smaller than the initial thickness of the sand layer ($A(T_{end}) < \Delta$), the growth of the unstable modes turn out to be exponential and the growth rates obtained by means of the numerical procedure match the analytical values predicted by the linear stability analysis (see Figure 3.11 and Figure 3.12). On the other hand, if an initial amplitude of the growing perturbations is considered which is equal to the thickness of the initial sand layer ($A_0 = \Delta$), the emerging bottom perturbations bare the motionless substratum throughout the whole simulation time window and nonlinear effects modify the exponential growth of the unstable modes. In this case, in order to quantify the growth of the bottom perturbations and to gain information on the most unstable mode which is supposed to prevail under supply limited condition, the following quantity is adopted

$$\bar{\omega}_{\alpha N} = \frac{\ln\left[A(T_{end})_\alpha / \Delta\right]}{T_{end}} \,. \tag{3.81}$$

In Figure 3.11 the analytical growth curve predicted by the linear stability analysis is compared with the numerical results in the case of alluvial conditions and in the case of supply limited conditions. The values of the flow and sediment parameters are $\mathcal{C} = 15$, $Fr = 0.5$, $s = 1.65$ and $\mu_d = 0.6$. Such values were chosen because they fall in the range of the values typical of the physical modelling described in Chapter 2. In particular, these values correspond to sand grains ($\rho_s^* = 1650 kgm^{-3}$) characterised by a mean grain size $d_s^*$ equal to $1\ mm$ and dragged by a uniform steady current in a mean water depth $D_0^*$ equal to $10\ cm$ with a depth averaged velocity $\bar{U}^*$ equal to $0.5\ ms^{-1}$. Because of the nonlinearities of the sediment transport the numerical growth rate evaluated in the case of supply limitation depends on the extension of the simulation time window. Since the experiments described in Chapter 2 were stopped after half an hour from the realisation of an uniform flow which forced the initial layer of sand with different degrees of supply limitation, results are presented for different values of the dimensionless time window representing dimensional duration of the numerical simulations of the same order of the duration of the laboratory experiments. It is worth nothing that the morphodynamic time scale $T_m^*$ appearing in equation (3.53) turns out to be much longer than the hydrodynamic time scale of the steady flow and for values of the parameters replacing the laboratory experiments typical values of $T_m^*$ are of the order of tens of minutes.

The last model inputs required by the model are the small amplitude $A_0$ of the initial sinusoidal undulations, which is presently assumed to be two order of magnitude smaller than the dimensionless mean water depth, and, the thickness $\Delta$ of the initial sand layer thickness. Values of $\Delta$ of the order of the mean water depth ($\Delta = 1$) lead to the formation of alluvial dunes, while a value of $\Delta$ equal to the small amplitude of the bottom perturbations ($\Delta = A_0$) leads to supply limited conditions. If the former case is considered, the growth rate $\omega_{\alpha N}$ (white dots in Figure 3.11) of the bottom waviness computed by numerically by means of the present model and that computed analytically by the linear stability analysis $\omega_{\alpha I}$ (solid line in Figure 3.11) are coincident. In this case, the numerical model predicts a maximum value of the growth rate for a wavenumber $\alpha \simeq 0.6$, which is that of the fastest growing alluvial dunes. If the latter case is considered, the motionless substratum becomes exposed and

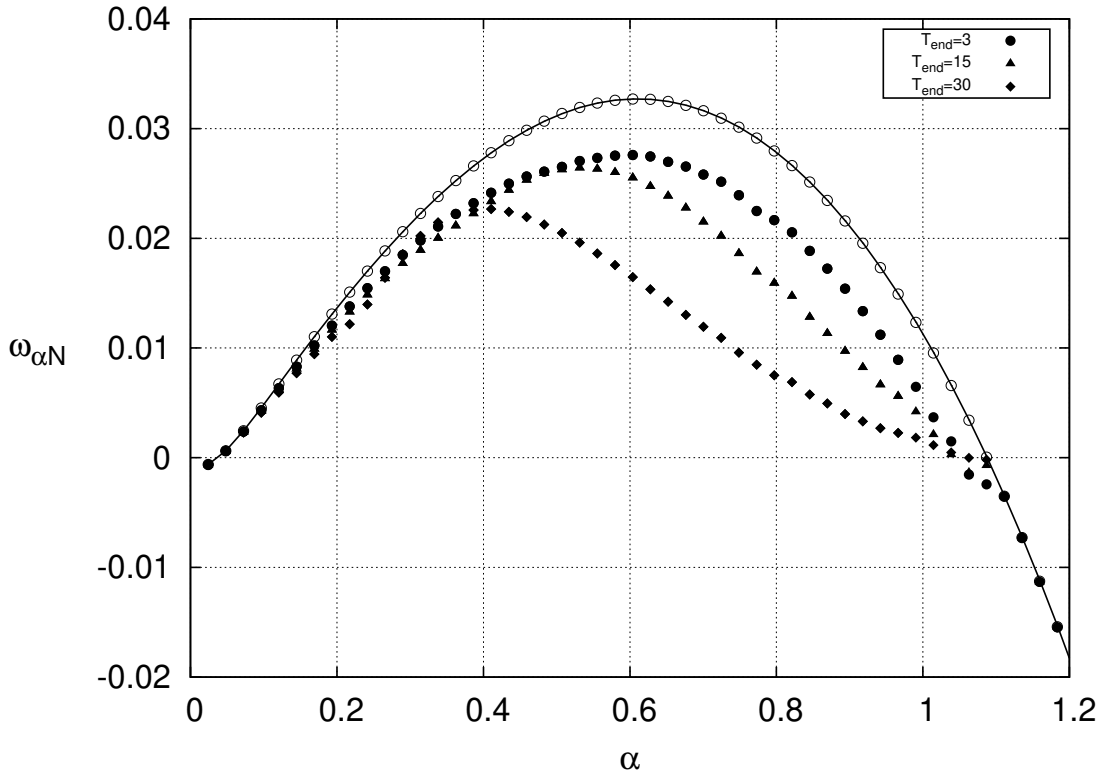


Figure 3.11: Growth rate of the bottom perturbations plotted versus the perturbation wavenumber $\alpha$ for the following values of the parameters $\mathcal{C} = 15$, $\Psi = 50°$, $Fr = 0.5$, $A_0 = 0.01$. Solid line represents the analytical growth rate $\omega_{\alpha I}$ predicted by the linear stability analysis. White dots represent the alluvial growth rate $\omega_{\alpha N}$ for each numerical simulation in alluvial conditions ($\Delta = 1$). Black dots represent the supply limited growth rate $\bar{\omega}_{\alpha N}$ for each numerical simulation in supply limited conditions ($\Delta = A_0$). Different point shape indicate different simulation time window $T_{end}$ reported in the legend.

nonlinear effects modify the growth curve obtained for alluvial conditions. In particular, in this case, the nonlinear sediment transport damps the growth rate of perturbations, especially those with large wavenumbers (smaller wavelengths), and, supply limited dunes predicted by the present numerical stability analysis turn out to be longer than alluvial dunes. This qualitative finding is in agreement with the experimental measurements presented in Chapter 2. Figure 3.11 shows the quantity $\bar{\omega}_{\alpha N}$ for different values of the simulation time $T_{end}$ (see legend of Figure 3.11), then for different degrees of the supply limitation. As expected, as $T_{end}$ decreases, $\bar{\omega}_{\alpha N}$ approaches the values of the growth rate $\omega_{\alpha I}$ predicted by the linear stability analysis. The numerical model predicts a maximum value of the quantity $\bar{\omega}_{\alpha N}$ for a wavenumber $\alpha \simeq 0.55$ considering a $T_{end} = 15$ and $\alpha \simeq 0.4$ considering a $T_{end} = 30$ corresponding to dimensionless wavelengths $\lambda^*$ equal to $1.1\ m$ and $1.5\ m$, respectively. The lengthening of the dunes with an increasing supply limitation is evident. This theoretical finding is in fair agreement with the laboratory observations described in Chapter 2.

The numerical procedure outlined above has been applied to make quantitative predictions of the characteristics of the fluvial dunes observed by Carling et al. (2000) in a supply

limited reach of the river Rhine introduced in Chapter 2. In Figure 3.12 the numerical growth rate of the bottom perturbations which emerge from an infinite layer of sediment (alluvial conditions) is compared with that of the perturbations which develop through a layer of sediment of finite thickness leading to the baring of a motionless substratum (supply limited conditions). The values of the flow and sediment parameters are $\mathcal{C} = 24$, $Fr = 0.15$, $s = 1.65$ and $\mu_d = 0.5$. Such values has been chosen because they fall in the range of the values typical of the field observations by Carling et al. (2000). In particular, these values correspond to a uniform steady flow with depth averaged velocity $\bar{U}^*$ equal to $0.8\ ms^{-1}$ in a mean water depth $D_0^*$ equal to $3\ m$ which entrains a mobile sediment ($\rho_s^* = 1650 kgm^{-3}$) characterised by a mean grain size $d_s^*$ equal to $0.9\ mm$. For these values of the parameters, the dimensional morphodynamic time scale $T_m^*$ attains larger values than that corresponding to the flume experiments of Chapter 2, and, it turns out to be of the order of tens of hours. Since the variations of the river stage recorder by Carling et al. (2000) occur during periods of the order of several days, results are presented for a dimensionless time window $T_{end}$ equal to 15, which represents a dimensional duration of the numerical simulations of the same order of the periods through which the river stream can be approximated by a uniform steady flow. The last model inputs required by the model are the small amplitude $A_0$ of the initial sinusoidal undulations, which is assumed to be two order of magnitude smaller than the mean water depth, and, the thickness $\Delta$ of the initial sand layer thickness. Different values of $\Delta$ has been chosen in order to describe the formation of dunes in alluvial conditions and in supply limited conditions as outlined in the previous paragraph. In the former case (grey line of Figure 3.12), the numerical model predicts a maximum value of $\omega_{\alpha N}$ for a perturbation wavenumber $\alpha \simeq 3.5$ which is that of the fastest growing dunes supposed to prevail on the other unstable modes in alluvial conditions. The corresponding dimensional wavelength $\lambda^*$ is about $5\ m$, a value which fairly reproduces the wavelengths of the two-dimensional small dunes migrating over the stoss side of larger parent bedforms observed by Carling et al. (2000). In the latter case (black line of Figure 3.12), the numerical model predicts a maximum value of $\bar{\omega}_{\alpha N}$ for a perturbation wavenumber $\alpha \simeq 0.5$ which is that of the fastest growing dunes supposed to prevail on the other unstable modes in supply limited conditions. The corresponding dimensional wavelength $\lambda^*$ is about $40\ m$, a value which falls in the range of the wavelengths of the large dunes migrating over a gravel lag layer observed by Carling et al. (2000). The numerical findings turn out to be in qualitative and quantitative agreement with the field observations.

Figure 3.13 shows the time development of the river bed when a thin layer of sediment is present and the initial profile of the bottom is described by the fastest growing mode predicted by the present numerical stability analysis in the case of supply limited conditions. As the initial perturbation grows, the motionless substratum becomes exposed in large regions and nonlinear effects start to play a significant role in the dynamics of the dunes. The crests of the supply limited dunes become sharper than the troughs, which in turn are flat because of the presence of the motionless substratum. Moreover, the bottom profile is asymmetric with respect to the dune crests which attain an humpback profile similar to those of the very large dunes observed by Carling et al. (2000).

### 3.5.2 Time development of an initial random bottom waviness

The present subsection is devoted to test whether the numerical model can provide a reliable description of the physical processes described by the experimental investigation presented in Chapter 2. Analogously to the experimental investigation, a series of numeri-

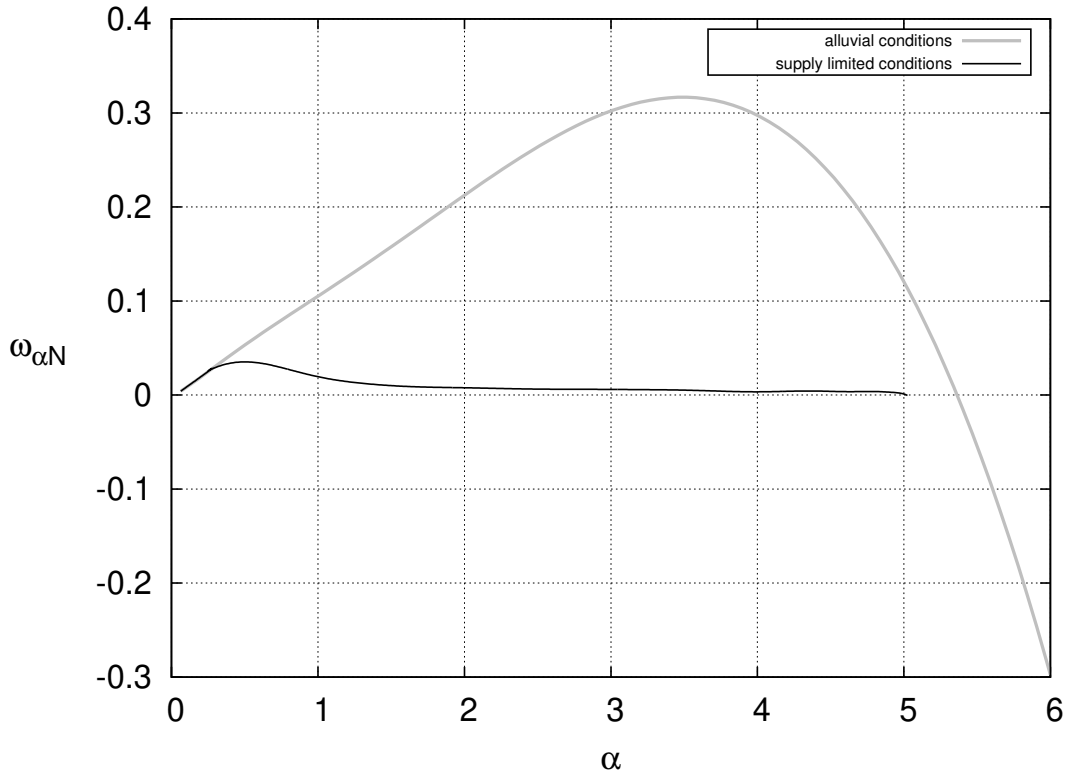


Figure 3.12: Growth rate of the bottom perturbations plotted versus the perturbation wavenumber $\alpha$ for the following values of the parameters $\mathcal{C} = 24$, $\Psi = 45°$, $Fr = 0.15$, $A_0 = 0.01$. Grey line represents the numerical growth curve predicted considering alluvial conditions ($\Delta = 1$). Black line represents the numerical growth curve predicted considering supply limited conditions ($\Delta = A_0$). Results are presented for a dimensionless time window $T_{end}$ equal to 15.

cal simulations is performed computing the time development of an initial random bottom waviness forced by a uniform steady current by fixing hydrodynamic and morphodynamic parameters and varying the supply of sediment. Accordingly to the flume experiments, the sediment supply is decreased by decreasing the dimensionless thickness $\Delta$ of the initial sand layer through which the dunes develop. Decreasing the amount of mobile sediment, the motionless substratum is exposed by the growth of the dune leading to supply-limited conditions. The supply limitation leads to nonlinear sediment transport which turns out to strongly affect the pattern morphology.

The right part of the panels of figure 3.14 show the bottom configurations at the beginning (grey lines) and at the end (black lines) of each numerical simulation. The values of the flow and sediment parameters are $\mathcal{C} = 15$, $Fr = 0.5$, $\Psi = 50°$. The dimensionless length of the computational domain is $L_d = 100$. The thickness of the initial sand layer is progressively decreased starting from $\Delta = 0.25$ (top panel) down to $\Delta = 0.05$ (bottom panel). Taking into account that the assumed mean water depth $D_0^*$ is $0.1\ m$, the first simulation with $\Delta = 0.25$ (panel A) corresponds to an initial dimensional thickness of the sand layer equal to $2.5\ cm$. At the beginning of the simulation, the bottom is flat but for a random perturbation of small

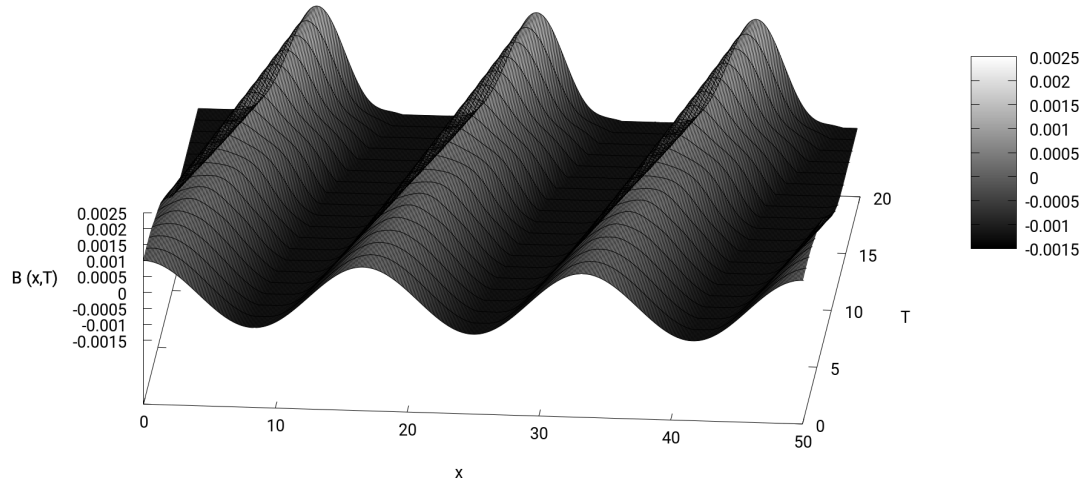


Figure 3.13: Time development of the river bed starting from a small amplitude bottom perturbations ($A_0 = 0.01$) which represents the fastest growing mode predicted by the numerical model in the case of supply limited conditions ($\Delta = 0.01$, $\alpha \simeq 0.5$)

amplitude of the order of $mm$. At the end of the simulation, $10$ well-shaped dunes can be easily identified through the computational domain with an average wavelength equal to $1\ m$ which is the alluvial wavelength predicted by the linear stability analysis for the same set of parameters.

Each numerical simulation is made considering a common simulation time window which corresponds to values of the final amplitude of the dunes of the same order of those observed at the end of the flume experiments. The chosen simulation time window turns out to be of the same order of the duration of the experiments. The left part of the panels of figure 3.14 shows also the bottom profiles through an enlargement of the central part of the computational domain at different time steps for each numerical simulation. It is possible to observe the rapid decay of the perturbation components characterised by the smallest wavelengths. Only the perturbations corresponding to the unstable range of modes predicted by the linear stability analysis survive. The initial waviness (grey lines), which is generated as a sequence of random numbers, is characterised by very short wavelengths representing a physical meaningless description of the bottom. The first part of each numerical simulation can be thought as a numerical trick which allows to obtain a reasonable initial bottom configuration (dotted lines). Left part of panel A of figure 3.14 shows numerical results of the first simulation which describe the growth of the fastest growing mode predicted by the linear stability analysis slowly prevailing on the other unstable modes (black solid line). The growth of the amplitude of the dunes is exponential and it does not bare the motionless substratum.

A similar final bottom configuration is computed by the second numerical simulation (panel B), which considers a dimensional thickness of the sediment layer equal to $2\ cm$. The final amplitude of the emerging patterns at the end of the second simulation is just large enough to locally bare the motionless substratum and $10$ regularly spaced alluvial dunes can be readily identified, the average wavelength of which is equal to that of the first simulation.

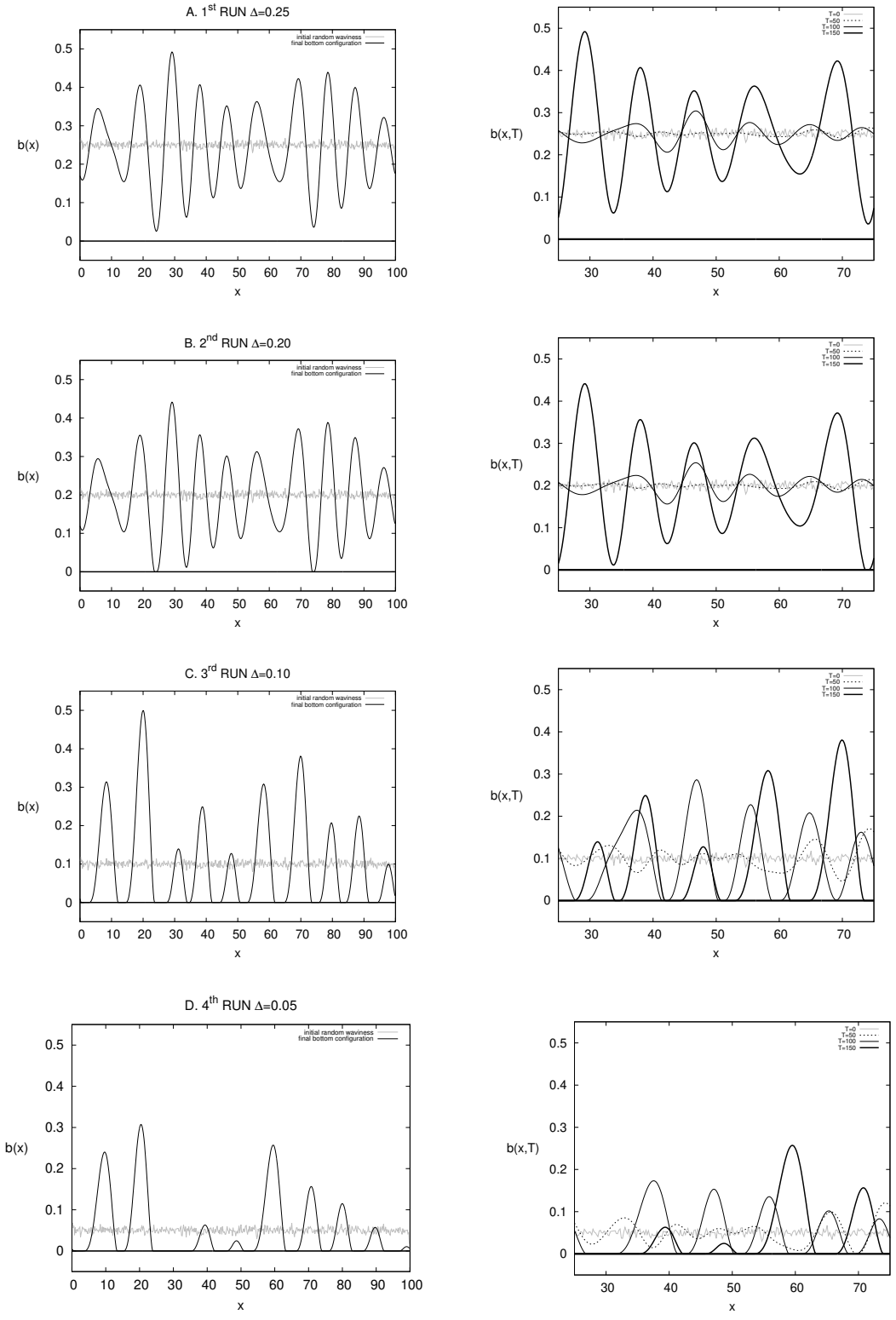


Figure 3.14: Time development of an initial random bottom waviness for the following values of the flow and sediment parameters: $\mathcal{C} = 15$, $Fr = 0.5$, $\Psi = 50°$. Left panels: Initial random waviness and final bottom configurations. Right panels: Bottom profiles at different time steps.

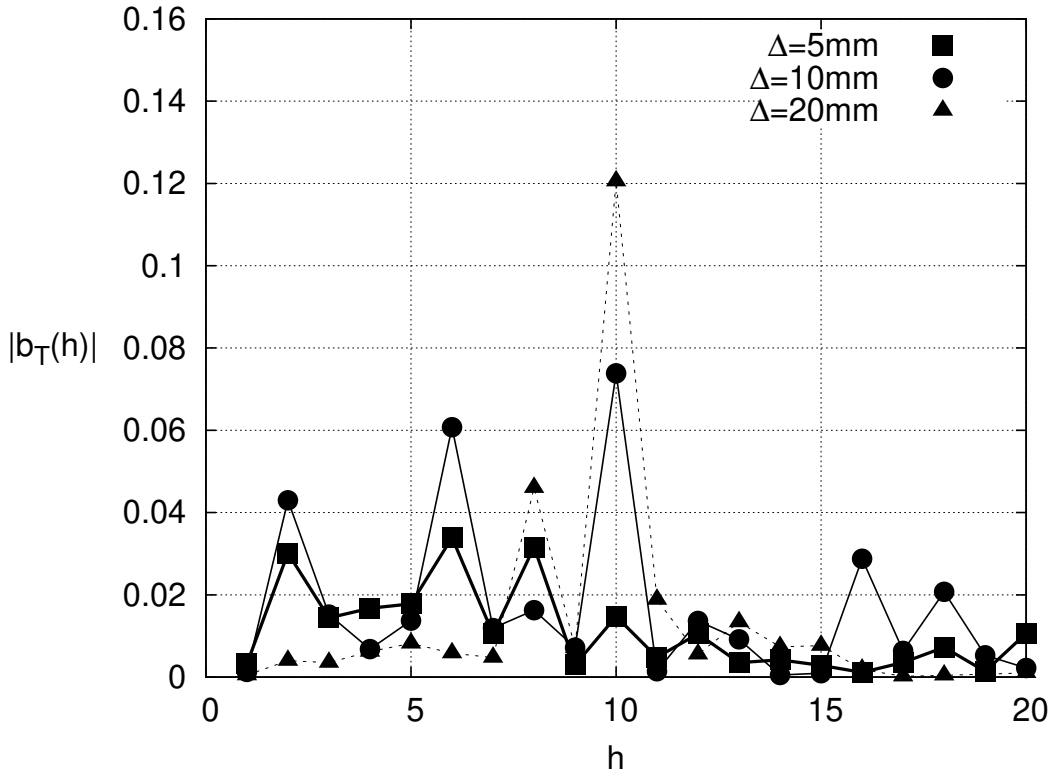


Figure 3.15: Comparison between the harmonic content of the final bottom configurations computed at the end of the numerical simulations varying the supply limitation. The modulus of the Fourier transform is plotted versus the first harmonic components.

The series includes two further simulations which correspond to an initial sand layer thickness of $1\ cm$ (panel C) and $0.5\ cm$ (panel D), respectively. For these values of the volume of mobile sediment, numerical results predict the baring of the motionless substratum owing to the formation of supply limited dunes. The final bottom configurations show an increasing crest-to-crest distance of the dunes as the initial thickness of the sand layer decreases. The lengthening of the supply limited dunes and the increasing irregularity of their profile with an increasing supply limitation is evident.

By considering the harmonic content of each final bottom configuration computed by the numerical simulations, the spectrum of the bottom profile reveals whether a dominant wavelength is present or whether the configuration is the result of a superposition of many different components. In Figure 3.15, the spectra of the final bottom configurations are compared. The modulus of the Fourier transform of each harmonic component is presented. The numerical results show that the peak harmonic component shifts towards lower frequencies as the thickness of the sand layer decreases. These numerical findings are in fair agreement with the experimental measurements presented in Chapter 2.

## 3.6 Conclusions

Numerical simulations were performed to investigate the formation of starved dunes in steady currents by means of an idealised process-based numerical model which consists of an extension of the linear stability analysis of sand dunes that accounts for the effect of sediment starvation on the formation of fluvial dunes. The main outcomes of the theoretical investigation are the following.

- Numerical simulations of the time-development of the bottom profile characterising both alluvial dunes and starved dunes, for the same values of the hydrodynamic and morphodynamic parameters and, in particular, for the same duration of the numerical simulations, predict that starved dunes attained longer wavelengths than alluvial dunes. This is consistent with the laboratory measurements presented in Chapter 2.
- A stability analysis of starved dunes in steady currents was performed in order to compare the numerical findings with the field observations by Carling et al. (2000). As the sediment starvation increases, alluvial two-dimensional dunes are replaced by more irregularly spaced starved dunes that exhibit a larger averaged crest-to-crest distance than alluvial dunes. This is consistent with the field data collected by Carling et al. (2000).

# Chapter 4

# A Numerical Investigation on the Formation of Starved Dunes in Oscillatory Tidal Currents


## Abstract

Field observations in the English Channel through the central part of the Dover Strait, where strong tidal currents prevent the uniform deposition of sediments ultimately leading to sediment starvation, show the presence of morphological patterns with geometric and kinematic characteristics that are similar to, but different from, those of typical tidal dunes. In particular, these amorphous sandy mounds exhibit an averaged spacing which is larger than the wavelength of tidal dunes that are observed in the same surveyed area where sand is abundant. The present investigation is intended to be a contribution to the stability theory of sand dunes in oscillatory tidal currents that accounts for the effect of sediment starvation on the formation of tidal dunes. When the volume of sediments available for transport is limited, classical morphodynamic stability analyses cannot be applied for two main reasons: firstly, the motionless substratum initially underlying the mobile sediments is exposed by the emergence of the bedforms and the seabed profile is no longer sinusoidal; secondly, the predictor relations commonly used to quantify sediment transport are no longer valid because of the exposition of the motionless substratum. An idealised process-based model is presented which consists of a hydrodynamic module, that is based on a perturbation approach and considers an oscillatory turbulent flow interacting with small amplitude sandy mounds, and a morphodynamic module, that is based on a numerical integration of the sediment continuity equation and accounts for the possibility of the exposition of a motionless substratum. The main outcome of the theoretical investigation is that, when the motionless substratum is exposed by the formation of tidal dunes, the lack of sand affect the sediment transport and, in turn, the dune morphology. As the motionless substratum is progressively exposed by the growth of the dunes, numerical results predict the lengthening of the sandy mounds and an increasing irregularity in their spacing. The reliability of the idealised model is supported by a comparison of the theoretical findings with the aforementioned field observations in the central part of the English Channel.

## 4.1 Introduction

As described in 1.1, marine environments exhibit a fascinating variety of bedforms, ranging from small scale ripples to large scale sand banks, and unravelling the processes underlying their appearance is a subject of great concern to coastal engineers. Sea wave ripples play an important role in sediment transport and mixing processes at the seafloor as flow separation occurs at their crests eventually inducing coherent flow structures (vortices) that increase mass and momentum transfer and sediment transport. For practical purposes, the effect that these small-scale bedforms have on large-scale phenomena can be modelled by assimilating their presence as a hydraulic roughness of appropriate size. Differently, tidal banks evolve on very much larger spatial and temporal scales than ripples, and understanding their long-term dynamics is fundamental for the proper design of offshore structures and human interventions (such as dredging activities) with special attention to the consequences that both structures and interventions may have on the surrounding environment. Even more important from a practical point of view is the very dynamic behaviour of tidal dune fields widespread over the continental shelf, that should be regularly monitored in order to safeguard submarine pipelines and cables whose safety can be compromised by their migration.

The present theoretical investigation on the formation of starved dunes in oscillatory tidal flows is based on the field observations of Le Bot et al. (2000), Le Bot (2001), Le Bot and Trentesaux (2004), which were carried out in the English Channel through the central part of the Calis-Dover Strait at the southern end of the 'South Falls' and 'Sandettie' banks. The presence of these huge converging sand deposits has a strong influence on the sediment availability through the surveyed area. In the northern part of the area, sediment is abundant as a result of the erosion in progress of the 'South Falls' (Smith and Rijkswaterstaat, 1988), whereas, in the southern part, tidal currents accelerate as a consequence of banks' convergence so as to prevent a uniform deposition of sediment leading ultimately to local sediment starvation. Two morphologically contrasted sectors were identified by Le Bot (2001), namely the North-West and the South-East sector. In the former, a underlying motionless substratum is entirely covered by a uniform mixture of sand with mean grain size equal to $0.35$ mm and very regular tidal dunes were observed that exhibit typical features of an environment rich of sand. The rate and direction of the migration of these bedforms vary depending on the time-scale of the field observations showing a strong correlation with the wind regime and the occurrence of sea storms. Conversely, in the South-East sector, a bimodal mixture of fine gravel and sand (mean grain size equal to $0.35$ mm) is transported by tidal currents in the form of periodic sandy mounds with finite extent in the transverse direction interspersed with exposed pebble lags that exhibit geometric and kinematic characteristics different from tidal dunes of the North-West sector. In this sector, the sequence of mounds migrate invariably towards the South-West, which is the direction of the tidal ebb that here dominates with respect to the tidal flood. In particular, the in-situ measurements indicate that the crest-to-crest distance of tidal dunes in the North-West sector is smaller than the mound-to-mound distance of starved bedforms in the South-East sector (see Figure 4.1). As the hydrodynamic parameters and the characteristics of the mobile sediment of the two sectors are similar, a possible explanation for the existing differences between tidal dunes and sandy mounds is the effect of sediment starvation on the morphology of tidal dunes.

The objective of the present study is to provide a detailed description of the flow field generated by the interaction of an oscillatory tidal current with periodic sandy mounds superimposed on pebble lags and to explain the mechanisms that lead to their appearance.

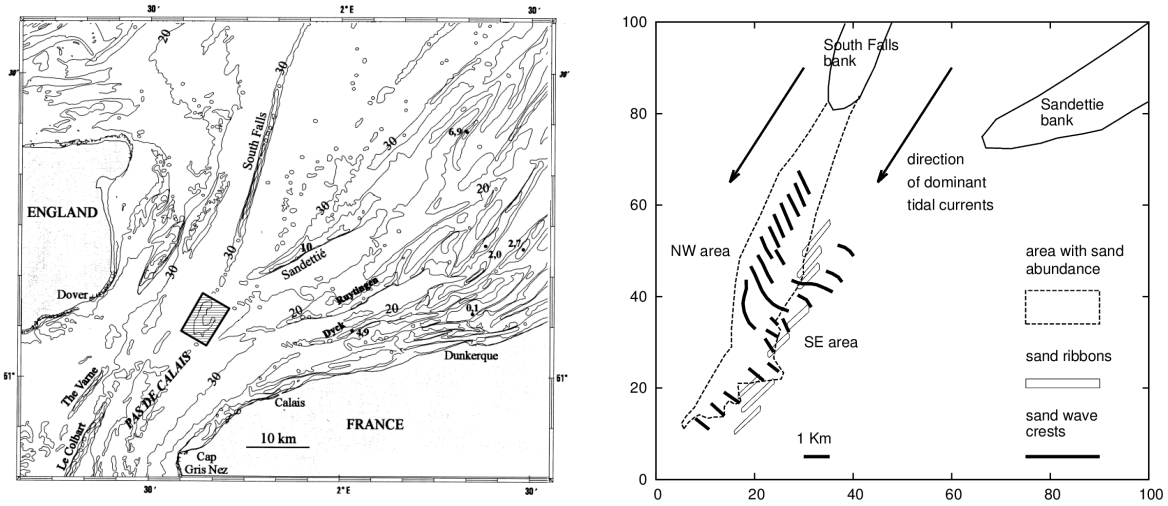


Figure 4.1: Left panel: Location of the field observation of Le Bot & Trentesaux (2004). The dashed rectangle represents the surveyed area. Right Panel: Sketch of the measured crests of tidal dunes and sandy mounds. The broken line encloses the part of the surveyed area where mobile sediment is abundant. Outside this part, sediment starvation leads to the exposition of relict pebble lags. Adapted from Le Bot (2001).

Since previous models of the formation of tidal dunes explain their appearance as a result of steady recirculating flows which continually drag sediments towards the crest of the bedforms Hulscher (1996), at the first stage of the modelling, attention is focused on the steady stream that is generated by the harmonic interaction of an oscillatory tidal flow with a sequence of periodic sandy mounds. Then, directly from the knowledge of the steady velocity components, the bottom shear stress is determined, along with the net sediment transport rate. Finally, an idealised process-based model of the formation of starved dunes in oscillatory tidal currents is presented. The linear stability analysis by Besio et al. (2006) is extended to account for the effect of sediment starvation on the formation of tidal dunes by including the numerical procedure outlined by Blondeaux et al. (2016), who investigated the formation of starved ripples under surface-gravity waves when only a thin layer of mobile sediments cover a motionless substratum. Presently, the approach of Blondeaux et al. (2016) is employed to quantify sediment transport wherever the growth of the sand dunes leads to the exposition of a motionless substratum that represents the pebble lags. However, the present investigation differs from that of Blondeaux et al. (2016) because the oscillatory tidal flow is inherently turbulent and thus vorticity pervades the whole water column.

The next section is devoted to the description of the idealised process-based model of the formation of starved dunes in tidal currents. Hydrodynamic results of the model are presented in Section 4.3 in terms of the steady recirculating stream and the related net sediment transport that leads to the accretion of sandy mounds interacting with oscillatory tidal currents. Furthermore, model results on the linear stability analysis of starved tidal dunes are compared with those obtained by means of standard models devised for environments with sediment abundance. Section 4.4 is then devoted to the discussion of the application of the model to the site in the English Channel where the measurements of Le Bot and Trentesaux (2004) are available. The conclusions are drawn in the final section.

## 4.2 The model

Taking advantage of the assumption that the mixture of water and sediment flowing in the vicinity of the bottom is sufficiently dilute, its average concentration is presently neglect with respect to the concentration of the packed particles resting at the bottom and the hydrodynamics of the oscillatory water flow is thought to be not affected by the presence of the sediments (one-way coupling). In addition, it is possible to demonstrate directly from the sediment continuity equation through purely dimensional arguments that the morphodynamic evolution of the liquid-solid interface evolves on a morphological time-scale which turns out to be very larger than the time-scale of the hydrodynamic response, namely the time required for the tidal wave to propagate in shallow water seas. As a physical consequence, the tidal flow adjust quasi-instantaneously to the evolution of the seafloor and, as such, accounting for perturbations of the flow field only driven by perturbations of the seafloor the morphodynamics can be decoupled from the hydrodynamics (de-coupling). As a result, the model described in the following is made up of two modules: the hydrodynamic module and the morphodynamic module. In the first subsection, the so-called basic flow field is identified as the propagation of a tidal wave over a plane rough seafloor and then an appropriate small amplitude periodic perturbation of the plane configuration is superimposed on the basic morphology in order to determine the effects that a sequence of periodic sandy mounds has on the tidal-averaged flow field. In the second subsection, the morphodynamic module of the model is described that account for the effect of sediment starvation on the time-development of the bottom configuration.

### 4.2.1 The hydrodynamic module

We consider the flow field generated by the propagation of a tidal wave over a horizontal sandy bottom and we introduce a local Cartesian coordinate system $(x^*, y^*, z^*)$ with the $x^*$-axis aligned with the direction of the tidal current, the $z^*$-axis vertical and pointing upwards and the origin at the free surface. Hereinafter a star is used to denote dimensional quantities.

Although, in the English Channel, the semi-diurnal constituent is dominant with respect to the other tidal constituents and a fair description of the tidal flow can be made just accounting for the propagation of its associated tidal wave, presently the tidal current is assumed to be generated by the superposition of the semi-diurnal (M2) with the quarter-diurnal (M4) tidal constituent and a residual current (Z0). The quarter-diurnal constituent and the residual current, are added so as to show, in the following, the effects of their harmonic interaction on the migration of tidal dunes and sandy mounds. If the amplitude of the free surface oscillations induced by the tide propagation is assumed to be much smaller than the local water depth, the velocity profile generated by the propagation of a tidal wave over a plane, horizontal bottom can be expressed as follows

$$u^*(z^*,t^*) = \left[\frac{U^*_{M2}(z^*)}{2}\exp\left(i\omega^* t^*\right) + c.c.\right] + \left[\frac{U^*_{M4}(z^*)}{2}\exp\left(2i\omega^* t^*\right) + c.c.\right] + U^*_{Z0}(z^*). \quad (4.1)$$

where $\omega^*$ is the angular frequency of the M2 tidal constituent. In (4.1), the dependence of $U^*_{M2}$, $U^*_{M4}$ and $U^*_{Z0}$ on $x^*$ is neglected because the area of interest has the size of the sandy mounds and turns out to be much smaller than the tidal wavelength. Moreover, the functions $U^*_{M2}(z^*)$, $U^*_{M4}(z^*)$, $U^*_{Z0}(z^*)$ are each independent on the other and the gradient of the free

surface, which drives the flow, is provided by

$$\frac{\partial \eta^*}{\partial x^*} = \left[\frac{1}{2}\frac{\partial H^*_{M2}}{\partial x^*}\exp\left(i\omega^*_{M2}t^*\right) + c.c.\right] + \left[\frac{1}{2}\frac{\partial H^*_{M4}}{\partial x^*}\exp\left(i\omega^*_{M4}t^*\right) + c.c.\right] + \frac{\partial H^*_{Z0}}{\partial x^*}. \tag{4.2}$$

Typically, Field measurements typically provide the local depth-averaged values $\hat{U}^*_{M4}$, $\hat{U}^*_{M2}$, $\hat{U}^*_{Z0}$ of $U^*_{M4}$, $U^*_{M2}$ and $U^*_{Z0}$, while the present hydrodynamic model requires the evaluation of the velocity profile over the vertical direction as it concerns the tidal-averaged recirculating stream throughout the water column owing to the interaction of the oscillatory tidal current with periodic bedforms. The functions $U^*_{M2}(z^*)$, $U^*_{M4}(z^*)$, $U^*_{Z0}(z^*)$ and their relationship with the free surface oscillations can be determined by considering momentum and continuity equation. Because of the high values of the Reynolds number, the flow regime turns out to be turbulent and Reynolds averaged equations should be considered for the different tide constituents

$$\frac{d}{dz^*}\left[\nu^*_T\frac{dU^*_{M2}(z^*)}{dz^*}\right] = i\omega^*_{M2}U^*_{M2}(z^*) + g^*\frac{dH^*_{M2}}{dx^*}, \tag{4.3}$$

$$\frac{d}{dz^*}\left[\nu^*_T\frac{dU^*_{M4}(z^*)}{dz^*}\right] = i\omega^*_{M4}U^*_{M4}(z^*) + g^*\frac{dH^*_{M4}}{dx^*}, \tag{4.4}$$

$$\frac{d}{dz^*}\left[\nu^*_T\frac{dU^*_{Z0}(z^*)}{dz^*}\right] = g^*\frac{dH^*_{Z0}}{dx^*}, \tag{4.5}$$

where the values of $\frac{dH^*_{M2}}{dx^*}$, $\frac{dH^*_{M4}}{dx^*}$, $\frac{dH^*_{Z0}}{dx^*}$, which are assumed to be constant, should take appropriate values to generate the required depth-averaged velocity oscillations. The determination of the velocity profiles calls for the introduction of an appropriate turbulence model. Presently, turbulence is assumed to be isotropic and thus Reynolds stresses are quantified by using Boussinesq hypothesis and by considering a self-similar solution for the kinematic eddy viscosity, denoted by $\nu^*_T$ in (4.3)-(4.5). Moreover, since turbulent stresses are much larger than viscous stresses, the kinematic viscosity of the sea water is neglected.

Some existing models assume a constant value of the eddy viscosity. A turbulence model that assumes a constant eddy viscosity provides an acceptable description of the flow field only if the no-slip condition at the bottom is replaced by a partial slip condition, but, as the fluid is thought to slip over the bottom, the large values of the velocity gradient at the bottom cannot be reliably reproduced. Because of the unsteady nature of the tidal flow, the eddy viscosity should depend also on time (Roos and Schuttelaars, 2013). However, Gerkema (2000) pointed out that a time-independent eddy viscosity fails to describe the mixing processes due to turbulence mainly at flow reversal, when the transport of any quantity, and in particular of fluid momentum, is very weak. Herein, the vertical profile of the kinematic eddy viscosity is assumed to be independent on time and reads

$$\nu^*_T(z^*) = \kappa\frac{\hat{U}^*_{M2}h^*_0}{\mathcal{C}}F(\xi); \quad \text{with} \quad \xi = \frac{z^*-\eta^*}{h^*_0+\eta^*}, \tag{4.6}$$

where $\kappa$ is the von Karman constant ($\kappa = 0.4$) and $h^*_0$ is the average water depth.

In (4.6) the eddy viscosity is assumed to be proportional to the amplitude of the friction velocity induced by the semi-diurnal tidal constituent, which is evaluated by means of the friction factor $\mathcal{C}$. Since the Reynolds number of the tidal flow is typically very large, the

friction factor $\mathcal{C}$ is assumed to depend only on the dimensionless roughness $z_r = z_r^*/h_0^*$ and is evaluated by means of the standard relationship proposed by Fredsøe and Deigaard (1992)

$$\mathcal{C} = 5.75 \log_{10} \left( \frac{10.9 h_0^*}{z_r^*} \right). \tag{4.7}$$

In the present model, the eddy viscosity profile proposed by Dean (1974) is employed. The resulting eddy viscosity has a finite value at the free surface that increases down through the water column reaching its maximum value and then progressively decreases until it finally vanishes at the sea bottom. The function $F(\xi)$ in (4.6) provides the spatial dependence of the eddy viscosity and reads

$$F(\xi) = \frac{-\xi(1+\xi)}{1 + 2A(1+\xi)^2 + 3B(1+\xi)^3} \quad \text{with} \quad A = 1.84 \ , \quad B = -1.56 \tag{4.8}$$

It follows that the eddy viscosity can be written in the form

$$\nu_T^* (z^*) = \nu_{T0}^* \nu_T (\xi) \tag{4.9}$$

where

$$\nu_{T0}^* = \frac{\kappa U_{M2}^* h_0^*}{\mathcal{C}} \int_{-1}^{0} F(\xi)\, d\xi \quad \text{and} \quad \nu_T (\xi) = \frac{F(\xi)}{\int_{-1}^{0} F(\xi)\, d\xi}.$$

and, of course, the depth-averaged value of $\nu_T (\xi)$ is equal to 1.

Assuming that the sea bottom is hydrodynamically rough, the no-slip condition impose the vanishing of the velocity at a distance from the sea bottom equal to $z_r^*/29.8$ and, assuming that no wind stress acts on the free surface, the vanishing of the velocity gradient should be enforced at the free surface. Equations (4.3)-(4.5) are then numerically integrated by means of a standard shooting procedure similar to those outlined by Blondeaux and Vittori (2005). Firstly, a particular solution of the equation system (4.3)-(4.5) is obtained by forcing a unitary value of the forcing term and imposing vanishing values of the velocity and its derivative at the free surface. Secondly, another particular solution is determined by forcing vanishing values of both the velocity derivative and the forcing term but assuming a unitary value of the velocity at the free surface. Finally, a solution of the equations (4.3)-(4.5) is obtained that satisfies the no-slip condition at the bottom and that attains the desired value of the depth averaged velocity by simply linearly combining the two aforementioned solutions.

The numerical integration is carried out with a standard second-order Runge-Kutta method that makes use of a coordinate stretching to increase the number of grid points close to the bottom, where the velocity gradients attain their larger values. Numerical preliminary tests with successive grid refinements allow the evaluation of the minimum number of grid points that assures the accuracy of the numerical results.

Now, let us consider the interaction of the tidal current with a periodic sequence of sandy mounds, with a spatial periodicity $L^*$. The crests of the bottom forms are assumed to be orthogonal to the direction of the tidal current and interspersed by flat areas made up of relict pebble lags. Considering a spatially periodic flow domain of extent $L^*$ in the $x^*$ direction, the bottom profile can be modelled as (see figure 4.2):

$$\begin{aligned} z^* &= -h_0^* - \Delta^* && \text{for} \quad 0 < x^* < \frac{L^* - \lambda^*}{2} \quad \text{and} \quad \frac{L^* + \lambda^*}{2} < x^* < L^* \\ z^* &= -h_0^* - \Delta^* + a^* \mathcal{F}(x^*) && \text{for} \quad \frac{L^* - \lambda^*}{2} \le x \le \frac{L^* + \lambda^*}{2} \end{aligned} \tag{4.10}$$

where $L^*, \lambda^*$ and $\Delta^*$ are free parameters. Moreover, in (4.10) $\mathcal{F}(x^*)$ indicates a function that describes the bottom profile at the considered time and assumes values of order one. At this stage the exact form of $\mathcal{F}(x^*)$ is not relevant. In the model, similarly to Roos et al. (2005), a Fourier decomposition of (4.10) is used, which allows any bottom profile to be considered. Presently, to discuss the influence of sandy mounds on the tidal current only, we consider:

$$\mathcal{F}(x^*) = \left[1 + \cos\left(\frac{2\pi\,(x^* - L^*/2)}{\lambda^*}\right)\right],$$

which is a fair approximation of the profile of the sandy mounds.

Since the sequence of sandy mounds is thought to be generated by the time development of a thin layer of sand of thickness $\Delta^*$ superimposed to a rigid substratum and $L^*$ denotes the crest-to-crest distance of the sandy mounds, the conservation of the volume of sand forces $a^*$ to be equal to $\Delta^* L^*/\lambda^*$.

At this stage it is convenient to introduce the following dimensionless variables:

$$(x, z) = \frac{(x^*, z^*)}{h_0^*} \quad , \quad t = t^*\omega^* \quad , \quad (u, w) = \frac{(u^*, w^*)}{\hat{U}_{M2}^*} \quad , \quad p = \frac{p^*}{\rho^*\omega^* h_0^* \hat{U}_{M2}^*}, \tag{4.11}$$

where $\rho^*$ is the density of the sea water, $p^*$ is pressure and $(u^*, w^*)$ are the velocity components along the $x^*, z^*$-axes, respectively.

The dimensionless continuity and momentum equations, read:

$$\frac{\partial u}{\partial x} + \frac{\partial w}{\partial z} = 0 \tag{4.12}$$

$$\frac{1}{\hat{r}}\frac{\partial u}{\partial t} + u\frac{\partial u}{\partial x} + w\frac{\partial u}{\partial z} = -\frac{1}{\hat{r}}\frac{\partial P}{\partial x} - \frac{1}{Fr^2}\frac{\partial \eta}{\partial x} + \hat{\mathcal{D}}\left\{\frac{\partial}{\partial x}\left[2\nu_T\frac{\partial u}{\partial x}\right] + \frac{\partial}{\partial z}\left[\nu_T\left(\frac{\partial u}{\partial z} + \frac{\partial w}{\partial x}\right)\right]\right\} \tag{4.13}$$

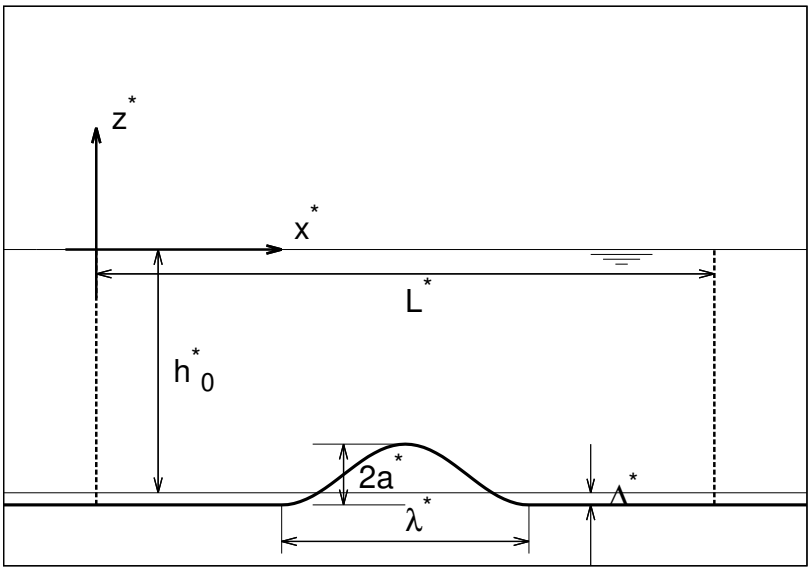


Figure 4.2: Sketch of the bottom profile

$$\frac{1}{\hat{r}}\frac{\partial w}{\partial t}+u\frac{\partial w}{\partial x}+w\frac{\partial w}{\partial z}=-\frac{1}{\hat{r}}\frac{\partial P}{\partial z}+\hat{\mathcal{D}}\left\{\frac{\partial}{\partial x}\left[\nu_T\left(\frac{\partial u}{\partial z}+\frac{\partial w}{\partial x}\right)\right]+\frac{\partial}{\partial z}\left[2\nu_T\frac{\partial w}{\partial z}\right]\right\} \tag{4.14}$$

where the modified pressure $P$

$$P=p+\frac{g^*}{\hat{U}^*_{M2}\omega^*}\left(z-\eta\right) \tag{4.15}$$

is introduced. Presently the eddy viscosity is modelled as in Besio et al. (2006) by using the friction factor $\mathcal{C}$ and the function $F\left(\xi\right)$, that describes the vertical distribution. In (4.13)-(4.14), the following dimensionless parameters appear:

$$\hat{r}=\frac{\hat{U}^*_{M2}}{\omega^* h^*_0}\,,\quad \hat{\mathcal{D}}=\frac{k\int_{-1}^{0}F(\xi)d\xi}{\mathcal{C}},\quad Fr=\frac{\hat{U}^*_{M2}}{\sqrt{g^* h^*_0}}. \tag{4.16}$$

The parameter $\hat{r}$ is proportional to the ratio between the amplitude of horizontal fluid displacement oscillations and the local water depth. A rough estimate shows that $\hat{r}$ is of order $10^2$ and $\hat{\mathcal{D}}$ and $Fr$ are of order $10^{-2}$.

The hydrodynamic problem is closed by the kinematic and dynamic boundary conditions at the free surface and at the bottom. At the free surface ($z=\eta(x,y,t)$), the dynamic boundary condition forces the vanishing of the stress (the stress related to the wind is not considered). At the bottom, the velocity should vanish at $z=-h+z_r/29.8$ (Fredsøe and Deigaard, 1992). Finally, the kinematic boundary condition at the free surface should be imposed.

The local water depth, which can be easily derived from (4.10), can be expressed as the superposition of different spatial harmonic components

$$h(x)=1+\epsilon\sum_{n=1}^{N}\left(h_n e^{i\alpha_n x}+c.c.\right) \tag{4.17}$$

where $\epsilon$ is a measure of the ratio between the amplitude of the bottom forms and the local water depth. As long as the hydrodynamic problem is considered, the assumption of a rigid bottom is more than reasonable since the morphodynamic time scale $T^*_m$, which will be introduced in the next section, is typically much longer than the tide period. For example, considering values of the physical quantities typical of the English Channel (e.g. a water depth equal to $30$ m, a sediment size equal $0.35$ mm, $\rho^*_s/\rho^*$ equal to $2.65$ and the bed porosity $p_{or}$ equal to $0.4$), $T^*_m$ turns out to be of order $10^3$ days. In other words the interaction of the tidal current with the bottom forms can be studied by neglecting the small variations of the bottom profile taking place during the tidal period. The value of $N$ is chosen, on the basis of numerical experiments, to be sufficiently large to obtain an accurate description of the bottom profile both at the early and at the final stages of the bottom development.

The assumption that $\epsilon$ is much smaller than $1$ allows the solution of the hydrodynamic problem to be obtained by means of a perturbation approach and to be written in the form:

$$[u,w,P,\eta]=\left[u_0,0,0,\frac{a^*}{h^*_0}e_0\right]+\epsilon\left[\sum_{n=1}^{N}\left(u_1^{(n)},w_1^{(n)},\hat{r}P_1^{(n)},0\right)h_n e^{i\alpha_n x}+c.c.\right]+O(\epsilon^2) \tag{4.18}$$

The eddy viscosity ($\nu_T$) is expressed as:

$$\nu_T=\nu_{T0}+\epsilon\sum_{n=1}^{N}\left(\nu_{T1}^{(n)}h_n e^{i\alpha_n x}+c.c.\right)+O(\epsilon^2) \tag{4.19}$$

The functions $\nu_{T0}$ and $\nu_{T1}^{(n)}$ can be easily computed by expanding the formulae in Appendix A, where $\xi = (z^* - \eta^*)/(h^* + \eta^*)$ (note that in the definition of $\xi$, $h_0^*$ is replaced by $h^*$). The quantities $u_0$, $e_0$ and $\nu_{T0}$ are related to the flow field generated by a tidal wave propagating over a horizontal bottom and are computed following Besio et al. (2006).

When (4.18) is substituted into (4.12)-(4.14) and only the terms of order $\epsilon$ are considered, the following system of linear differential equations for $u_1^{(n)}, w_1^{(n)}, P_1^{(n)}$ is obtained:

$$i\alpha_n u_1^{(n)} + \frac{\partial w_1^{(n)}}{\partial z} = 0 \tag{4.20}$$

$$\begin{aligned}\frac{1}{\hat{r}}\frac{\partial u_1^{(n)}}{\partial t} + i\alpha_n u_0 u_1^{(n)} + w_1^{(n)}\frac{\partial u_0}{\partial z} &= -i\alpha_n P_1^{(n)} \\ &+\hat{\mathcal{D}}\left[\nu_{T0}\left(\frac{\partial^2 u_1^{(n)}}{\partial z^2} - \alpha_n^2 u_1^{(n)}\right) + \frac{\partial \nu_{T0}}{\partial z}\left(\frac{\partial u_1^{(n)}}{\partial z} + i\alpha_n w_1^{(n)}\right) + \nu_{T1}^{(n)}\frac{\partial^2 u_0}{\partial z^2} + \frac{\partial \nu_{T1}^{(n)}}{\partial z}\frac{\partial u_0}{\partial z}\right]\end{aligned} \tag{4.21}$$

$$\begin{aligned}\frac{1}{\hat{r}}\frac{\partial w_1^{(n)}}{\partial t} + i\alpha_n u_0 w_1^{(n)} &= -\frac{\partial P_1^{(n)}}{\partial z} \\ &+\hat{\mathcal{D}}\left[\nu_{T0}\left(\frac{\partial^2 w_1^{(n)}}{\partial z^2} - \alpha_n^2 w_1^{(n)}\right) + i\nu_{T1}^{(n)}\alpha_n\frac{\partial u_0}{\partial z} + 2\frac{\partial \nu_{T0}}{\partial z}\frac{\partial w_1^{(n)}}{\partial z}\right].\end{aligned} \tag{4.22}$$

The no-slip condition at the bottom and the vanishing of the stress at the free surface provide the boundary condition at order $\epsilon$:

$$u_1^{(n)} = -\frac{\partial u_0}{\partial z} \quad , \quad w_1^{(n)} = 0 \ \text{ at } \ z = -h + \frac{z_r}{29.8} \tag{4.23}$$

$$\frac{\partial u_1^{(n)}}{\partial z} = 0 \quad , \quad 2\hat{\mathcal{D}}\nu_{T0}\frac{\partial w_1^{(n)}}{\partial z} = 0 \quad \text{at } \ z = 0 \tag{4.24}$$

Since the parameter $\hat{r}$ assumes values of $O(10^2)$, the terms proportional to the local time derivatives can be neglected in (4.13)-(4.14) and $t$ becomes just a parameter. It is worth pointing out that the terms in (4.13)-(4.14) proportional to $\hat{\mathcal{D}}$ should be retained, notwithstanding the small value of $\hat{\mathcal{D}}$, since they become significant in a boundary layer close to the bottom because of the larger values the velocity gradient. Indeed, their presence is necessary to force the no-slip condition at the bottom.

### 4.2.2 The morphodynamic module

The sediments at the sea bottom are moved by the currents induced by tide propagation and by the sea waves. Qualitative information on the amount and direction of the sediment moved by the tidal currents can be obtained by evaluating the bottom shear stress while quantitative results can be obtained only by using a sediment transport predictor.

In relatively large water depths, such as the ones presently considered, sea waves induce significant sediment transport only during strong storms, i.e. for a small number of days per year. Hence, the effect of sea waves is not presently taken into account and only the effects of tidal currents are considered. Le Bot and Trentesaux (2004) showed that the suspended-load provides a significant contribution, in particularly during spring tidal conditions. Therefore, both the bed load and the suspended load are taken into account by the model.

Bed load ($q_B^*$) is obtained by means of Van Rijn (1991) formula:

$$q_B = \frac{q_B^*}{\sqrt{\left(\frac{\rho_s^*}{\rho^*} - 1\right) g^* (d^*)^3}} = \frac{0.25}{R_p^{0.2}} \left(\frac{\theta - \theta_{crit}}{\theta_{crit}}\right)^{1.5} \sqrt{\theta}, \tag{4.25}$$

where $d^*$ is the mean grain size of the mobile sediment and $\theta = \frac{\widetilde{\tau}_x^*}{(\rho_s^* - \rho^*) g^* d^*}$ is the Shields parameter ($\widetilde{\tau}_x^*$ is the bottom shear stress related to the skin friction only).

In (4.25) the critical value of the Shields parameter ($\theta_{crit}$) is evaluated using Brownlie (1981) formula and $R_p$ is the Reynolds number of the sediment:

$$R_p = \frac{\sqrt{(\rho_s^*/\rho^* - 1) g^* d^{*3}}}{\nu^*}. \tag{4.26}$$

Following Colombini (2004), the bottom shear stress is evaluated at the top of the bed-load layer, the thickness $h_b^*$ of which is proportional either to the grain size $d^*$ or to the roughness size $z_r^*$ (if ripples are present). Experimental data show that the proportionality constant $l_b$, necessary to compute $h_b^*$, depends on the bed shear stress (e.g. Sekine & Kikkawa, 1992)

$$l_b = 1 + 1.3 \left(\frac{\theta - \theta_{crit}}{\theta_{crit}}\right)^{0.55}. \tag{4.27}$$

To account for the effects of the bottom slope, we follow Seminara (1998) and add the following contribution to the sediment transport rate

$$q_P = \frac{q_P^*}{\sqrt{\left(\frac{\rho_s^*}{\rho^*} - 1\right) g^* (d^*)^3}} = -q_B G \frac{\partial h}{\partial x} \tag{4.28}$$

where $G$ is a dimensionless constant which is evaluated following Seminara (1998) and Talmon et al. (1995)

$$G = -\frac{1}{\mu_d} \frac{\theta_{crit}}{q_B} \frac{dq_B}{d\theta} \tag{4.29}$$

In (4.29), $\mu_d$ is the dynamic friction coefficient of the sediment which assumes values close to $0.5\mu_s$ (Fredsøe and Deigaard, 1992), $\mu_s$ being the static friction coefficient.

The suspended sediment transport rate $q_S$ is evaluated as the flux of the sediment concentration $c = c(x^*, z^*, t^*)$. The temporal and spatial distribution of $c$ is obtained by solving the

standard convection-diffusion equation where the diffusion coefficient of sediment particles is assumed to be equal to the eddy viscosity (Van Rijn, 1991).

Because of the assumption $\epsilon \ll 1$, the concentration of the suspended sediment can be written in the form:

$$c = c_0 + \epsilon c_1 = c_0 + \epsilon \sum_{n=1}^{N} \left( c_1^{(n)} h_n e^{i\alpha_n x} + c.c. \right) + O(\epsilon^2). \tag{4.30}$$

When (4.30) is substituted into sediment concentration equation, at the leading order of approximation, the following equation is obtained:

$$\frac{1}{\hat{r}} \frac{\partial c_0}{\partial t} - \frac{w_s}{\hat{r}\sqrt{\hat{\psi}_d}} \frac{\partial c_0}{\partial z} = \hat{\mathcal{D}} \frac{\partial}{\partial z} \left( \nu_T \frac{\partial c_0}{\partial z} \right) \tag{4.31}$$

where the sediment mobility number $\hat{\psi}_d$ is defined by

$$\hat{\psi}_d = \frac{\omega^* h_0^*}{\left( \frac{\rho_s^*}{\rho^*} - 1 \right) g^* d^*}.$$

Equation (4.31) is solved by means of the numerical procedure previously described, after neglecting the terms proportional to $1/\hat{r}$ and expanding the function $c_0$ as a Fourier series of time because of the time dependence forced by the bottom boundary condition (4.34).

Then, the contribution of $c_1$ in equation (4.30) is determined by solving the following differential equation:

$$\left[ i\alpha_x u_0 c_1 + w_1 \frac{\partial c_0}{\partial_z} \right] - \frac{w_s}{\hat{r}\sqrt{\hat{\psi}_d}} \frac{\partial c_1}{\partial z} = \tag{4.32}$$

$$\hat{\mathcal{D}} \left[ \nu_{T0} \left( \frac{\partial^2 c_1}{\partial z^2} - \alpha_x^2 c_1 \right) + \frac{\partial \nu_{T0}}{\partial z} \left( \frac{\partial c_1}{\partial z} \right) + \nu_{T1} \frac{\partial^2 c_0}{\partial z^2} + \frac{\partial \nu_{T1}}{\partial z} \frac{\partial c_0}{\partial z} \right]$$

Once more, the solution of (4.32) is obtained with the numerical procedure previously outlined. The boundary conditions at the free surface for equations (4.31) and (4.32), require the vanishing of the sediment flux in the direction normal-to-surface ($\hat{n}$)

$$(\nu_T^* \nabla c + w_s^* c \hat{k}) \cdot \hat{n} = 0, \tag{4.33}$$

where $\hat{k}$ is the unit vector in the vertical direction. Since, in the case under consideration, the bottom roughness is certainly much smaller than $0.01 h_0^*$, the sediment concentration is forced equal to the reference concentration $c_{\zeta^*}$ at $\zeta^* = 0.01 h^*$ (Van Rijn, 1984):

$$c_{\zeta^*} = 0.015 \frac{d^*}{\zeta^* R_p^{0.2}} \left( \frac{\theta - \theta_{crit}}{\theta_{crit}} \right)^{3/2}. \tag{4.34}$$

The relationships (4.33) and (4.34) should be expanded in terms of the small parameter $\epsilon$, in order to obtain the boundary conditions for $c_0$ and $c_1$.

Once the spatial and temporal distribution of the sediment concentration is obtained, the transport rate of sediment in suspension ($q_S^*$) is evaluated as the flux of sediment concentration:

$$q_S = \frac{q_S^*}{\sqrt{\left( \frac{\rho_s^*}{\rho^*} - 1 \right) g^* (d^*)^3}} = \frac{\hat{r}\sqrt{\hat{\psi}_d} h_0^*}{d^*} \int_{-h+\zeta}^{\eta} uc \, dz. \tag{4.35}$$

Relationships (4.25), (4.28) and (4.35) provide the different components of the sediment transport if there is an unlimited supply of sand at the sea bottom. On the other hand, if a small amount of sediment is available and the rigid substratum of the sea bottom becomes exposed, no sediment can be mobilised at the considered location and the sediment transport depends on the upstream values, i.e. on the spatial derivative of the bottom shear stress.

Following Blondeaux et al. (2016), let us consider position $x_P$, where no sand is available and a time interval during which the bottom shear stress is positive and the Shields parameter $\theta(x,t)$ is larger than its critical value. If $\partial\theta(x,t)/\partial x$ is positive, i.e. the bottom shear stress increases as $x$ is increased, the sediment transport rate cannot increase because no further sediment is available. Hence, the sediment transport rate at $x_P$ should be equal to the sediment transport rate at the upstream location. On the other hand, if $\partial\theta(x)/\partial x$ is negative at $x_P$, i.e. the bottom shear stress decreases as $x$ is increased, two situations are possible. If the upstream value of the sediment transport $q$ is smaller than that computed at $x_P$, because also the region upstream is exposed of sediment, the sediment transport rate at $x_P$ should be taken equal to the upstream value. If, on the other hand, the upstream value of the sediment transport rate is larger than that computed at $x_P$, the local sediment transport rate at $x_P$ is that provided by the sediment transport predictor at $x_P$ and some sand is deposited on the bottom.

Finally, in order to evaluate the bottom time development, it is necessary to consider the sediment balance equation averaged over the tide period

$$\frac{\partial h}{\partial t_m} = -\frac{\partial \overline{q}_T}{\partial x} = -\frac{\partial\left(\overline{q}_B + \overline{q}_P + \overline{q}_S\right)}{\partial x} \quad \text{with} \quad t_m = \frac{t^*}{T_m^*} \tag{4.36}$$

where

$$\left(\overline{q}_B, \overline{q}_T, \overline{q}_S\right) = \frac{1}{2\pi}\int_0^{2\pi} \left(q_B, q_P, q_S\right) dt.$$

The morphodynamic time scale $T_m^*$ appearing in (4.36) is defined by:

$$T_m^* = \frac{(1-p_{or})h_0^{*2}}{\sqrt{\left(\rho_s^*/\rho^* - 1\right) g^* \left(d^*\right)^3}}, \tag{4.37}$$

and turns out to be much longer than the period of the tide $T^*$, since typical values of $T_m^*$ are of the order of months. Of course equation (4.36), that can be applied only in the regions where the bottom is covered with sediment and the bottom profile can change, is integrated in time by means of a second order Runge-Kutta scheme and the spatial derivatives are approximated by means of centred finite differences.

## 4.3 Results

### 4.3.1 Flow field and sediment transport over sand waves and sandy mounds

An oscillatory flow close to a wavy bottom generates steady recirculating cells, the form and strength of which depend on the flow parameters and on the wavelength and amplitude of the bottom waviness. The steady streaming which is generated by the oscillatory flow over ripples was studied by Vittori (1989); Blondeaux (1990); Hara and Mei (1990). Considering larger spatial and temporal scales, also an oscillating tidal current over sand waves or sandy mounds causes the formation of steady recirculating cells (Hulscher, 1996, Besio et al., 2006). An exhaustive investigation of the phenomenon in the parameter space is not possible because of the large number of governing parameters so that, in the following, only the effects of some of these parameters are shown.

The steady recirculating cells which form over a sequence of sand waves, for values of the parameters typical of field observations in the North Sea, is shown in Figure 4.3a, where the steady component of the stream function $\psi$ is plotted (the stream function $\psi$ is such that $u = \frac{\partial \psi}{\partial z}$ and $w = -\frac{\partial \psi}{\partial x}$). Two symmetric recirculating cells per wavelength can be observed. The left cell is characterised by negative values of $\psi$ while the right cell is characterised by positive values of $\psi$. The crest of the sand wave is located at the centre of the computational domain and two troughs are located at $x = 0$ and $x = L$. Figure 4.3 shows also the streamlines over sandy mounds (panels b to f), for assigned values of the crest-to-crest distance $L$ and of the volume of sand, i.e. for a fixed value of $\Delta$. Because of the conservation of the sand volume, the value of the height of the sandy mounds is related to the value of $\lambda$ by

$$a = \frac{L\Delta}{\lambda}. \tag{4.38}$$

The direction of the steady flow component is always toward the crest and the left and right recirculating cells are characterised by negative and positive values of $\psi$, respectively. Moreover, as the value of $\lambda$ is decreased and the amplitude of the mound is increased, the intensity of the steady velocity component increases, particularly close to the crest of the mound (see figure 4.3e,f).

The analysis of the time-averaged value of the shear stress at the bottom shows that it is always directed towards the crest both for sand waves and sandy mounds. Moreover, the value of the shear stress increases as the value of $\lambda$ is decreased and the amplitude of the bottom forms increases. Even though the analysis of the bottom shear stress could provide indications on the sediment transport rate, the time average of the bottom shear stress differs from the time average of the sediment transport rate because of the nonlinear relationship between $q_T$ and $\theta$ and because of the effects of the bottom slope on sediment dynamics. Figure 4.4 shows the time-averaged components $\overline{q}_T, \overline{q}_B, \overline{q}_P, \overline{q}_S$ of the total sediment transport rate and its different contributions, as function of $x$ for the different bottom profiles previously considered. For values of $\lambda$ just smaller than $L$, the net sediment transport rate is directed towards the crests of the mounds and the bottom forms are expected to grow. However for decreasing values of $\lambda$ and close to the crest, the total sediment transport rate reverses its direction and is directed from the crests to the troughs of the bottom forms. As a consequence, the growth of the sandy mounds is expected to stop (see figure 4.4f). The analysis of the different components of $\overline{q}_T$ in figure 4.4 shows that the component related to suspended transport is smaller than the others for all values of $\lambda$, while the component related to the effect of slope increases its intensity as $\lambda$ is decreased. For the smallest values

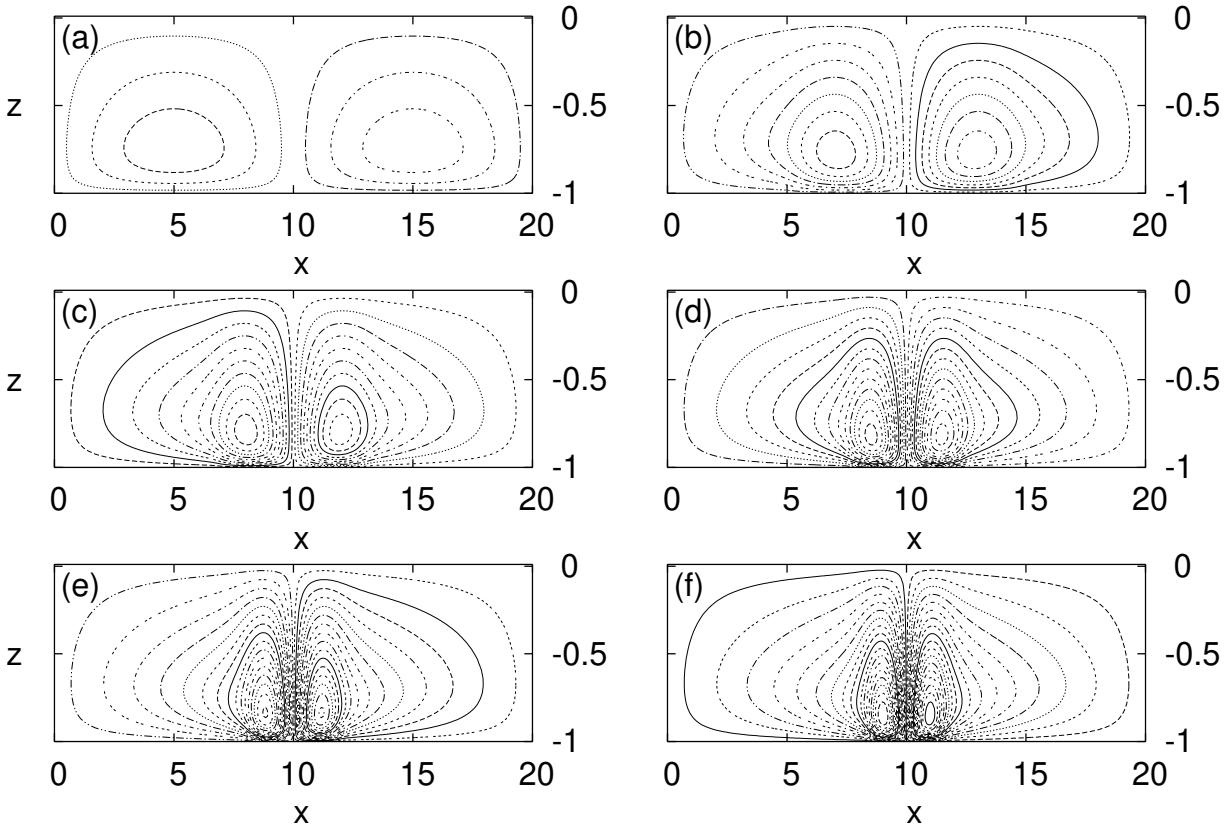


Figure 4.3: Isolines of the stream function $\psi$ describing the steady velocity component for $h_0^* = 30$ m, $\hat{U}_{M2}^* = 0.9$ m s$^{-1}$ $\hat{U}_{M4}^* = 0$ m s$^{-1}$, $\hat{Z}_0^* = 0$ m s$^{-1}$, $L^* = 600$m, $\Delta^*$=0.05 $h_0^*$, and the geometrical configuration plotted in figure 4.2. a) $\lambda = L$, $a$=0.05 (sand waves); b) $\lambda = L/2$, $a$=0.1; c) $\lambda = L/3$, $a$=0.15; d) $\lambda = L/4$, $a$=0.2; e) $\lambda = L/5$, $a$=0.25; f) $\lambda = L/6$, $a$=0.3 ($\psi_n = n\Delta\psi + 1$ with $\Delta\psi = 2$ and $n = \pm 1, \pm 2, ...$)

of $\lambda$, the sediment transport due to slope effects becomes even larger than that related to bed-load. Figure 4.4 shows oscillations of the sediment transport rate of small amplitude and wavelength, located in the regions of transition between the rigid substratum and the sandy mounds. These oscillations give rise to a sequence of very short bedforms characterised by a quite small amplitude. These small scale bedforms have no physical meaning, since they are a spurious output of the numerical approach, but their influence on the dynamics of the large scale bottom forms is negligible. Indeed the results, which can be obtained by introducing a filtering procedure which removes the small scale oscillations, are practically coincident with those obtained without the use of any filter.

Figure 4.5 shows the time averaged value of the total sediment transport rate $\overline{q}_T = \overline{q}_B + \overline{q}_P + \overline{q}_S$ both for sand waves and sandy mounds for different values of $L^*$. The steady component of the sediment transport rate is directed from the troughs towards the crests of the bottom waviness (we remind to the reader that the crest of the bottom profile is located at $x = L/2$). For sinusoidal sand waves (panel a), the maximum value of $\overline{q}_T$ is attained for a wavelength of the bottom forms falling around $35h_0^*$. Hence, the results plotted in Figure 4.5a suggest that, in a site characterised by abundance of sand and values of the parameters similar to those of figure 4.5, the sand waves are characterised by a wavelength of about $1000$

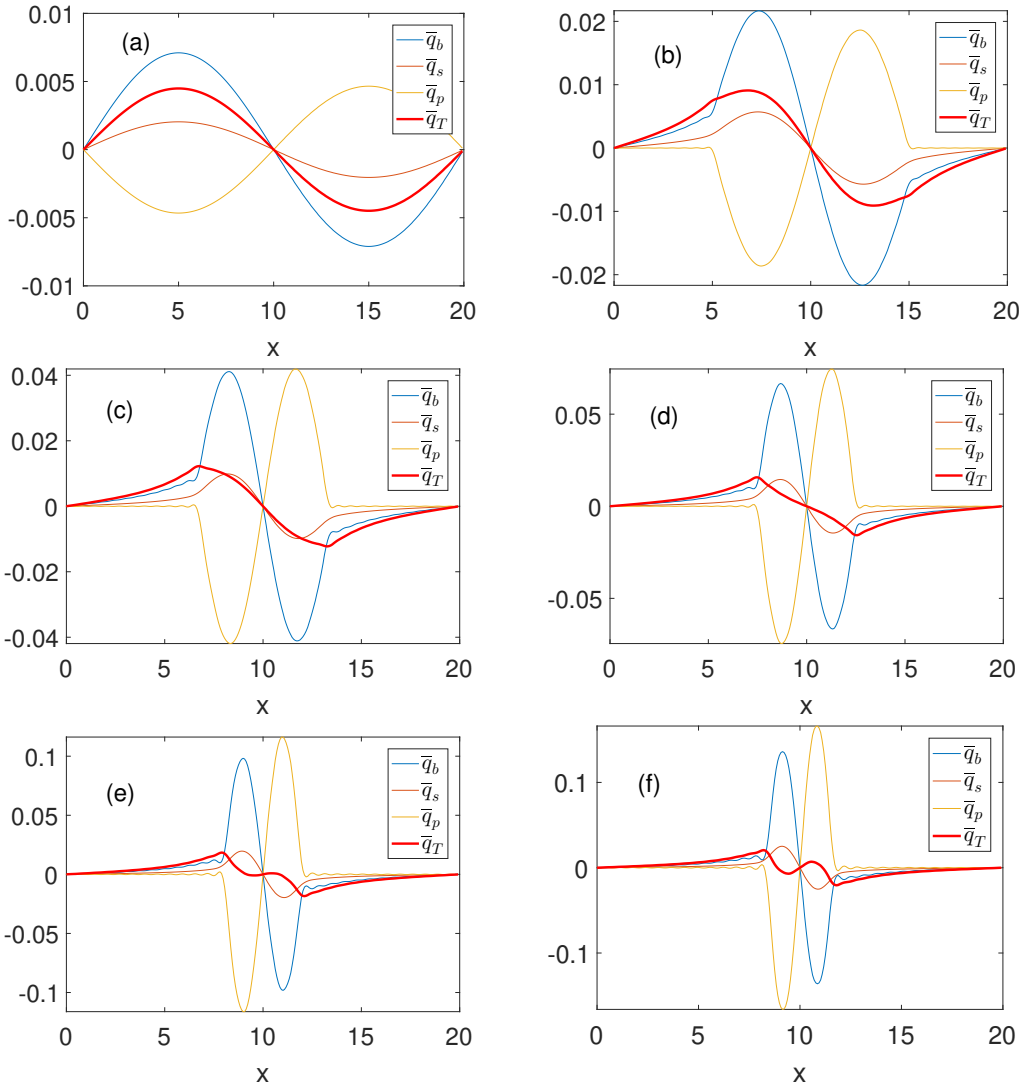


Figure 4.4: Time-averaged components of the sediment transport rate for $h_0^* = 30$ m, $\hat{U}_{M2}^* = 0.9$ ms$^{-1}$ $\hat{U}_{M4}^* = 0$ ms$^{-1}$, $\hat{Z}_0^* = 0$ ms$^{-1}$, $L^* = 600$ m, $d^* = 0.6$ mm, $\rho_s^* = 2650$ kgm$^{-3}$, $\Delta^* = 0.05\ h_0^*$, $\mu_d = 0.23$. Bottom configuration as sketched in Figure 4.2 with a) $\lambda = L$, $a = 0.05$; b) $\lambda = L/2$, $a = 0.1$; c) $\lambda = L/3$, $a = 0.15$; d) $\lambda = L/4$, $a = 0.2$; e) $\lambda = L/5$, $a = 0.25$; f) $\lambda = L/6$, $a = 0.3$.

m. If a sand mound is considered (see panel b of figure 4.5) and the values of the parameters are the same as those of panel a, the analysis of the sediment transport indicates that the mounds that will develop and which will be identified in the next section, are characterised by a larger crest-to-crest distance.

Figure 4.6 is similar to Figure 4.5 but the results are obtained for a larger value of the amplitude $\hat{U}_{M2}^*$ of the velocity oscillations induced by the semi-diurnal constituent. The results of Figure 4.6a show that stronger tidal currents lead to the formation of shorter sand waves. Indeed, by comparing the results shown in Figure 4.5a with those of Figure 4.6a, it can be seen that the wavelength of sand waves which are likely to appear decreases from 1000 m to about 720 m, as $\hat{U}_{M2}^*$ is increased from 0.7 m/s to 0.9 m/s. If sandy mounds

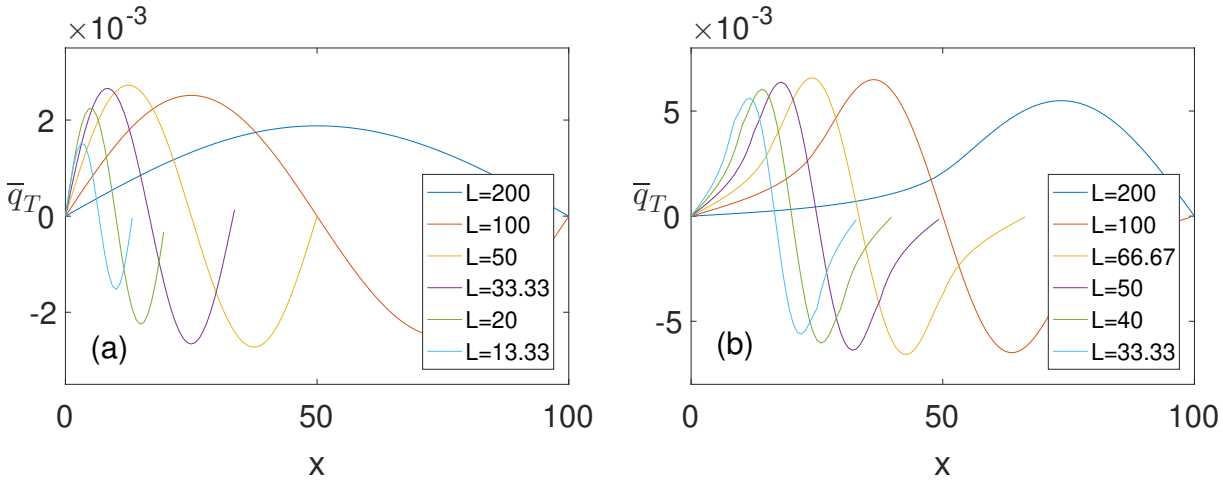


Figure 4.5: Time-averaged sediment transport rate for $h_0^* = 30$ m, $\hat{U}_{M2}^* = 0.7$ m s$^{-1}$, $\hat{U}_{M4}^* = 0$ m s$^{-1}$, $\hat{Z}_0^* = 0$ m s$^{-1}$, $d^* = 0.4$ mm, $\rho_s^* = 2650$ kg m$^{-3}$, $\Delta^* = 0.05 h_0^*$, $\mu_d = 0.26$, Panel a): sand waves ($\lambda$=$L$); panel b): sandy mounds $\lambda = L/2$.

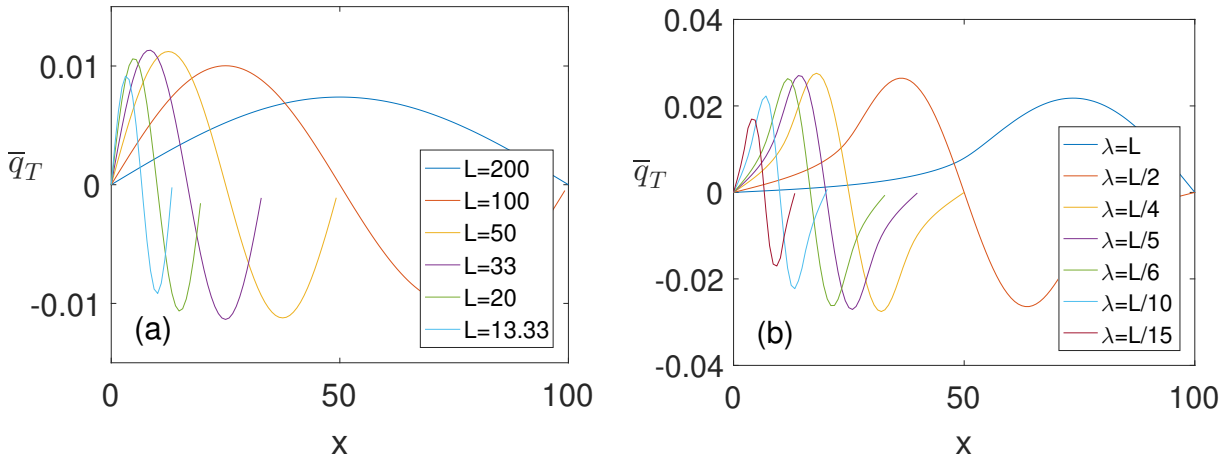


Figure 4.6: Time-averaged sediment transport rate for $h_0^* = 30$ m, $\hat{U}_{M2}^* = 0.9$ m s$^{-1}$ $\hat{U}_{M4}^* = 0$ m s$^{-1}$, $\hat{Z}_0^* = 0$ m s$^{-1}$, $d^* = 0.4$ mm, $\rho_s^* = 2650$ kg m$^{-3}$, $\mu_d = 0.26$, $\Delta = 0.05$. Panel a): sinusoidal bottom profile ($L$=$\lambda$); panel b): geometrical configuration plotted in figure 4.2 with different values of $\lambda$.

are considered, no qualitative difference is found as $\hat{U}_{M2}^*$ is varied (Figure 4.5b and 4.6b). Further results obtained for different values of the water depth and of the grain size show that the crest-to-crest distance of the sandy mounds is always longer than the wavelength of the sand waves. In other words the bedforms, which appear when only a thin layer of sand is available and the bedform development bares the rigid substratum, are longer than those which are generated by tidal currents flowing over a layer of sand of “infinite” thickness.

### 4.3.2 Formation of sand waves and sandy mounds

The analysis of the steady recirculating cells and of the net sediment transport rate provides qualitative information on the evolution of the sea bottom. However, quantitative results can be obtained only by using the morphodynamic module and by considering the time development of the bottom profile. In the present section, we describe the results of a series of numerical simulations of the formation of sand waves and sandy mounds. The values of the parameters used in the simulations are reported in Table 4.1.

Figure 4.7 shows the time development of the sea bottom when an infinite layer of sediment is present and the initial profile of the sea bottom is $A_0 \cos(\alpha x)$, with $A_0$ equal to 0.005 $h_0^*$ (Case A1 in Table 4.1). At the early stages of formation of sand waves, linear effects dominate and, in accordance to the theory by Besio et al. (2006), the growth of the amplitude of the bottom waviness is exponential.

Figure 4.8 shows the time development of the initial bottom perturbation considered previously, when the sea bottom is covered with a layer of sand of dimensionless thickness $\Delta = 0.01$. As the initial disturbance grows, at $t = 60$ (i.e after about 10 tidal cycles), the sea bottom becomes exposed of sediment in large regions and nonlinear effects start to play a significant role. The crests of the bottom forms become sharper than the troughs, which in turn are flat because of the presence of the rigid substratum. Moreover, because of the symmetry of the forcing flow, the bottom profile is symmetric with respect to the crests and troughs and no migration of the bedforms is observed.

If a residual current is present, the bottom forms migrate in the direction of the residual current, as found by Németh et al. (2002). Moreover, the bottom profile at equilibrium is no longer sinusoidal and symmetric with respect to the central crest but it is characterised by larger slopes of the forward flanks (Figure 4.9).

When an infinite amount of sand is available and for values of the parameters such that the sea bottom is unstable, the wavelength of the sand waves that tend to appear can be predicted by means of stability-based models as those of Hulscher (1996) or Besio et al. (2006). Such models show that, during the early stages of formation, when nonlinear effects are weak, the growth of the amplitude of the sand waves that takes place on the slow morphodynamic time scale $T_m^*$ (see (4.37)) is exponential and can be quantified by its growth rate $\Gamma$. As the aforementioned models, the present model allows computation of the growth rate of sand waves following the procedure outlined below. We perform numerical simulations of

| case | $h_0^*$ [m] | $\Delta^*$ [m] | $\omega^*$ [sec$^{-1}$] | $\hat{U}_{M2}^*$ [m/s] | $\hat{U}_{M4}^*$ [m/s] | $\hat{Z}_0^*$ [m/s] | $d^*$ [m $\times 10^{-3}$] | $L^*$ [m] |
|---|---|---|---|---|---|---|---|---|
| A1 | 30 | $\infty$ | $7.5 \times 10^{-5}$ | 0.7 | 0. | 0. | 0.4 | 546 |
| A2 | 30 | 0.3 | $7.5 \times 10^{-5}$ | 0.7 | 0. | 0. | 0.4 | 546 |
| A3 | 30 | 0.3 | $7.5 \times 10^{-5}$ | 0.7 | 0. | 0.1 | 0.4 | 546 |
| B0a | 30 | $\infty$ | $7.5 \times 10^{-5}$ | 0.8 | 0. | 0. | 0.35 | 355 |
| B0b | 30 | 0.6 | $7.5 \times 10^{-5}$ | 0.8 | 0. | 0. | 0.35 | 415 |
| B1a | 30 | 0.6 | $7.5 \times 10^{-5}$ | 0.8 | 0. | 0.05 | 0.35 | 375 |
| B1b | 30 | 0.6 | $7.5 \times 10^{-5}$ | 0.8 | 0. | 0.1 | 0.35 | 375 |
| B2 | 30 | 0.6 | $7.5 \times 10^{-5}$ | 0.8 | 0.15 | 0.05 | 0.35 | 375 |

Table 4.1: Data used in the cases discussed.

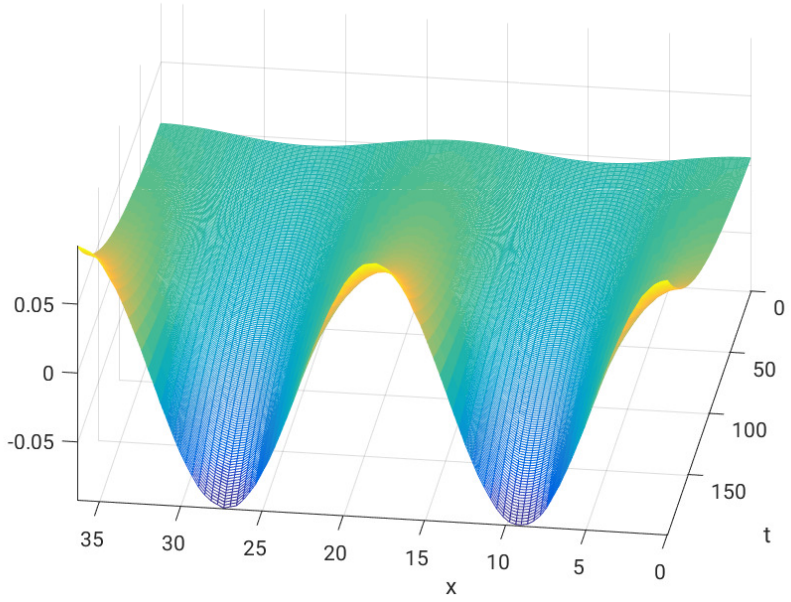


Figure 4.7: Time development of sandy mounds within a sand layer of average thickness $\Delta = 0.01$ starting from a sinusoidal undulation of the bottom surface with a dimensionless initial amplitude equal to 0.005 (Case A2, Table 4.1).

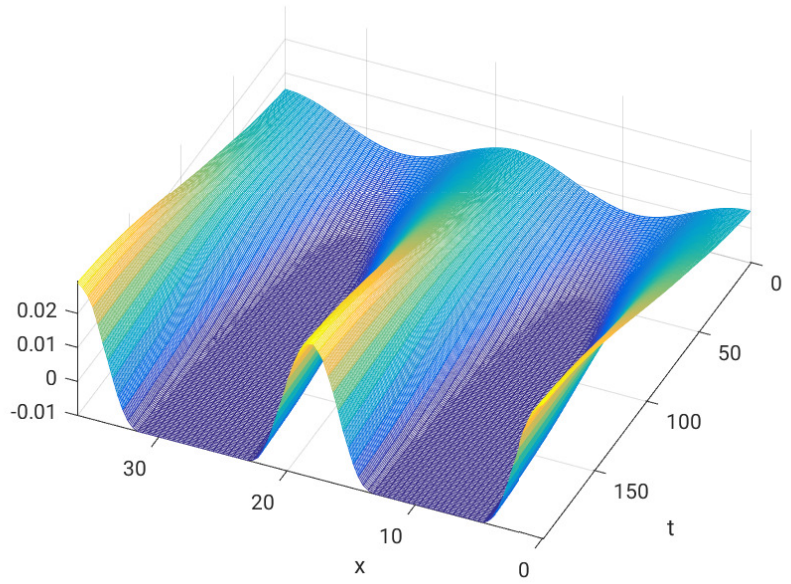


Figure 4.8: Time development of sandy mounds within a sand layer of average thickness $\Delta = 0.01$ starting from a sinusoidal undulation of the bottom surface with a dimensionless initial amplitude equal to 0.005 (Case A2, Table 4.1).

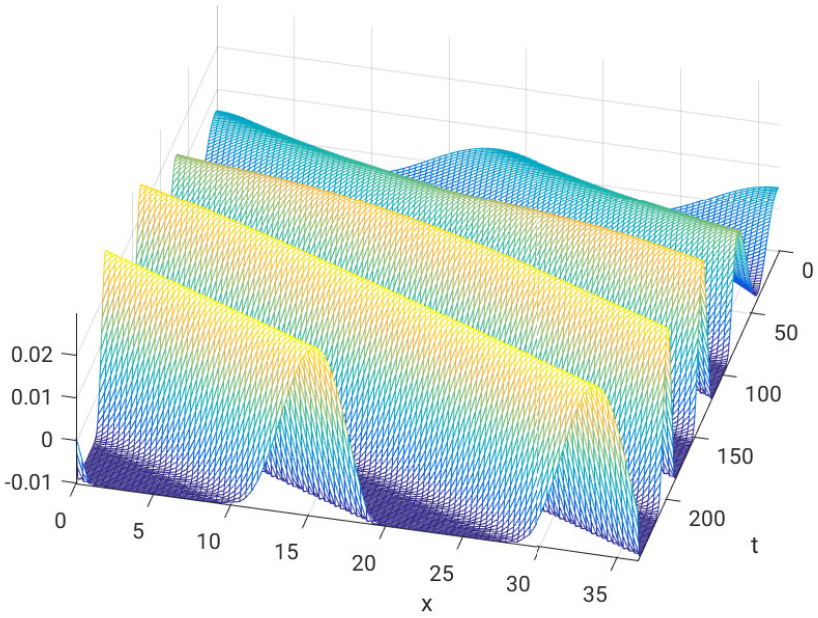


Figure 4.9: Time development of sandy mounds within a sand layer of average thickness $\Delta = 0.01$ starting from a sinusoidal undulation of the bottom surface with a dimensionless initial amplitude equal to 0.005 (Case A3, Table 4.1).

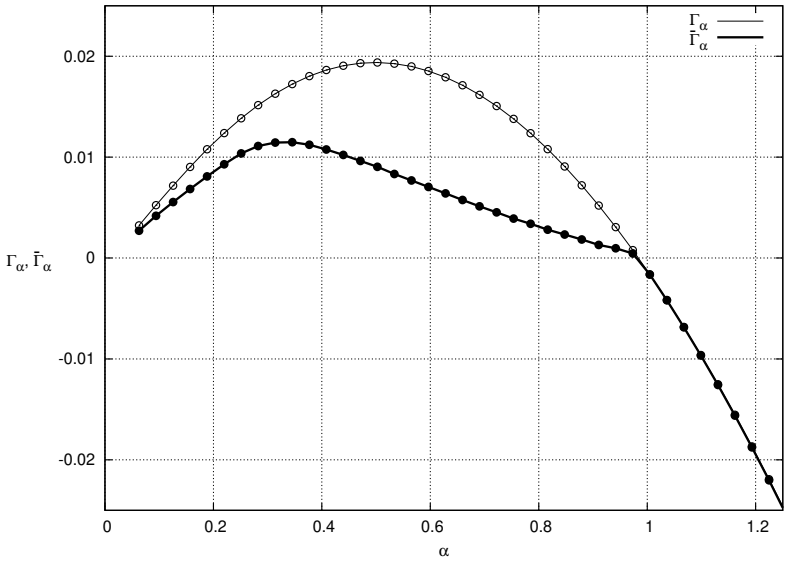


Figure 4.10: Analytic growth rate evaluated by standard stability analysis (thin line), numerical growth rate $\Gamma_\alpha$ for an 'infinite' sand layer (white dots) and quantity $\hat{\Gamma}_\alpha$ for an initial sand layer thickness $\Delta$ equal to $0.05$ (black dots) versus the perturbation wavenumber $\alpha$ for $h_0^* = 30$ m, $\hat{U}_{M2}^* = 0.8$ m s$^{-1}$ $\hat{U}_{M4}^* = 0$ m s$^{-1}$, $\hat{Z}_0^* = 0$ m s$^{-1}$, $d^* = 0.35$ mm, $\mu_d = 0.21$.

the bottom time development starting from initial bottom configurations described as

$$h = 1 - A_0 \cos(\alpha x)$$

and compute the growth rate of the sinusoidal undulation $\Gamma_\alpha$ as

$$\Gamma_\alpha = \frac{\ln\left[A(T_{m,fin})/A_0\right]}{T_{m,fin}}, \tag{4.39}$$

where $A(T_{m,fin})$ indicates the amplitude of the sand wave computed at $t = T_{m,fin}$. If sand waves develop, the growth of an initial disturbance for small values of $T_{m,fin}$ is exponential and the computed value of $\Gamma_\alpha$ matches the growth rate obtained by using the stability-based model by Besio et al. (2006). Figure 4.10 shows the growth rate $\Gamma_\alpha$ as function of the wavenumber $\alpha = \frac{2\pi}{L}$ of the initial bottom undulation for values of the parameters chosen to reproduce typical conditions in the North Sea, so as to compare the values of the growth rate $\Gamma_\alpha$ computed analytically by the stability analysis by Besio et al. (2006) (thin solid line) with those computed numerically by means of the present model (white dots). The numerical and the analytic results are coincident. The growth curves predicted by the models show a maximum value for $\alpha \simeq 0.47$, that is the wavenumber featuring the fastest growing sand wave which is more likely to occur. The predicted fastest growing mode corresponds to a dimensional wavelength of about $400$ m, a value in the range of the wavelengths of the very regular sand waves observed in the field by Le Bot and Trentesaux (2004).

On the other hand, if a sand layer of finite thickness $\Delta$ is considered and the emergence of sand waves exposes a motionless substratum, nonlinear effects modify the exponential growth of the bedforms. In this case, to quantify the growth of the sandy mounds and to have information on the bottom perturbation which grows most quickly, the following quantity is employed

$$\bar{\Gamma}_\alpha = \frac{\ln\left[A(T_{m,fin})/\Delta\right]}{T_{m,fin}}, \tag{4.40}$$

where the initial profile is described by:

$$h = 1 - \Delta \cos(\alpha x).$$

Because of the nonlinearity of the sediment transport predictor, the value of $\hat{\Gamma}_\alpha$ depends on the duration $T_{m,fin}$ of the numerical simulation, that has to be chosen appropriately. As $T_{m,fin}$ decreases indeed, $\hat{\Gamma}_\alpha$ approaches the values predicted by the linear stability analysis. Presently the value of $T_{m,fin}$ is chosen in such a way that $A(T_{m,fin})/\Delta$ is equal to 1.5, where $A(t)$ is half the height of the bedforms (the vertical distance from the crests to the rigid substratum). Smaller/larger values of the ratio $A(T_{m,fin})/\Delta$ lead to larger/smaller values of $\hat{\Gamma}_\alpha$. For this reason, the numerical results presented in the following provide only an indication of the effects that a motionless substratum has on the growth of sandy mounds but they cannot be used for quantitative forecasting of bedform features. The thick solid line with black dots in Figure 4.10 shows values of $\hat{\Gamma}_\alpha$ computed for a dimensionless sand layer thickness $\Delta^*$ equal to $0.05$ and different values of the parameter $L$ ($\alpha = 2\pi/L$), the other parameters being equal to the 'infinite thickness' case. The maximum growth rate is observed for $\alpha \simeq 0.37$, corresponding to a dimensional crest-to-crest distance of about $510$ m, which is similar to the mound distance observed by Le Bot and Trentesaux (2004).

## 4.4 Discussion of the results

In the previous section we showed that the evolution of an initial disturbance in a sand-starved environment generates bedforms, named sandy mounds, with a wavelength larger than that of the sand waves that develop for the same conditions but in presence of abundant sediments.

At this stage it is worthwhile pointing out that, while the wavelength of sand waves can be predicted by using a linear stability analysis assuming that the bedforms are generated by the time development of the fastest growing mode, the present model can only compute the time development of an initial bottom profile considering the nonlinear effects due to the sediment transport predictor. In order to use the present model for predictive purposes, it would be necessary to run a large number of simulations with random initial topographies setting a computational domain of very large extent (in principle, the length of the computational domain should be much larger than the wavelength of the expected equilibrium bedforms). However, such a procedure is highly demanding in terms of computational resources and, for this reason, is not presently pursued.

On the other hand, we compute the time development of initially sinusoidal bottom perturbations characterised by different wavelength and we assume that the sandy mounds are generated by the growth of the perturbation that has the largest value of $\hat{\Gamma}_\alpha$. Despite the aforementioned limitation, the model reproduces field observations fairly well. In particular, we use the model to make quantitative predictions of the characteristics of the sandy mounds observed in the English Channel by Le Bot and Trentesaux (2004). It is worth keeping in mind that the idealised model introduces some simplifications (such as constant water depth, uniform grain size, currents due to a few tidal constituents only) and only a rough agreement between the characteristics of the bedforms observed in the field and those predicted by the model is expected.

Field observations show that a reasonable value of the water depth is $30$ m and the hydrodynamics of the channel is dominated by semi-diurnal tidal currents. Moreover the eccentricity of the tidal ellipse is very low, the currents being almost rectilinear because of the geometrical constraints. The tidal current can therefore be assumed unidirectional and dominated by the M2 constituent. The intensity of the currents in the channel increases moving towards the Calais-Dover strait, where it attains its maximum values which are larger than $1$ m/s at the sea surface during mean spring tides (SHOM, 1968). However, taking into account that: 1) field data collected in the North Sea (along the Dutch coast) indicate that the amplitude of the velocity oscillations induced by the M2-constituent is roughly equal to $50\%$ of the maximum value of the current observed during the spring tide; 2) the measurements of the tidal current reported by Le Bot and Trentesaux (2004) were carried out $1$ m above the bottom, while the model requires the depth-averaged value of the velocity, all in all, a value of $\hat{U}^*_{M2}$ equal to $0.8$ m/s appears reasonable.

Field data indicate as well that the grain size distribution is characterised by significant variations in the area of the field surveys. At locations where the sand completely covers the pebble lags, the mean grain size is about $0.35$ mm (Le Bot and Trentesaux, 2004), while at the other locations, where the pebble lags are exposed, larger values of the mean grain size are found. Hence, we run the model with a mean grain size of the mobile layer of sand equal to $0.35$ mm and we consider the pebble lags as a rigid substratum.

The last model input, which is required by the model, is the thickness of the layer of sand ($\Delta^*$), which initially covers the rigid substratum. From the sections of the bottom forms

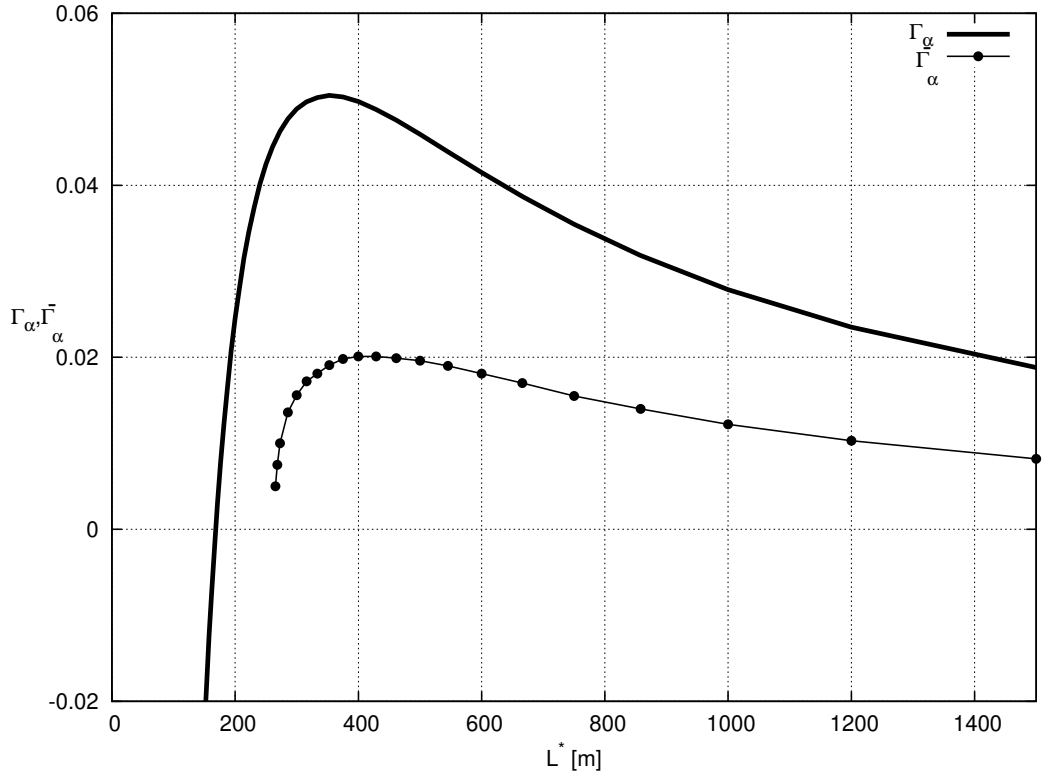


Figure 4.11: Growth rate $\Gamma_\alpha$ and $\hat{\Gamma}_\alpha$ plotted versus the dimensional crest-to-crest distance of the bottom forms for $h_0^* = 30$ m, $\hat{U}_{M2}^* = 0.8$ m s$^{-1}$ $\hat{U}_{M4}^* = 0$ m s$^{-1}$, $\hat{Z}_0^* = 0$ m s$^{-1}$, $d^* = 0.35$ mm, $\rho_s^* = 2650$ kg m$^{-3}$, $\mu_d = 0.29$, considering respectively a layer of sand of 'infinite' thickness (solid thick line) and of finite thickness $\Delta^*$ equal to $0.6$ m (solid line with dots).

shown in Le Bot and Trentesaux (2004), considering their relative distance and assuming the conservation of the volume of sand, it is possible to estimate that $\Delta^*$ is close to $0.6$ m. Table 4.1 contains the values of the parameters for cases B0a and B0b, which respectively refer to the values chosen to represent sectors A and B (Le Bot and Trentesaux, 2004).

Figure 4.11 shows the growth rate $\Gamma_\alpha$ of bottom forms over a substratum of 'infinite' thickness (solid thick line, Case B0a in Table 4.1) and the quantity $\hat{\Gamma}_\alpha$ computed for a sand layer of thickness equal to $0.6$ m (Case B0b in Table 4.1). In order to allow an easier interpretation of the results shown in figure 4.11, $\Gamma_\alpha$ and $\hat{\Gamma}_\alpha$ are plotted versus the dimensional crest-to-crest distance $L^*$. The results show that the wavelength of the sand waves predicted by the model, that is the fastest growing mode, is about $355$ m, a value which fairly agrees with the wavelength of the bedforms observed by Le Bot and Trentesaux (2004) in Sector A where the sand is abundant. Their data, collected during the field survey carried out in 1996 and represented in Figure $9$ of Le Bot and Trentesaux (2004), show that the fairly regular wavelength of the sand waves is about 300 m. On the other hand, the crest-to-crest distance of the sandy mounds predicted by the model turns out to be about $415$ m, a value which is larger than the wavelength of the sand waves and again it is in fair agreement with the field observations carried out in Sector B where the crest-to-crest distance of the observed bedforms appears to have an average value of about $425$ m. However, it is worth pointing

out that field values change over time. For example, in 1998 further sand waves appeared in Sector A and their average wavelength significantly decreased. Hence, the comparison between model predictions and field measurements should be considered more qualitative than quantitative.

Since both $U^*_{Z0}$ and $U^*_{M4}$ are set equal to zero in the model run, the bottom forms do not migrate. The migration of the bedforms observed in the field is induced by the asymmetry of the forcing flow. This tidal asymmetry can be enforced by accounting for a residual current or the superposition of diverse tidal constituents in suitable phase with the semi-diurnal one. The model accounts for the presence of both the residual current and the M4 constituent. However, the data contained in the paper by Le Bot and Trentesaux (2004) do not allow an accurate estimate of these constituents. Moreover, the field measurements clearly show that the migration of the bottom forms is certainly affected also by other effects, such as the velocity profile induced by the wind action, which are not considered in the present idealised model.

To provide information on the migration speed of the sandy mounds, the effects of the residual current and of the M4 constituent are investigated using $U^*_{M4}$ and $Z^*_0$ as free parameters. Panels $a$ and $b$ of Figure 4.12 respectively shows the effect of adding a steady current with a depth averaged velocity equal to $5$ cm s$^{-1}$ and $10$ cm s$^{-1}$ (Case B1a and B1b in Table 4.1), to the base, starved case (Case B0b in Table 4.1). As expected, the bottom forms move in the direction of the steady current and larger values of $U^*_{Z0}$ lead to larger migration speeds. Once the equilibrium conditions are attained, a migration of the bottom forms in the direction of the residual current (the positive direction) takes place and the migration speed of the bedforms is about $16$ m year$^{-1}$ for $Z^*_0 = 5$ cm/s and $32$ m year$^{-1}$ for $Z^*_0 = 10$ cm/s, that are values falling close to the measurements carried out by Le Bot and Trentesaux (2004).

Field surveys show that at some locations the direction of migration of the bedforms depends on the observation period. The current due to the wind action or the presence of more tidal constituents are possible explanations of these field observations. Figure 4.13 shows the effect of adding a M4 tidal constituent with $U^*_{M4} = 15$ cm s$^{-1}$ to the case characterised by $U^*_{M2} = 0.8$ m s$^{-1}$ and $Z^*_0 = 5$ cm s$^{-1}$. The results show that the $U^*_{M4}$ constituent can cause the migration of the bottom forms in the direction which is opposite to that of the residual current. Of course the effect of the $U^*_{M4}$ constituent depends of its phase. In figure 4.13 the phase $\varphi$ is such that the maximum value of the tidal current is in the negative direction even if the time averaged value of the tidal constituent is positive and equal to $5$ cm s$^{-1}$. If the phase is set equal to $\varphi + \pi$, the other parameters being fixed, the bedforms not only reverse the direction of migration but their migration speed increases.

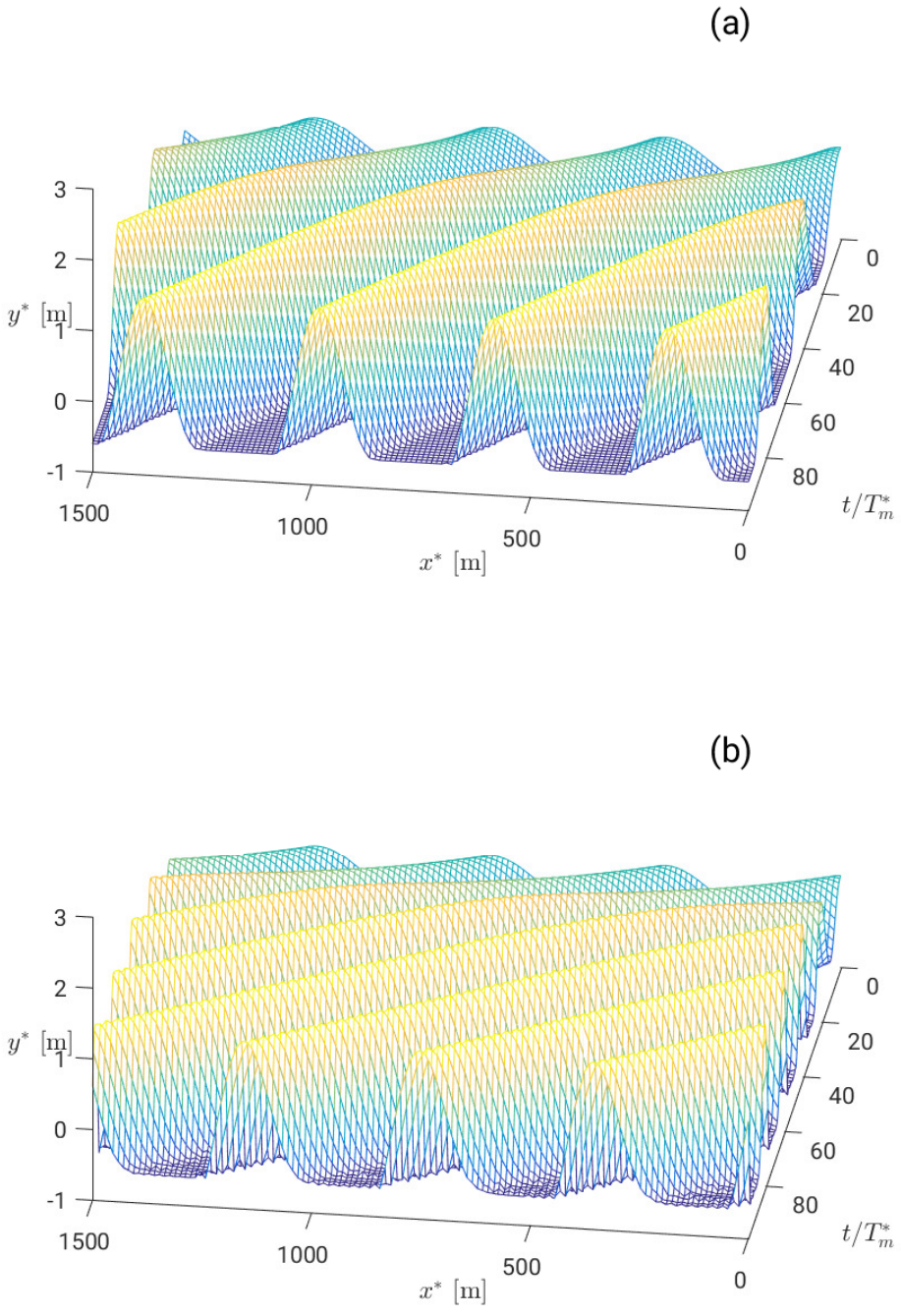


Figure 4.12: Time development of the bottom starting from a sinusoidal bottom perturbation with an initial amplitude equal to 30 cm until an equilibrium amplitude is attained for a) Case B1a and b) Case B1b (see Table 4.1).

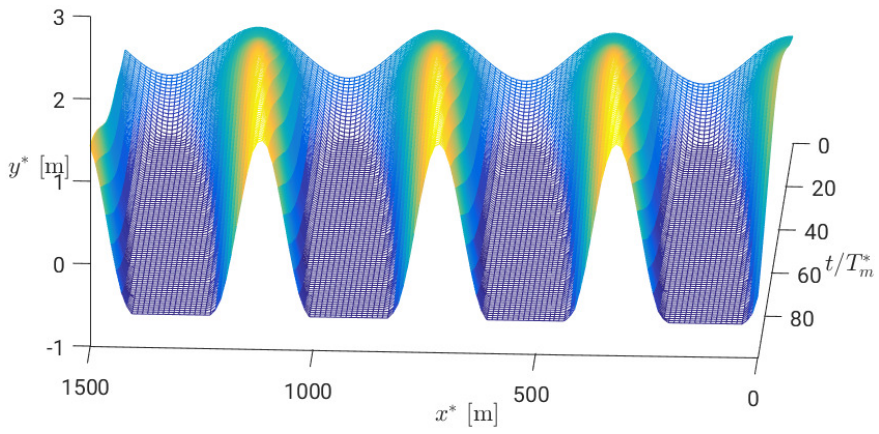


Figure 4.13: Time development of the bottom starting from a sinusoidal bottom perturbation of initial amplitude equal to $30$ cm until an equilibrium amplitude is attained for case B2 (see Table 4.1)

.

## 4.5 Conclusions

Numerical simulations were performed to investigate the formation of starved dunes in oscillatory tidal currents by means of an idealised process-based numerical model which consists of an extension of the linear stability analysis of sand dunes that accounts for the effect of sediment starvation on the formation of tidal dunes. The main outcome of the theoretical investigation are the following.

- Model predictions of the tidal averaged flow field generated by an oscillatory tidal current interacting with a sequence of isolated sandy mounds show that steady recirculating cells form as a result of the harmonic interaction of the forcing flow with the seabed and that this steady stream strongly depends on the geometry of the bed profile.
- Numerical simulations of the time-development of the bottom profile characterising both tidal dunes and sandy mounds, for the same values of the hydrodynamic and morphodynamic parameters, predict that starved sandy mounds attain longer wavelengths than tidal dunes. This is consistent with the field data collected by Le Bot (2001).
- When the symmetry of the flow due to the semi-diurnal tidal constituent is broken by accounting for the presence of more tidal constituents, the migration of sandy mounds is predicted by the model. If only a residual current is added to the semi-diurnal tidal constituent, mound migration takes place in the direction of this residual current, whereas if a quarter-diurnal tidal constituent is further included, the mounds can migrate even in the opposite direction depending on the phase shift between the different tidal constituents. A comparison of these theoretical results with the field data collected by Le Bot and Trentesaux (2004) supports the reliability of the idealised model in predicting the migration of the sandy mounds observed in the English Channel.

# Chapter 5

# Conclusions and Future Developments

## 5.1 Conclusions

The objectives of this thesis were as follows: (1) to get insights into the effects of sediment starvation on the formation of subaqueous sand dunes, (2) to describe the phenomenon by means of an experimental investigation, (3) to formulate a theory capable of including sediment starvation in the framework of the stability theory of sand dunes by numerical means, and (4) to implement and validate a numerical model capable of predicting the formation of fluvial dunes and tidal dunes wherever sediment starvation affects the dynamics of these morphological patterns. This section is devoted to answering the research questions posed in the Introduction (Section 1.4) that were formulated to achieve the above listed objectives.

**Q1.** What is known about the effect of sediment starvation on the formation of sand dunes?

The literature study has revealed that the available knowledge comes mostly from field observations and also from laboratory experiments. However, available data on this topic is limited and an apparent contradiction exists in the literature between laboratory measurements and field surveys. Therefore, how sediment starvation potentially affects the formation of sand dunes is still an unresolved issue. Furthermore, according to the examined literature, existing modelling efforts on the formation of subaqueous sand dunes usually consider an infinite availability of mobile sediment and, as such, they cannot predict the formation of subaqueous starved dunes.

**Q2.** Can the effect of sediment starvation on sand dune formation (Q1) be reproduced by laboratory experiments that simulate the appearance of fluvial dunes in steady currents, and how do the experimental findings then compare to the outcome of previous laboratory and field observations?

As shown in Chapter 2, the initial stage of sand dune formation has been successfully reproduced in a laboratory flume. A set of laboratory experiments has been presented that investigate the relationship between dune morphology and sediment starvation. Laboratory measurements indicate that the exposition of the rigid bottom of the flume strongly affects the characteristics of starved dunes, the average spacing of which increases and becomes more irregular with a decreasing sediment availability.

**Q3.** Can the effect of sediment starvation on sand dune formation (Q1) be reproduced by an idealised process-based model, and how do the model results compare to the results of the laboratory experiments (Q2)?

As shown in Chapter 3, the initial stage of fluvial dune formation has been successfully reproduced by means of an idealised process-based model that accounts for the effects of sediment starvation. The theoretical investigation assumes that the dunes are of small amplitude so as to linearise the hydrodynamic problem. However, even though the dunes are characterised by small amplitudes, their dynamics turns out to be highly nonlinear when the motionless substratum is exposed as a result of sediment starvation. Indeed, the sediment transport predictor should take into account that no sediment can be further mobilised when even high shear stresses act on the motionless substratum. Both the model results and the experimental observations show that the dunes, which are generated by a uniform steady current over a layer of sand so thin that the appearance of the morphological patterns bares an underlying motionless substratum, are longer than those which are generated for the same hydrodynamic conditions when the thickness of the sediment layer is so thick that the underlying motionless substratum is always covered by the sand. The lengthening of fluvial dunes predicted by the idealised model showed good agreement with field data on starved dunes observed through a sediment starved reach of the Rhine river (Germany).

**Q4.** Can the idealised modelling of the starved dune formation in steady currents (Q3) be extended to reproduce the effect of sediment starvation on the formation of tidal dunes, and, if so, how do the results of the model compare to field observations?

As shown in Chapter 4, the initial stage of tidal dune formation has been successfully reproduced by means of an idealised process-based model that accounts for the effects of sediment starvation. The interaction of tidal currents with a sequence of isolated starved dunes generates steady recirculating cells which appear even when the forcing flow is purely oscillatory. The model results show that the steady streaming depends on the geometry of the starved dunes, whose profile turns out to differ from that of typical tidal dunes, and on the characteristics of the semi-diurnal tidal constituent, but it is also affected by the presence of a residual current and/or a quarter-diurnal tidal constituent. The results show that, in sand-starved environments, the spacing between successive crests of the bedforms is larger than the wavelength of the tidal dunes that would form if an infinite supply of sand would be present. When the symmetry of the tidal flow due to the semi-diurnal constituent is broken by accounting for the presence of more tidal constituents, the migration of starved dunes is predicted by the model. If only a residual current is added to the semi-diurnal tidal constituent, dune migration takes place in the direction of this residual current, whereas if a quarter-diurnal tidal constituent is further included, the starved dunes can migrate even in the opposite direction depending on the phase shift between the different tidal constituents. The lengthening and migration of tidal dunes predicted by the idealised model showed good agreement with field data on starved dunes observed in the English Channel where sediment starvation affects the dynamics of these morphological patterns.

## 5.2 Possible Future Developments

Differently modelling techniques have been successfully applied to study the formation and dynamics of hydraulic sand dunes in case of limited sand supply, conducting laboratory experiments and implementing a process-based idealised model.

The performed laboratory experiments, described in Chapter 2, provide controlled empirical foundations for the simplified analytical and numerical modelling, developed in Chapter 3. The laboratory measurements of Chapter 2 raise the following question: what happens if a much longer duration of the experiments is chosen? Non-modal dynamics of hydraulic sand dunes, three-dimensional effects and long-term nonlinearities control the equilibrium configurations of these patterns giving rise to a very complex phenomenon which asks for further physical and theoretical modelling.

The presented stability-based model is capable of describing the formation of starved dunes in fluvial and marine environments. The stability properties of the short-term dynamics of these bedforms require further attention and upgrading the model to make it applicable on time-scales exceeding the initial-stages of their formation may require a thorough revision of the description of both the hydrodynamic and the morphodynamic processes involved. The results of Chapter 3 and Chapter 4 seem to call for an extension of the model, which presently allows only an essential 'small-amplitude' and 'low-steepness' description of the dynamics of starved dunes, that comprises the nonlinear effects due to gravity and their implications on sediment transport. As a consequence, the extended model should be able to deal with the long-term dynamics of starved dunes and, as such, to describe their equilibrium configuration. As far as possible, this research could be substantially improved by further describing the physical insights that came from our modelling exercise from a mechanistically point of view. Clearly, the sediment transport rate crossing the exposed immobile substratum to its covered portions is different, the former being lower than the latter because of sediment starvation. However, how this influences the morphology of the emerging sandy patterns is an open question difficult to address as the phenomenon under investigation is strongly nonlinear. Finally, it would be worthwhile to investigate whether the physical description of the morphodynamic processes underlying the formation of starved dunes can be improved by including mechanisms that have been neglected so far (viscous effects, sediment sorting and so on).

All that being said, our modelling exercises have successfully aimed at investigating the effects of sediment starvation on the morphology of subaqueous sand dunes in a very wide sense. Two different geomorphological features have been dealt with: hydraulic sand dunes in rivers and tidal dunes in shallow seas. In order to place this work within a broader field of research, the (2DV) hydrodynamic model could be straightforwardly extended in the third direction. There is a body of work that shows that eolian dune size and spacing can emerge from finite-amplitude interactions and how these interactions, including substantial bedform lengthening, can cause desert barchan dunes to evolve (Hersen et al., 2004, Worman et al., 2013, Khosronejad and Sotiropoulos, 2017). However, an extension of the present stability analysis to account for three-dimensional effects could be used for discussing subaqueous barchan dunes as a prominent example of dunes in a sediment-limited environment, rather than necessarily reflecting only finite-amplitude interactions. Hopefully, the flow module of the model could also be extended to study the atmospheric boundary layer making the present stability analysis be able to investigate the effects of sediment starvation on the morphology of eolian sandy patterns.

# Bibliography


Allen, J. (1982). Sedimentary structures, vol. ii. *Developments in Sedimentology*, 30.

Allen, J. L. (1968). *Current ripples*. North-Holland Publishing Co.

Bagnold, R. (1953). A. 1941. the physics of blown sand and desert dunes. *London: Methuen*.

Bagnold, R. A. (1956). The flow of cohesionless grains in fluids. *Phil. Trans. R. Soc. Lond. A*, 249(964):235–297.

Besio, G., Blondeaux, P., and Vittori, G. (2006). On the formation of sand waves and sand banks. *Journal of Fluid Mechanics*, 557:1–27.

Blondeaux, P. (1990). Sand ripples under sea waves part 1. ripple formation. *Journal of Fluid Mechanics*, 218:1–17.

Blondeaux, P. and Vittori, G. (2005). Flow and sediment transport induced by tide propagation: 2. the wavy bottom case. *Journal of Geophysical Research: Oceans*, 110(C8).

Blondeaux, P., Vittori, G., and Mazzuoli, M. (2016). Pattern formation in a thin layer of sediment. *Marine Geology*, 376:39–50.

Brownlie, W. R. (1981). Prediction of flow depth and sediment discharge in open channels. Technical report, California Institute of Technology.

Camporeale, C. and Ridolfi, L. (2011). Modal versus nonmodal linear stability analysis of river dunes. *Physics of Fluids*, 23(10):104102.

Carling, P., Golz, E., Orr, H., and Radecki-Pawlik, A. (2000). The morphodynamics of fluvial sand dunes in the river rhine, near mainz, germany. i. sedimentology and morphology. *Sedimentology*, 47(1):227–252.

Coleman, S. E. and Melville, B. W. (1994). Bed-form development. *Journal of hydraulic engineering*, 120(5):544–560.

Colombini, M. (2004). Revisiting the linear theory of sand dune formation. *Journal of Fluid Mechanics*, 502:1–16.

Colombini, M. and Stocchino, A. (2008). Finite-amplitude river dunes. *Journal of Fluid Mechanics*, 611:283–306.

Colombini, M. and Stocchino, A. (2011). Ripple and dune formation in rivers. *Journal of Fluid Mechanics*, 673:121–131.

Colombini, M. and Stocchino, A. (2012). Three-dimensional river bed forms. *Journal of Fluid Mechanics*, 695:63–80.

Dean, R. (1974). Aero report 74-11. *Imperial College, London*, 155.

Deigaard, R. and Fredsøe, J. (1987). Offshore sand waves. In *Coastal Engineering 1986*, pages 1047–1061. Coastal Engineering Proceedings.

Dietrich, W. E., Kirchner, J. W., Ikeda, H., and Iseya, F. (1989). Sediment supply and the development of the coarse surface layer in gravel-bedded rivers. *Nature*, 340(6230):215.

Einstein, H. A. (1934). Der hydraulische oder profilradius. *Schweizer Bauzeitung*, 103(8):89–91.

Engelund, F. (1970). Instability of erodible beds. *Journal of Fluid Mechanics*, 42(2):225–244.

Exner, F. M. (1925). Uber die wechselwirkung zwischen wasser und geschiebe in flussen. *Akad. Wiss. Wien Math. Naturwiss. Klasse*, 134(2a):165–204.

Fernandez Luque, R. and Van Beek, R. (1976). Erosion and transport of bed-load sediment. *Journal of hydraulic research*, 14(2):127–144.

Fredsøe, J. (1974). On the development of dunes in erodible channels. *Journal of Fluid Mechanics*, 64(1):1–16.

Fredsøe, J. and Deigaard, R. (1992). *Mechanics of coastal sediment transport*, volume 3. World scientific.

Gerkema, T. (2000). A linear stability analysis of tidally generated sand waves. *Journal of Fluid Mechanics*, 417:303–322.

Guy, H. P., Simons, D. B., and Richardson, E. V. (1966). *Summary of alluvial channel data from flume experiments, 1956-61*. US Government Printing Office.

Hara, T. and Mei, C. C. (1990). Oscillating flows over periodic ripples. *Journal of Fluid Mechanics*, 211:183–209.

Hersen, P., Andersen, K. H., Elbelrhiti, H., Andreotti, B., Claudin, P., and Douady, S. (2004). Corridors of barchan dunes: Stability and size selection. *Physical Review E*, 69(1):011304.

Houbolt, J. (1968). Recent sediments in the southern bight of the north sea. *Geologie en mijnbouw*, 47(4):245–273.

Howard, A., Morton, J., GAD-EL-HAK, M., and Pierce, D. B. (1978). Sand transport model of barchan dune equilibrium. *Sedimentology*, 25(3):307–338.

Hulscher, S. J. (1996). Tidal-induced large-scale regular bed form patterns in a three-dimensional shallow water model. *Journal of Geophysical Research: Oceans*, 101(C9):20727–20744.

Johnson, J. W. (1942). The importance of considering sidewall friction in bed-load investigations. *Civil Engineering*, 12:329–332.

Kennedy, J. F. (1969). The formation of sediment ripples, dunes, and antidunes. *Annual review of fluid mechanics*, 1(1):147–168.

Kenyon, N. H. (1970). Sand ribbons of european tidal seas. *Marine Geology*, 9(1):25–39.

Khosronejad, A. and Sotiropoulos, F. (2017). On the genesis and evolution of barchan dunes: morphodynamics. *Journal of Fluid Mechanics*, 815:117–148.

Kleinhans, M., Wilbers, A., De Swaaf, A., and Van Den Berg, J. (2002). Sediment supply-limited bedforms in sand-gravel bed rivers. *Journal of sedimentary research*, 72(5):629–640.

Le Bot, S. (2001). *Morphodynamique de dunes sous-marines sous influence des marées et des tempêtes*. PhD thesis, Université de Lille.

Le Bot, S. and Trentesaux, A. (2004). Types of internal structure and external morphology of submarine dunes under the influence of tide-and wind-driven processes (dover strait, northern france). *Marine Geology*, 211(1):143–168.

Le Bot, S., Trentesaux, A., Garlan, T., Berne, S., and Chamley, H. (2000). Influence des tempêtes sur la mobilité des dunes tidales dans le détroit du pas-de-calais. *Oceanologica Acta*, 23(2):129–141.

Lonsdale, P. and Malfait, B. (1974). Abyssal dunes of foraminiferal sand on the carnegie ridge. *Geological Society of America Bulletin*, 85(11):1697–1712.

Meyer-Peter, E. and Müller, R. (1948). Formulas for bed-load transport. In *IAHSR 2nd meeting, Stockholm, appendix 2*. IAHR.

Neill, C. (1968). Note on initial movement of coarse uniform bed-material. *Journal of Hydraulic Research*, 6(2):173–176.

Németh, A. A., Hulscher, S. J., and de Vriend, H. J. (2002). Modelling sand wave migration in shallow shelf seas. *Continental Shelf Research*, 22(18):2795–2806.

Nezu, I. and Nakagawa, H. (1984). Cellular secondary currents in straight conduit. *Journal of hydraulic engineering*, 110(2):173–193.

Parker, G., Klingeman, P. C., and McLean, D. G. (1982). Bedload and size distribution in paved gravel-bed streams. *Journal of the Hydraulics Division*, 108(4):544–571.

Parker, G., Seminara, G., and Solari, L. (2003). Bed load at low shields stress on arbitrarily sloping beds: Alternative entrainment formulation. *Water resources research*, 39(7).

Richards, K. J. (1980). The formation of ripples and dunes on an erodible bed. *Journal of Fluid Mechanics*, 99(3):597–618.

Roos, P., Blondeaux, P., Hulscher, S., and Vittori, G. (2005). Linear evolution of sandwave packets. *Journal of Geophysical Research: Earth Surface*, 110(F4).

Roos, P. and Schuttelaars, H. (2013). Influence of time-and depth-dependent eddy viscosity on the formation of tidal sandwaves. *VLIZ Special Publication*.

Sakai, Y. and Uhlmann, M. (2016). High-resolution numerical analysis of turbulent flow in straight ducts with rectangular cross-section. In *High Performance Computing in Science and Engineering´ 15*, pages 301–313. Springer.

Sekine, M. and Kikkawa, H. (1992). Mechanics of saltating grains. ii. *Journal of Hydraulic Engineering*, 118(4):536–558.

Seminara, G. (1998). Stability and morphodynamics. *Meccanica*, 33(1):59–99.

Shields, A. (1936). Anwendung der aehnlichkeitsmechanik und der turbulenzforschung auf die geschiebebewegung. *PhD Thesis Technical University Berlin*.

SHOM (1968). Courants de mare´e dans la manche et sur les co^tes franc¸aises de l'atlantique. Technical report, Service Hydrographique et Oce´anographique de la Marine.

Smith, D. and Rijkswaterstaat, D. G. (1988). Morphological development of the sandettie south falls gap: A degeneration ebb dominated tidal passage in the southern north sea. *De Boer PL, Van Gelder A., Nio SD (éd.), Tide-influenced sedimentary Environments and Facies, D. Reidel Publishing Company*, pages 51–64.

Sumer, B. M. and Bakioglu, M. (1984). On the formation of ripples on an erodible bed. *Journal of Fluid Mechanics*, 144:177–190.

Talmon, A., Struiksma, N., and Van Mierlo, M. (1995). Laboratory measurements of the direction of sediment transport on transverse alluvial-bed slopes. *Journal of Hydraulic Research*, 33(4):495–517.

Tuijnder, A. P., Ribberink, J. S., and Hulscher, S. J. (2009). An experimental study into the geometry of supply-limited dunes. *Sedimentology*, 56(6):1713–1727.

Van Rijn, L. (1991). Sediment transport in combined waves and currents. In *Proceedings of Euromech*, volume 262, pages 3–15.

Van Rijn, L. C. (1984). Sediment transport, part i: bed load transport. *Journal of hydraulic engineering*, 110(10):1431–1456.

Vanoni, V. (1975). Sediment discharge formulas. *Sedimentation engineering*, pages 190–229.

Vanoni, V. A. and Brooks, N. H. (1957). Laboratory studies of the roughness and suspended load of alluvial streams.

Venditti, J. G., Nelson, P. A., Bradley, R. W., Haught, D., and Gitto, A. B. (2017). Bedforms, structures, patches, and sediment supply in gravel-bed rivers. *Gravel-Bed Rivers: Process and Disasters*, 439.

Vittori, G. (1989). Non-linear viscous oscillatory flow over a small amplitude wavy wall. *Journal of Hydraulic research*, 27(2):267–280.

Wippermann, F. and Gross, G. (1986). The wind-induced shaping and migration of an isolated dune: a numerical experiment. *Boundary-Layer Meteorology*, 36(4):319–334.

Wong, M. and Parker, G. (2006). Reanalysis and correction of bed-load relation of meyer-peter and müller using their own database. *Journal of Hydraulic Engineering*, 132(11):1159–1168.

Worman, S. L., Murray, A. B., Littlewood, R., Andreotti, B., and Claudin, P. (2013). Modeling emergent large-scale structures of barchan dune fields. *Geology*, 41(10):1059–1062.